STATISTICAL CHARACTERIZATION OF MORPHODYNAMIC SIGNALS USING WAVELET ANALYSIS

by

Ronald R. Gutierrez

BSc, National University of Engineering, Peru, 1997

MSc, University of Pittsburgh, USA, 2012

Submitted to the Graduate Faculty of
the Swanson School of Engineering in partial fulfillment
of the requirements for the degree of
Doctor of Philosophy

University of Pittsburgh

2013

UNIVERSITY OF PITTSBURGH

SWANSON SCHOOL OF ENGINEERING

This dissertation was presented

by

Ronald R. Gutierrez

It was defended on

April 3rd, 2013

and approved by

Jorge D. Abad, PhD, Assistant Professor, Department of Civil and Environmental Engineering

Xu Liang, PhD,Associate Professor, Department of Civil and Environmental Engineering

Daniel Budny, PhD, Associate Professor, Department of Civil and Environmental Engineering

Piervincenzo Rizzo, PhD, Associate Professor, Department of Civil and Environmental Engineering

Eddy J. Langendoen, PhD, National Sedimentation Laboratory, USDA

Dissertation Director: Jorge D. Abad, PhD, Assistant Professor, Department of Civil and Environmental Engineering

STATISTICAL CHARACTERIZATION OF MORPHODYNAMIC SIGNALS USING WAVELET ANALYSIS

Ronald R. Gutierrez, PhD

University of Pittsburgh, 2013

Morphodynamic and hydrodynamic properties are concomitantly part of the entire dynamic of river systems and commonly present both temporal and spatial persistent variability. Therefore, the study of both river morphodynamic signals (e.g. bed forms and meandering and anabranching river morphometrics) and hydrodynamic signals (e.g. velocity fields, sediment concentrations) requires both temporal and spatial multi-scale signal representations. The present research is focused on the former type of signals and it is a first attempt to discriminate such signals and, subsequently, develop the theoretical background to link these processes at different spatial and temporal scales and determine the scales that have more influence on river evolution.

The present research contribution has reached the following achievements: [1] to design a methodology to discriminate bed form features (e.g. bars, dunes and ripples) via the combined application of robust spline filters and one-dimensional continuous wavelet transforms, allowing the quantitative recognition of bed form hierarchies. The methodology was tested by using synthetic bed form signals and subsequently applied to the analysis of bed form features from the Paraná River, Argentina. [2] To design a methodology for the statistical analysis of the spatial distribution of meandering rivers morphometrics by coupling the capabilities of one-dimensional wavelet transforms, principal component analysis and Frechét distance. A universal river classification method is also proposed. [3] To perform a novel study of the planimetric configuration of confluences in tropical free meandering rivers located in the upper Amazon catchment. River confluences in tropical environments represent

areas where biota is concentrated; therefore, a better understanding and characterization of these features has a particular importance for the Amazonian ecosystem. [4] To evaluate the potential of on two-dimensional wavelet transforms in the analysis of bed form features. The broader impact will be an improved understanding of river morphodynamics of the upper Amazon River for practical applications such as navigability. Furthermore, the project will provide an updated statistical analysis of the meandering rivers dynamics for practical applications, including erosion control, river ecology, and habitat restoration. The developed statistical tool will be included as an application of the RVR Meander platform (www.rvrmeander.org), which is a broadly used software for river restoration.

TABLE OF CONTENTS

LIST OF TABLES

LIST OF FIGURES

PREFACE

To my mother Saturnina, my brothers (Ulises and Jaime) and sisters (Nazia, Dalia and Sonia), my friends and Lily who supported me to complete this endeavor.

Simplex sigillum veri - The simple is the seal of the true.

ACKNOWLEDGEMENT

All my gratitude to Dr. Jorge D. Abad for his comments and encouragement. Likewise, I greatly appreciate the support from grants bestowed to me by the University of Pittsburgh's Center for International Studies and by the American Society of Civil Engineers, ASCE (2012 Freeman Fellowship).

1.0 INTRODUCTION AND MOTIVATION

Morphodynamic and hydrodynamic properties are concomitantly part of the entire dynamic of river systems and they commonly present both temporal and spatial persistent variability. Therefore, the study of both river morphodynamic signals (e.g. bed forms, bank forms, and meandering and anabranching river morphometrics) and hydrodynamic signals (e.g. velocity fields, sediment concentrations) requires both temporal and spatial multi-scale signal representations. The present research is a first attempt to discriminate the former signals in order to, subsequently, develop the theoretical background to link these processes at different spatial and temporal scales and determine the scales that have more influence on river evolution.

Despite copious research on river bed forms, there is not a standard methodology to discriminate bed form features based on their length scales. Most of the studies have also simplified bed forms as two-dimensional entities, although they exhibit markedly three-dimensional patterns in natural channels. Past methodologies for bed forms scale discrimination have used moving average and Gaussian filters, Fourier transforms and one-dimensional wavelets, which have proved to be limited in describing highly non-stationary and three-dimensional signals as bed form signals. Likewise, there is not a tailored statistical tool to analyze and to classify meandering rivers. On the other hand, there is limited number of studies on tropical rivers such as those located at the upper Amazon River basin; even though the Amazon river represents the world's largest river and is crucial to sustain the humankind.

The present research has the following main objectives: [1] to design a methodology to discriminate bed form features (e.g. bars, dunes and ripples) based on a scale hierarchization criterion; [2] to design a statistical tool to study the plan morphometrics of meandering and complement the prevailing Bryce classification criteria; and subsequently, study the spatial distribution of meanders (e.g. confluences, morphometrics, class variation); and [3] to asses the capabilities of the two-dimensional wavelet transforms in the analysis of bed form features. The thesis is split into 6 chapters, being **Chapter 1** a brief introduction to the main text.

Chapter 2 deals with the background in the analysis of river morphodynamic signals, and the previous work of the thesis author on the analysis of bed form features using one dimensional wavelet transforms and robust spline filters is highlighted. As part of the thesis to obtain the MSc. degree, the author of this thesis proposed a standardization of the nomenclature and symbolic representation of bed forms, and detailed the combined application of robust spline filters and continuous wavelet transforms to discriminate these morphodynamic features, allowing the quantitative recognition of bed form hierarchies. The proposed methodology for bed form discrimination was firstly applied to synthetic bed form profiles, which were sampled at a Nyquist ratio interval of 2.5-50 and a signal-to-noise ratio interval of 1-20, and subsequently applied to a detailed 3D bed topography from the Río Paraná, Argentina, which exhibits large-scale dunes with superimposed, smaller bed forms. After discriminating the synthetic bed form signals into 3 bed form hierarchies that represent bars, dunes and ripples, the accuracy of the methodology was quantified by estimating the reproducibility, the cross correlation and the standard deviation ratio of the actual and retrieved signals. For the case of the field measurements, the proposed method was used to discriminate small and large dunes; and subsequently obtain and statistically analyze the common morphological descriptors such as wavelength, slope, and amplitude of both stoss and lee sides of these different size bed forms. Analysis of the synthetic signals demonstrated that the Morlet wavelet function is the most efficient in retrieving smaller periodicities such as ripples and smaller dunes features, and that the proposed methodology effectively discriminated waves of different periods for Nyquist ratios higher than 25 and signal-to-noise ratios higher than 5. The analysis of the bed forms of the Paraná River revealed that, in most cases, a Gamma probability distribution, with a positive skewness, best describes the dimensionless wavelength and amplitude for both the lee and stoss sides of large dunes. For the case of the smaller superimposed dunes, the dimensionless wavelength showed a discrete behavior that is governed by the sampling frequency of the data, and the dimensionless amplitude better fits the Gamma probability distribution, again with a positive skewness. The study thus provided a robust methodology for systematically identifying the scales and magnitudes of bed forms in a range of environments.

Chapter 3 details the proposed methodology for meandering river morhometrics statistical analysis. The Mean Center (MC) is defined as the midterm lifespan coherent wave of the meanders centerline and it is obtained using a methodology that combines the capabilities of the principal component analysis and the discrete wavelet transforms. The Daubechies-10 wavelet —at level $J = 5 - 8$ best defines the MC. The application of wavelet cross correlation shows that river curvature is strongly correlated with that of the MC; thus, in confined rivers, lower local curvature at the river centerlines are related to peaks in the MC local curvature; conversely, in freely meandering rivers, compound bends and multiple loops are associated to peaks in the MC local curvature. In all the cases, the river's normalized curvature exhibit a normal distribution after the Johnson transformation is performed. Likewise, wavelet analysis of the dimensionless curvature indicates that the arc-wavelength is typically bimodal, with higher and lower coherent frequencies respectively ranging from $\sim 5\bar{B}$ and $\sim 20\bar{B} - 25\bar{B}$ ($\bar{B}$ is the channel width). The normalized planform amplitudes typically ranges in the interval $\sim 2\bar{B}$-$7\bar{B}$ for confined rivers and in the interval $\sim 8\bar{B}$ to higher than $20\bar{B}$ for freely meanders. The application of the normalized Fréchet distance is introduced as well as the gradient of the curvature wavelet entropy to classify freely from confined meanders. Confined meanders are bounded by a normalized Fréchet distance ∼650. Thus, the MC shows to be a strong frame to classify meandering rivers and also has also the potential to discriminate modeled from natural meandering rivers.

Chapter 4 elaborates on the characterization of free meandering rivers confluences. Most of the past studies on river confluences dynamics are based on a limited number of experimental and field data that mainly represent the morphodynamic, hydrodynamic and sedimentary processes of alluvial river channels with limited planform activity and concentrated solely around the confluence region. This novel contribution focuses on the study of the planimetric configuration of confluences in tropical free meandering rivers located in the Upper Amazon catchment. Since river confluences in tropical environments represent areas where biota is concentrated, a better understanding and characterization of these features has a particular importance for the Amazonian ecosystem. Confluence of meandering rivers or meander trains (asumming one is the main channel and the other a tributary) imposes the following general changes in the planimetric configurations of these channels: [1] modulation of the morphodynamics of the upstream main (M) and tributary (T) channels and [2] modulation of the morphodynamics of the downstream main channel (MT), thus increasing the arc-wavelength and amplitude and resembling a constructive effect in the superposition of curvature waves. A Wavelet analysis of the normalized channel curvature was performed by using the continuous Morlet Wavelet function. This analysis indicates that important transient perturbations in the curvature frequency spectrum are being developed when the ratio between the tributary width and the main channel width (upstream of the confluence point) ($\beta = B_T/B_M$) are higher than 0.5, as those perturbations become more dominant when the width-ratio (β) increases.

Chapter 5 examines the state of the art of the application of two-dimensional wavelet transforms in the analysis of topographic data and proposes the design of synthetic bed form signals that might be used benchmark signals for calibration of the two dimensional wavelet functions parameters (e.g. dilation, translation and rotation parameters). **Chapter 6**, presents the proposed future work towards the statistical characterization of morphodynamic signals. The final chapter, **Chapter 7**, covers the main conclusions of the present thesis.

2.0 BACKGROUND

2.1 INTRODUCTION TO THE RESEARCH PROBLEM

River morphodynamic signals are comprised by planform (i.e. river centerline planimetry), altimetric (e.g. bed forms), and bank form data. These signals help to understand the spatial and temporal scales of river migration; therefore, not only characterization of morphodynamic features is possible, but also to define heterogeneous regions along the longitudinal and transversal direction of the river. They have been studied extensively in the past [42, 229, 128, 127, 2, 182]. It is important to mention that Blondeaux and Seminara; 1985 ([42]) referred as unified planimetric and altimetric instabilities to the interaction of force and free bars, respectively. Herein, a combination of planform and altimetric perturbations describes the bank morphology and bank alignment (lateral perturbations) which is a consequence of heterogeneous distribution of local flow structure and shear stresses induced by bed and planform morphology [6]. Even though these in channel morphodynamic structures have been known for long time, little has been done to [1] characterize their dominant spatial and temporal scales of the morphological signals, and [2] to study the interactions to form the natural bed, bank and planform river configuration and the participation, as a main controlling factor, of the morpho-sedimentary characteristics of the floodplain. Figure 2.1 shows the planform, altimetric and lateral morphodynamic structures (e.g. meander bends, progressive bedforms and bank morphology, respectively). Even though these morphodynamic settings are different (in Figure 2.1), similar signals can be obtained by using the curvature along the streamwise direction for the case of meandering channels, bed elevation along longitudinal transects showing ripples superimposed over sand bars or dunes for the case of bed morphology, and longitudinal transects along the banks that show the lateral

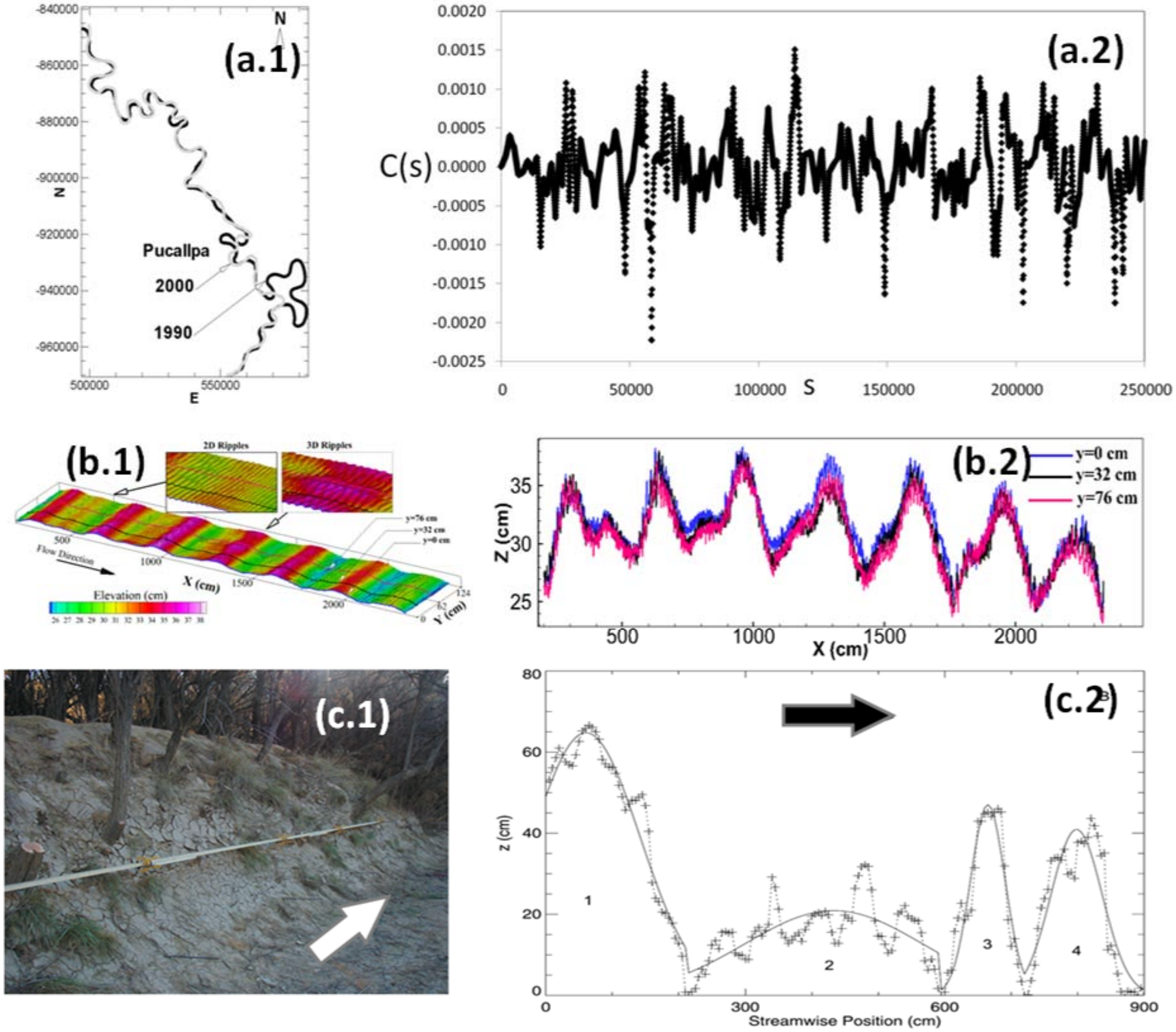

Figure 2.1: Examples of morphodynamic structures: (a) meandering channel (Ucayali River, Peru, [7]), (b) unidirectional-dominated bedforms (laboratory experiments, [58], (c) bank morphodynamics (Rio Puerco, New Mexico, [127]).(a.1), (b.1) and (c.1) represent the morphodynamic structure and (a.2), (b.2) and (c.2) represent the uni-directional signal for each morphodynamic feature.

oscillation of bank alignment and morphology. Therefore by developing uni-directional statistical and morphometric tools benefits its physical description and understanding of each of these morphodynamic signals, but also their correlation among these signals when date is available.

In recent years, several morphometric tools [108, 167, 9, 90] have been developed to characterize the above morphodynamic structures. However, little has been done for applying one-dimensional (1D) wavelets into this characterization. Very few exceptions are related to streamflow and sediment load temporal variations in the Mississippi River [223], first attempt to characterize bedform morphology under laboratory conditions [58], first attempt to characterize bedform morphology in a field scale condition, the Parana River [98], first attempted to characterize planimetric patterns of meandering rivers [2, 4], seabed morphology pattern recognition [158] and riverbed roughness [191]. In general the application of wavelets into the description of geophysical signals were performed for the case of fluid mechanics with isolation of coherent structures in turbulent flows, meteorology with temporal variability of coherent convective storm structures, climatology with long-term land temperature series, paleoclimatology with oxygen isotopic ratios from marine sediments, among others [143]. This study concerns to the development of a 1D morphodynamic statistical tool that includes the wavelet methodology as well as other morphometric tools that will be explained below. The following are the current morphometric tools that were developed to characterize these morphodynamic structures:

2.1.1 Meandering Channels

For the case of meandering channels, some development of morphometric variables and the application of 1D-wavelets have been proposed to quantify the main characteristics of the meandering streams and further conduct numerical comparison and/or statistical analysis. Knowledge of these conditions is also important for understanding fluvial landforms, for reconstructing paleo environments, and for predicting the effects of natural and, increasingly often, man-induced changes in the modern environment. This knowledge can only be obtained if meander geometry is not only quantified but is reduced to a manageable number of parameters [88]. Howard and Hemberger, 1991 [108] measured 40 morphometric variables that were aimed to quantify the sinuosity, meandering wavelength, curvature moment, meander asymmetry, and pattern irregularity. Morphometric variables were roughly grouped into two categories; those that are assemble averages for the entire measured channel, and that of half-meanders defined by successive inflection points. Morphometric variables of meandering rivers could be applied to other quasi-periodic natural phenomena, such as dune profiles, water waves, and sedimentary coastlines characterized by regular cuspate planform [108]. With the aim of distinguishing between natural and modeled channels, [90] proposed using just 12 relevant morphometric variables. They also introduced a new morphodynamic length scale associated with spatially oscillating disturbances and pointed out that once normalized with this length scale, the relevant morphologic features of the simulated long-term patterns (e.g., the probability of density function of local curvature and the geometric of oxbow lakes) tend to collapse on two distinct behaviors, corresponding to either sub-resonant or super-resonant conditions, depending on the dominant morphologic regime. Spectral analysis of meanders by [235, 60, 88, 76, 106] indicate that the characteristic meander wavelength is a poor indicator of the dominant frequencies of oscillation and there seems to be more than one characteristic wavelength in a meander system. Chang and Toebes, 1970 [60] analyzed the correlation between the curvature distribution and both discharge and geology and found that the distributions are not of Gaussian type. These spectral analyses were carried out by using the windowed Fourier transform which assumes that the data is stationary although river plan form parameters possess trend, or non-stationarities, because of the continuous increase of the flow rate hence the increase of river dimensions going downstream [60]. Fourier analyses have severe limitations for analyzing signals that include significant departures from stationarity, consisting of intermittent burst processes or intermittent processes. A high number of Fourier coefficients are necessary to take into account these structures which are visible on some intervals and invisible on others [143]. Wavelet analysis has been developed in order to provide a performing analyzing tool for this kind of signals. It effectively renders possible a timescale localization of the process thanks to a projection on a class of functions which in turn makes it possible to extract information within a local neighborhood [143].

2.1.2 Bed Forms

For the case of altimetric structures, riverbed morphology studies reveled that commonly found morphological bed features in continental shelves and rivers are ripples, dunes and bars. They have been usually observed in amalgamated form, i.e. ripples superimposed upon dunes [58]. Although the distinction between ripple and dune is so apparently obvious that many authors fail to mention their criteria for separating them in field and laboratory studies; however these criteria are often different. Ashley, 1990 [21] proposed a wavelength of 0.60 m as threshold to separate ripples from dunes, and this became the official criterion [117]. After the separation had been done, wavelet tools can be applied to estimate the dominant wavelength, amplitude and lee and stoss slopes. This information is important to later separate the skin and form shear stresses. Gutierrez et. al., 2012 [98] successfully used one-dimensional wavelets to quantify the dominant periods in bed forms for large natural channels such as the Parana River. Since the election of the mother wavelet is crucial to retrieve representative information of the bed forms, Gutierrez et. al., 2012 also provided insights in the criteria to choose the most efficient mother wavelet based on sampling frequency and signal-to-noise ratios quantities. A detailed description of the this work is presented in Section 2.2.

2.1.3 Bank Morphodynamics and Alignment

These morphodynamic structures have received less attention and past studies where mainly dedicated to calculate rate of erosion based on digitalization of aerial and satellite images [183], to attempt to describe a physically-based model for bank erosion [147]. The bank alignments are directly related to the importance on defining the channel width variation [163] and its implications for meandering evolution. However, few attempts to characterize the bank morphology and alignment were done by Kean and Smith (2006a, 2006b). Therefore, for the case of bank morphology and bank alignment, there is no statistical analysis that has been carried out to characterize the dominant scales.

2.1.4 The Role of the Floodplain

A fluvial system is a physical system with history and the fluvial archive is the floodplain, a fact frequently forgotten by engineers, planners and ecologist that applied actualistic short time approaches concentrating on **in channel** processes. The heritage of the landforms and the sedimentary architecture of the floodplain play a major role in the paths of transmission of water and sediments as well as on the control of rates of planform adjustments (erosion/deposition rates at different fluvial reaches). Moreover, many of the models on planform analysis (characterization) and migration of meandering rivers, as referenced above ([51, 229], among others), do not integrate the valuable and fundamental information provided by the morpho-sedimentary analysis of the floodplain.

2.2 DISCRIMINATION OF BED FORM SCALES USING ROBUST SPLINE FILTERS AND WAVELET TRANSFORMS

2.2.1 Introduction

The quantification of variability in bed form geometry is necessary for scientific and practical applications, such as in quantifying and explaining: [1] bed roughness [245, 13], [2] the formation of cross-strata [206, 196, 239, 162, 40, 94, 210, 214], [3] the vertical sorting of sediments [133, 41, 134, 141], [4] sediment transport rates [101, 259, 80, 139, 91, 232], [5] the transition between 2D and 3D dunes [254], and [6] velocity pulsations within the flow [100, 105, 231]. Such quantification is also required for the numerical modeling of flow over bed forms (e.g. [131, 257, 236]), assessing the interaction between flow over bed forms and ground-water [54, 53, 55], and evaluating contaminant transport [195]. For practical purposes, the study of the variability of bed forms is important in: [1] the prediction of floods and flow resistance [19, 121, 207, 132, 126, 258], [2] the prediction of potential disturbance to man-made structures, such as river tunnels [18] and bridges, [3] predicting future changes in sediment transport rates and biotic responses following dam removal (e.g. [178]), [4] for estimating the relationship between bed form characteristics and biota [260, 240].

The morphology and dynamics of alluvial bed forms are strongly governed by the interrelationship between sediment transport and the hydraulic conditions. The persistent variability in the geometry and migration rates of bed forms is the hallmark of behavior under, and interacting with, unidirectional shear flows [118]. However, at present we lack a consistent, non-arbitrary, quantitative description of both the morphology and dynamics of bed forms across a range of spatial scales that is necessary to understand the effect of their morphology upon bed form migration, sediment transport and the resultant bed roughness.

Theoretical research on the morphodynamics of non-cohesive channel beds has largely followed five distinctive approaches [99] in which sediment continuity was incorporated into the governing equations [84], the water-bed interface was regarded as a Kelvin-Helmholtz instability [159], the fluid-bed interface was investigated using linear stability theory [130], kinematically admissible bed form profiles were obtained using the Helmholtz Kirchoff method [175], and dimensionless statistical correlations were performed [263].

Statistical methods developed for the description of bed forms in alluvial channels were first proposed by [189] and [83]. Research performed following the fifth statistical approach has typically used morphometric parameters such as bed form height (Δ), wavelength (λ) and steepness (Δ/λ) to describe and classify features such as ripples and dunes commonly found on continental shelves and within river channels in various superimposed states [21, 58].

Some early studies considered bed form profiles to be stochastic variables [190, 115, 176] that were analyzed by using time series analysis techniques [156]. However, more recent studies have used spatial scaling techniques that treat bed elevations in a bed form profile as a random function, rather than identifying individual bed forms in a profile [187, 118, 250].

The variability of bed form morphology is the principal factor determining the total form roughness of a channel, and there is theoretical, laboratory, and field evidence that the roughness of bed forms of all wave lengths, up to the scale of the largest bed forms, play a key role. It has also been hypothesized that the variability in geometric variables of individual bed forms within a reach affects the reach-averaged form roughness [250]. Based on experimental measurements and field data, [265] proposed that the form resistance, f”, when ripples are superimposed upon dunes can be estimated as $f\text{”} = 4\Xi$ if $\Xi >\simeq 10^{-2}$, and as $f\text{”} = [3.3\log(\Xi - 1) - 2.3]^{-2}$ if $\Xi <\simeq 10^{-2}$; where $\Xi = \frac{\Delta^2}{\Lambda h}$ (see Figure 2.2a for the geometric definition of these variables). These relationships suggest that drag resistance is dependent mainly on the geometric characteristics of dunes. Field measurements also prove the importance of the geometry of larger dunes in the drag resistance, even using other relationships such as those proposed by Vanoni-Hwang, van Rijn (modified) and Engelund as reported by [120]. Moreover, [250] hypothesized that the variability of individual bed forms within a reach affects the reach-averaged form roughness, and base this hypothesis on the analogy between grain roughness and form roughness. For example, the 65%, 84%, or 90% percentiles of the grain size distribution are often used as a representative particle diameter in predicting the grain roughness. Similarly, form roughness may also be determined from bed forms that are higher, longer or steeper than the median or mean bed form height, bed form length, or bed form steepness, respectively [250].

Past approaches to the quantification of bed form variability have used and applied spectral analysis [103, 115, 116, 19, 156, 132], smoothing techniques such as a moving-average [48, 120, 259, 104, 91, 250], signal roughness techniques [232], fractals [260], and logistic regression [123]. However, moving-average techniques as well as Fourier series analysis have generally proved to be insufficient as a tool to extract the long-term variation from signals that contain a long-term trend with a superimposed fine oscillation (i.e. the short term variation) [241]. This lack of success is primarily because in using spectral analysis, the major assumption is that the bed form waves are two-dimensional and not highly variable in the cross-stream direction [156]. Likewise, the Fourier transform, which is used in spectral analysis, has severe limitations when analyzing signals that include significant departures from stationarity and consist of intermittent and/or aperiodic processes. In those cases, a high number of Fourier coefficients are necessary to take these processes, that may be visible in some intervals but not in others, into account [143]. Thus, a limited representation of the frequencies of nonlinear processes, such as river bed morphology, is obtained. Wavelet transforms were developed to overcome the limitations of Fourier transforms and have been applied to fluid mechanics in the isolation of coherent structures in turbulent flows [85], in analyzing the temporal variability of coherent convective storm structures [142], within investigation of long-term land temperature/climate series [29], in analyzing oxygen isotopic ratios from marine sediments [208], and in analyzing the local curvature of meanders [8].

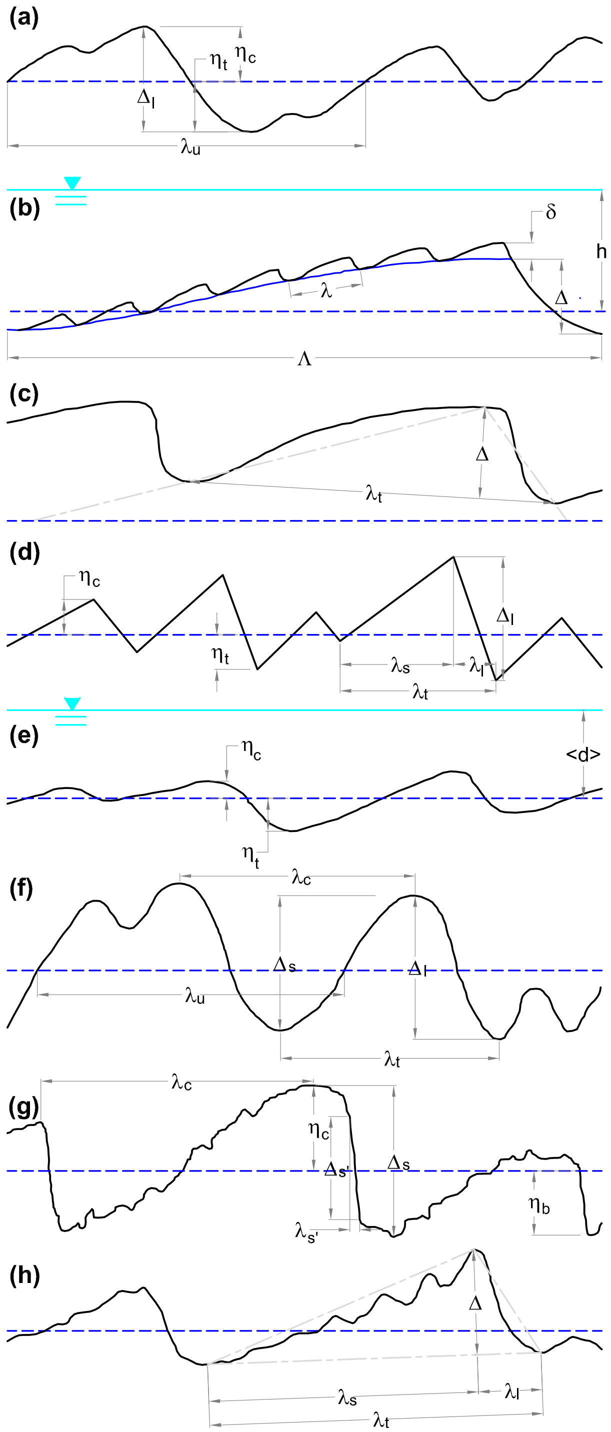

Figure 2.2: Bed form parameters after (a)[19], (b) [265] (c) [259], (d) [251], (e) [118], (f) [249], (f) [252] and (h) [136]. In each case, the blue dotted lines represent the mean elevation.

Some recent applications of 1D-wavelets in sedimentology encompass temporal variations within streamflow and sediment loads [223], characterization of bed form morphology [58, 233], sediment concentration distributions [87], the recognition of patterns in seabed morphology [158], analysis of riverbed roughness [191], and investigation of flow structure over alluvial sand dunes [231]. Herein, we demonstrate that this technique identifies the various scales of bed forms present within a series and significantly improves the quantification of form roughness at different bed form scales.

2.2.2 Bed Form Discrimination Method and Data

2.2.2.1 Synthetic Signal Data In order to assess the accuracy of the discrimination methodology proposed herein, a set of well-constrained synthetic signals were firstly examined. These signals comprise three waves of different periodicity that are intended to replicate ripples, dunes and bars. Ripples are represented by a random signal generated using the Wichman-Hill algorithmthat in some instances imposes periods not sufficient large on the generated signals [140]. The mean of these signals is equal to zero, and their variance was changed in order to obtain an interval with signal-to-noise ratios (SNR) from approximately 1 to 20. The SNR is defined as the ratio between the variance of the random signal and the variance of the signal comprised by the summation of the bar and dunes signals. The stoss side of the dunes is represented by the lower-regime dunes equation $\eta_{2,s}(x)$ (Equation 2.1) and proposed by [99]. The lee face is represented by a straight line, defined by Equation 2.2.

$$\eta_{2,s} = SL\left\{\frac{1}{2\pi\sin\frac{k\pi}{2}}\left(\ln\sin\frac{\pi}{L}\left(x+\frac{L}{2}[1-k]\right)-\ln\sin\frac{\pi}{2}[1-k]\right)+\frac{x}{L}\right\};\ \text{for } 0\leq x\leq kL \tag{2.1}$$

$$\eta_{2,l} = -\frac{a(L-x)}{(k-1)L};\ \text{for } kL < x \leq L \tag{2.2}$$

where S is the slope a/b, $S = tan(\theta)$, for θ =10 ° (see [99] for geometric details). L is the dune wavelength (assumed to be equal to 10 m) and k is the normalized length of the stoss face, which was assumed to be equal to 0.7. This value is close to $k = 0.667$ as predicted by theory for mature ripples and dunes [99]. Centered (zero mean) versions of these dunes are used in the present application. Higher noise was applied to the dunes stoss side than that of lee side, in order toreplicate the position of the ripples that are far more common supperimposed on the stoss side of dunes.

Bars are represented by the sinusoidal function $\eta_3(x) = a * Sin(2x/T - c) + d$; where x is the relative distance in meters, $a = 0.05$ m, T (the period) is equal to 200, $c = 100$ and $d = 0.05x$. The term d provides a slope in this synthetic bar signal.
The bed form synthetic signals are discretized at sampling intervals $\Delta x =$ 2m, 1m, 0.5m, 0.167m, 0.125m and 0.1m. Based on the ratio proposed by [71], the Nyquist ratio (NR) is defined as the number of times (> 1) the Nyquist sample rate is necessary to accurately recover the intermediate bed form scales (e.g. dunes). Since the life-span of the bed forms depends on the sediment transport rate fixed by flow conditions and on the bed form excursion, the distance over which an induvidual may travel [15], this definition aims to estimate the best sampling intervals for river bed forms where the intermediate scales present longer life-spans than that of the shorter scales (e.g. ripples). Since the Nyquist rate to recover dunes of $L = 10m$ is $\Delta x_N = 5$, an interval of $NR = \Delta x_N/\Delta x$ of 2.5, 5, 10, 30, 40 and 50 is obtained.

2.2.2.2 Paraná Study Reach Bed forms measured within the Río Paraná, the World's seventh largest river by mean flow discharge [96], are used as field test data herein. The study reach is located at 16 km north of Corrientes, NE Argentina (see Figure 2.3), close to its confluence with the Rio Paraguay.

The flow regime of the Río Paraná is characterized by summer floods between February and March and spring low water levels [192]. At the study reach, the channel pattern can be classified as multi thread/braided [192] and the river is approximately 2.5 km wide and 5-12 meters deep [198]. [198], surveyed a river bed 370 m wide, 1.2 km long, and 5-12 meters deep using a RESON 8125 multibeam echo sounder, and simultaneously obtained 3D flow information with an acoustic Doppler current profiler. In order to prepare the data for the present analysis, a structured 1-m grid was obtained from this survey. Thus, 370 longitudinal transects of 1028 points (1-m sampling interval and NR=100) were obtained.

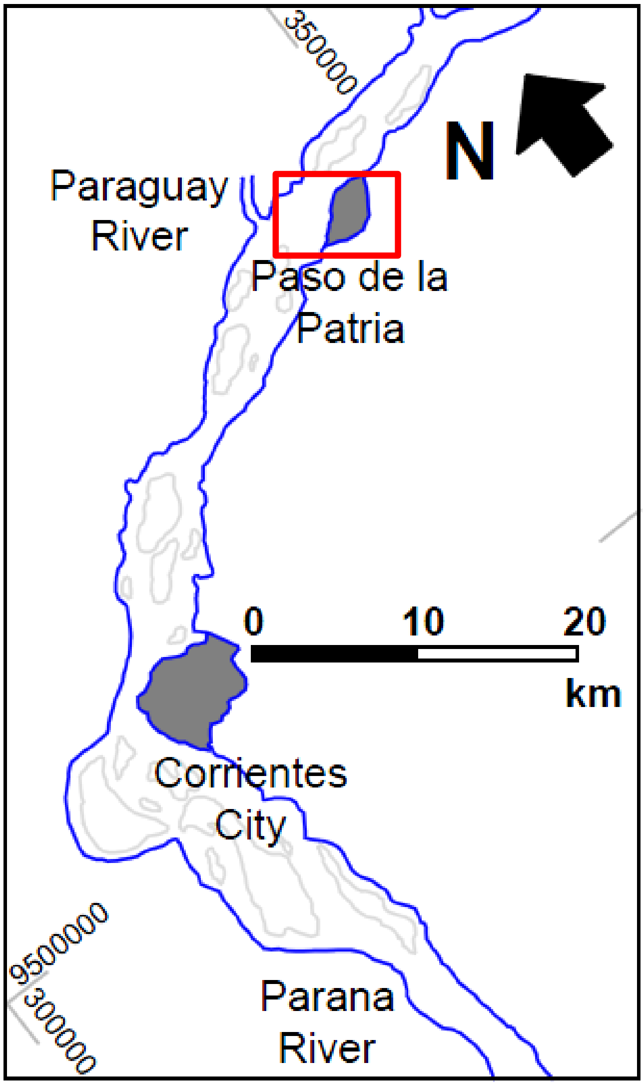

Figure 2.3: Location of fieldsite on the Río Paraná. The outline of islands are represented by thin gray lines.

The first transect ($j = 1$) was located at the northing 6977640 and the last ($j = 370$) at the northing 6978010 (Fig. 2.4). Figure 2.4 also shows that the bed morphology of the Río Paraná is characterized by 3D dunes with few straight crests that are subparallel, but with numerous undulating crests that possess saddles and lobes that occasionally bifurcate, especially in regions of deeper flow [198]. Inspection of the transects at the center and boundaries of the survey area (see Figure 2.5) shows that most of the dunes are highly asymmetric, with crestal platforms followed by marked changes of slope on the lee side (see [198] for more details). The larger bar feature is likely a forced bar created as flow is routed around a mid-channel bar to the north of the field survey area.

2.2.2.3 The Hierarchical Scale Discrimination of Bed Forms

There is currently no standard definition or methodology for the identification and discrimination of different bed form hierarchies (e.g. ripples, dunes, bars) generated on a natural mobile bed. As illustrated in Figure 2.2, various researchers have followed different approaches to quantifying and naming the geometric characteristics of bed forms. For example, bed form length has been defined as: i) the length of a line connecting two subsequent troughs, ii) the distance between two successive mean bed level up-crossings (points that reach the mean bed elevation by describing a positive slope), iii) the distance between two successive mean down-crossings (points that reach the mean bed elevation by describing a negative slope), and iv) the distance of two successive crests or two successive troughs (see Figures 2.2c, 2.2f and 2.2h). Similarly, bed form height has been defined as either the difference in elevation between a crest and its downstream trough, or as the shortest distance between a crestal elevation and the line between two troughs [249].

Likewise, some researchers (Figures 2.2d and 2.2f) have discriminated the length and amplitude of both the lee and stoss sides of dunes, which is more realistic because they represent markedly different regions of flow over asymmetrical dunes. In the lee side, a region of flow separation, with reattachment occurring approximately 4-8 dune heights downstream of the crest, and an expanding flow region are formed [35, 231]. These same gross patterns of flow also exist over the stoss and lee sides of the ripples, although dunes influence the

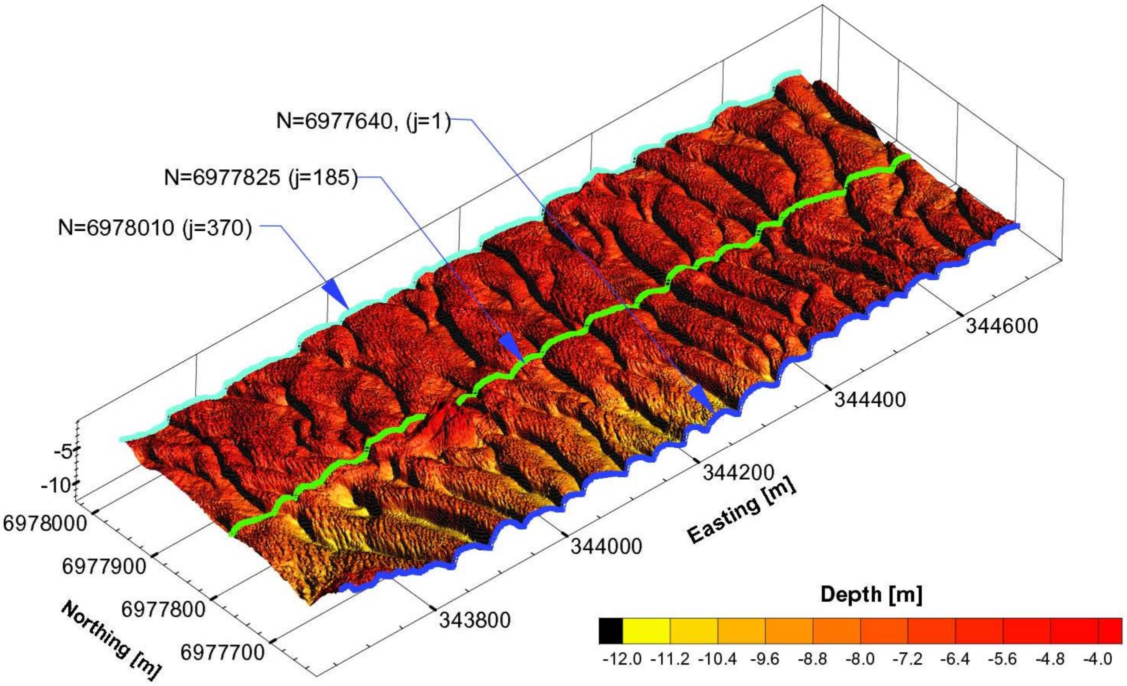

Figure 2.4: Bed morphology of the Río Paraná after [198]. Flow is from right to left. The water depth shown here was acquired in 2004 using a multibeam echosounder. Note the ubiquitous superimposition of three-dimensional small dunes on larger three-dimensional dunes. The cyan, green and blue lines represent the location of the profiles shown in Figure 2.5.

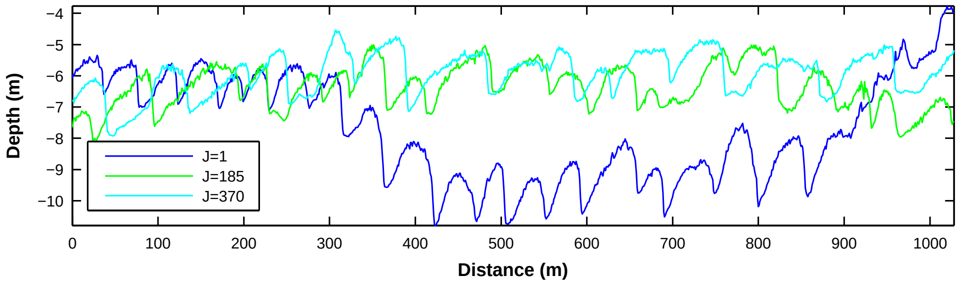

Figure 2.5: Bed form profiles (refer to sections j=1, j=185, and j=370 in Figure 2.4). Flow from left to right. Notice the existence of crestal platforms on dunes in the shallower areas.

water surface elevation and generate large-scale macro turbulence that may reach the water surface [138, 31, 36, 219].

Scaling remains a characteristic signature of bed forms [13], and both field and laboratory data often show multiple superimposed scales of bed forms. It is therefore frequently necessary to effectively subdivide these differing bed form scales into useful, quantified waveforms with different periodicities. Several experiments indicate that ripple heights and wavelengths are independent or slightly dependent on the flow depth [218, 83, 25, 213, 66, 62, 67, 65]; furthermore, the equilibrium ripple height is remarkably independent of the grain size [213]. [21] proposed arbitrary thresholds of 5, 10, 100 m for bed form length to differentiate "small", "medium" and "large" dunes, and proposed a classification scheme to distinguish ripples from dunes by defining ripples as features that have wavelengths generally less than 0.6 m. Although this criterion is based on an observational gap (which is currently being filled), it is often used as an accepted criterion for distinguishing between ripples and dunes but without any theoretical or causative process explanation. In practice, the discrimination between ripples and dunes is often taken as obvious, so that many authors fail to explain the criteria used for their discrimination in field and laboratory studies [117]. It is thus clear that the study of differing scales of bed forms requires both a standardized method for their quantification and description of their geometric descriptors.

The most widely-used definitions of various bed form geometric descriptors are given in Figures 2.2a, 2.2b, 2.2d, 2.2e and 2.2f, with the definitions in Figures 2.2c and 2.2h often not being used [251]. In order to standardize the symbolic representation of bed form geometric descriptors in bed form hierarchies, the symbols presented in Figure 2.6 are adopted herein. These symbols mainly agree with those presented by [251], although are applied on all bed form hierarchies and many have been widely used in past research, although they have not been used on a standardized basis (see Figure 2.2). Each descriptor is represented by a letter e.g. η (for bed form elevation), λ (for bed form length), Δ (for bed form height), and h (for water depth) followed by three indicators that represent [1] its position (as superscript, but avoiding this descriptor if the bed form elevation is represented) e.g. crest (c), trough (b), stoss (s), and lee (l); [2] its ordinal with respect to all the hierarchies (as sub-script and giving the first ordinal to the higher frequencies; e.g. ripples or small dunes); and [3] the

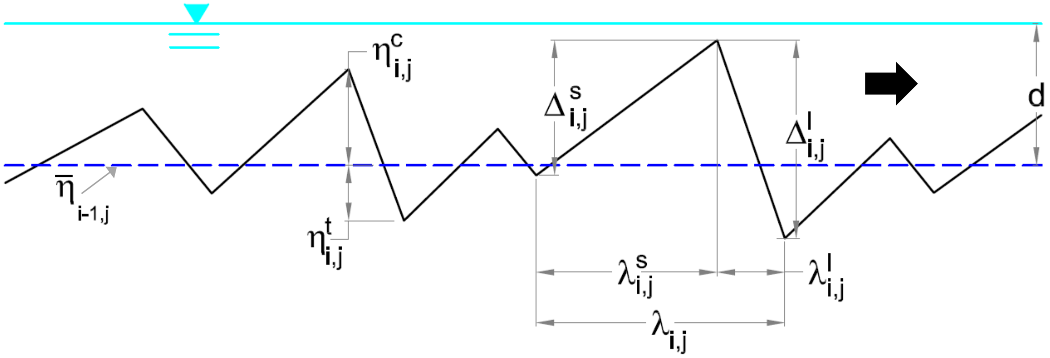

Figure 2.6: Symbolic representation of bed form descriptors for a given hierarchy adopted in the present study. These descriptors mainly agree with those presented by [251], but are applied on all of the bed form hierarchies. The bold black arrow represents the flow orientation and the blue dashed line the mean bed elevation of the preceding bed form scale.

total number of hierarchies (as a subscript). Therefore, the first hierarchy corresponds to ripples (or small dunes), the second to dunes, and the third to bars. Thus, for h (or η) the following relationship is always verified: $h = h_{1,3} + h_{2,3} + h_{3,3}$.

2.2.2.4 Method of Bed Form Scale Discrimination Investigations on bed form dynamics face the difficulty of defining an objective methodology to adequately quantify bed forms of different scale. This difficulty is principally due to the deterministic and stochastic nature of bed forms, where bed form profiles (BFPs) can further be viewed as a series of discrete bed form elements, continuous bed-elevation fields or some combination of these perspectives [65]. [251] proposed a methodology, named the bed form tracking tool, which uses spectral analysis and a weighted moving-average as a smoothing technique over BFPs that were previously verified to be statistically homogeneous. Generally speaking, such a methodology works according to the following procedure over individual BFPs: [1] it finds and replaces outliers, [2] a trend line is estimated based on the nature of the BFP (e.g. flume experiments or field measurements), [3] the BFP is detrended, [4] the BFP is filtered by applying a weighted moving-average filter, [5] the zero upcrossings (points where the filtered BFP crosses the zero line) and downcrossings (point where the filtered BFP crosses the zero line in downward direction; Figure 2.2g) are obtained, and finally [6] the geometric characteristics of the individual bed forms are estimated. This methodology performs reasonably well in minimizing any subjectivity in the estimation of the variability of bed forms, although it uses a filter that may not be completely suitable to detrend a BFP. A weighted-average is any average that has multiplying factors to give different weights to data at different positions in the sample window. Mathematically, the moving-average is a convolution of the data points with a fixed weighting function, and can therefore be considered as a rigid convolution function. The present work proposes the use of robust spline filters and the application of continuous wavelet transforms to perform a hierarchical discrimination and separation of different bed form scales. Discrete wavelet transforms and robust spline filters have been successfully used in the discrimination of engineering surfaces [211], which similar to bed forms are comprised of a range of spatial wavelengths. Engineering surfaces are split into form profiles that are similar to bars, waviness profiles that are similar to dunes and roughness profiles that are similar to ripples [211].

2.2.2.5 The Robust Spline Filter A fully automated robust spline procedure for uniformly-sampled datasets is used herein. The algorithm, based on a penalized least squares method, allows fast smoothing of uniformly sampled data y_i of n elements, by means of the discrete cosine transform.

To minimize or cancel the side effects of high leverage (a measure of the influence, between 0 and 1, of a given point on a fitting model due to its location in the space of the inputs), the algorithm constructs weights with a specified weighting function by using the current residuals and updating them, from iteration to iteration, until the residuals remain unchanged. In practice, five iterative steps are sufficient [93].

The algorithm uses a bisquare weighting function which is mathematically defined by Equation (2.3). The smoothed data $\hat{y}_i$ is determined by the parameter s which is a real positive scalar that controls the degree of smoothing. Thus, as the parameter s increases, the degree of smoothing of $\hat{y}_i$ also increases. It is important to note that in Equation (2.3).

u_i is the Studentized residual which is adjusted for standard deviation and leverage. The student residual is mathematically represented by Equation (2.4).

$$w_i = \begin{cases} rl\left[1 - \left(\frac{u_i}{4.685}\right)^2\right]^2 & \text{if } \left|\frac{u_i}{4.685}\right| < 1, \\ 0 & \text{if } \left|\frac{u_i}{4.685}\right| \geq 1 \end{cases} \tag{2.3}$$

$$u_i = \frac{r_i}{\hat{\sigma}\sqrt{1 - h_i}} \tag{2.4}$$

In the above equation $r_i = y_i - \hat{y}_i$ is the residual of the ith observation, h_i is its corresponding leverage and $\hat{\sigma}$ is a robust estimate for the standard deviation of the residuals given by 1.4826MAD, where MAD denotes the median absolute deviation. The leverage values h_i are all given by the diagonal elements of the hat matrix H. However, a faster and more economical alternative for robust smoothing can be obtained using an average leverage, which is mathematically defined by:

$$h_i = \frac{1}{n}\sum_i H_{ii} = \frac{Tr(H)}{n} \tag{2.5}$$

An approximated value for $Tr(H)/n$ is given by:

$$\frac{Tr(H)}{n} \approx r_i \sum_{i=1}^{n} [1 + s(2 - 2\cos((i-1)\pi/n)^2]^{-1} \tag{2.6}$$

The approximated Studentized residuals finally reduce to the expression:

$$u_i = r_i \left| 1.4826\text{MAD}(r)\sqrt{1 - \frac{\sqrt{1 + \sqrt{1 + 16s}}}{\sqrt{2}\sqrt{1 + 16s}}} \right|^{-1} \tag{2.7}$$

The use of the bisquare weightings in combination with the approximated Studentized residuals provides a robust version of the above-mentioned smoothing. An iteratively weighted robust version of the algorithm is used to deal with occurrences of missing and outlying values [93].

2.2.2.6 The Wavelet Transform

The unidimensional wavelet transform (WT) of a signal $f(x) \in L_2$ is obtained by the convolution of the signal and the wavelet function (WF) or mother wavelet $\psi(x)$ as expressed by Equation (4.1), where a is the scale parameter, b is the location parameter and $\bar{\psi}_{a,b}(t)$ is the complex conjugate of $\psi_{a,b}(t)$, as mathematically represented by Equation (4.2).

$$T(a,b) = \int\limits_{-\infty}^{\infty} x(t)\bar{\psi}_{a,b}(t)\,dt, \text{ for } a > 0, \tag{2.8}$$

$$\psi_{a,b}(t) = \frac{1}{\sqrt{a}}\psi(\frac{t-b}{a}) \tag{2.9}$$

According to the Parseval's theorem the same wavelet transform can be expressed as:

$$T(a,b) = \frac{1}{2\pi}\int\limits_{-\infty}^{\infty} \hat{x}(f)\bar{\hat{\psi}}_{a,b}(f)\,df \tag{2.10}$$

where $\hat{x}(f)$ and $\hat{\psi}_{a,b}(f)$ are the Fourier transforms of $x(f)$ and $\psi_{a,b}(f)$, respectively. The wavelet power spectrum is defined as $|T(a,b)|^2$.

Wavelets have advantages over traditional Fourier methods in analyzing physical situations where the signal contains discontinuities and sharp spikes. They also provide a flexible time or spatial-scale window that is localized on time or space-scale planes [211]. The most widely-used continuous WFs are the Morlet and the $n-th$ derivatives of the Gaussian (DOG). Among the DOGs, the Ricker or so- called Mexican hat wavelet represents the second derivative. The selection of the appropriate WF depends on both the mathematical and physical nature of the parameter being analyzed. Different categories of wavelet, and various types of wavelets within each category, provide a multitude of options to choose from when analyzing a process of interest [89]. The complex Morlet function is expressed by Equation (2.11) in its simplest form (where k_0 is the central frequency, which is generally assumed to be 5 or bigger to satisfy the wavelet admissibility condition). The Ricker function, which is a real function, is mathematically represented by equation Equation (2.12).

$$\psi(t) = \frac{1}{\pi^{1/4}}.e^{i2\pi k_0 t}e^{-t^2/2} \tag{2.11}$$

$$\psi(t) = (1 - t^2).e^{-t^2/2} \tag{2.12}$$

According to the uncertainty Heisenbergs principle, there is a lower limit to the product of frequency and time resolution. Thus, as time resolution is improved, frequency resolution degrades and vice versa [14].

The Morlet function provides lower area of the Heisenberg cell than the DOGs WT and retrieves accurate wavelengths at higher signal-to-noise ratios and lower sample frequencies. The wavelet analysis of the synthetic signals confirms this. Morlet WF (see Figure 2.7) retrieves frequencies of the order of ripples for sampling frequencies below 0.25 m, and that the efficiency of the DOGs improves as the order of the derivative is increased. This efficiency of the Morlet WT is particularly important to retrieve frequencies of the order of ripples. Therefore, it is used for all the estimations with wavelet transforms. They are performed by using a modified version of the wavelet software provided by [243].

2.2.2.7 Discrimination Method For each synthetic signal and Río Paraná BFP, the separation procedure encompasses the following steps and is valid for either h or η signals:

1. The outliers are identified and replaced by the mean water depth h (or bed form elevation η).

2. The continuous wavelet analysis is performed on the given h (or η) signal (see Figures 2.8 and 2.9). The global wavelet transform spectrum (see Figures 2.8c and 2.9c) provides information to find the wavelength (192 m for signal SSNR80SNR489 and 337 m for j=100) of the wave that underlies the dunes that have a mean wavelength of approximately 10 m and 62 m, respectively.

3. The original synthetic signal (η in Figure 2.11) and BFP (h in Figure 2.10) are filtered by using the robust spline filter with several values of the parameter s. A wavelet transform analysis is then performed for each filtered signal and the one that has a mean

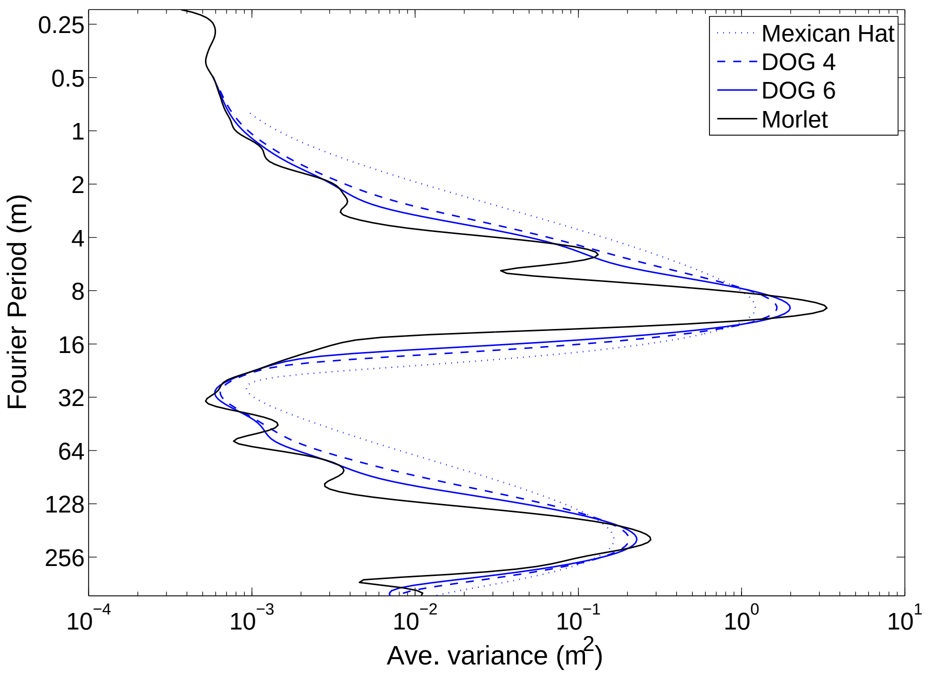

Figure 2.7: Wavelet global spectrum for Morlet and the derivatives of the Gaussian wavelet functions for signal SSNR100SNR494. The former retrieves higher frequencies such as the synthetic ripples with ∼0.30m of wavelength, at any signal to noise ratio and Nyquist ratio. It is important to note that the 5m wavelength is imposed by the synthetic ripples.

(a) Fig7−ParanaXS100MORLET6

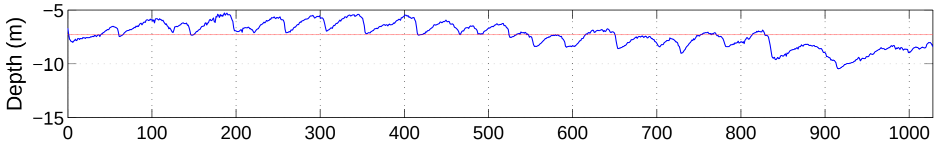

(b) MORLET 6 wavelet power spectrum

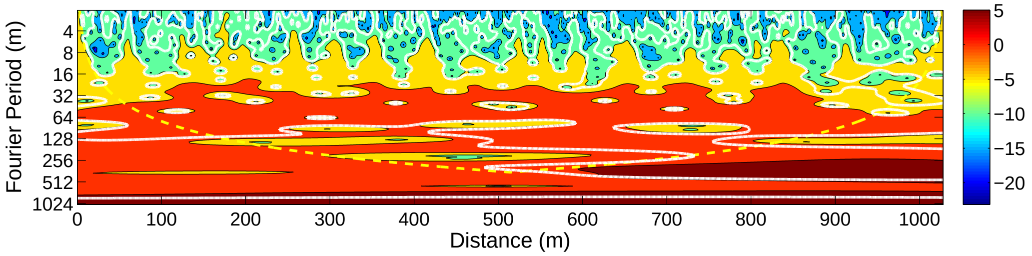

(c) Global WT spectrum α=1

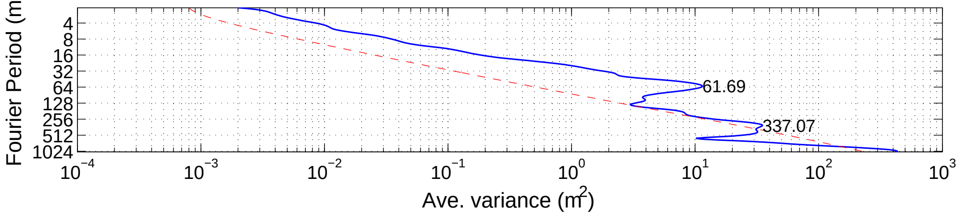

Figure 2.8: Wavelet analysis output for section j=100. Bed form migration from left to right. (a) Bed form profile at section j=100, (b) contours of the wavelet power spectrum using the Morlet wavelet function (the dotted yellow line represents the cone of influence and the bold contours are the contours at 95% confidence limits), and (c) global wavelet power spectrum showing the main frequencies in section j=100 (the dotted red line represents the 95% confidence interval; thus, the peaks located at the right side of such line are the wavelengths are at 95% of the confidence level). The higher frequency, 337 m, is used by the program to discriminate the third bed form hierarchy (bars).

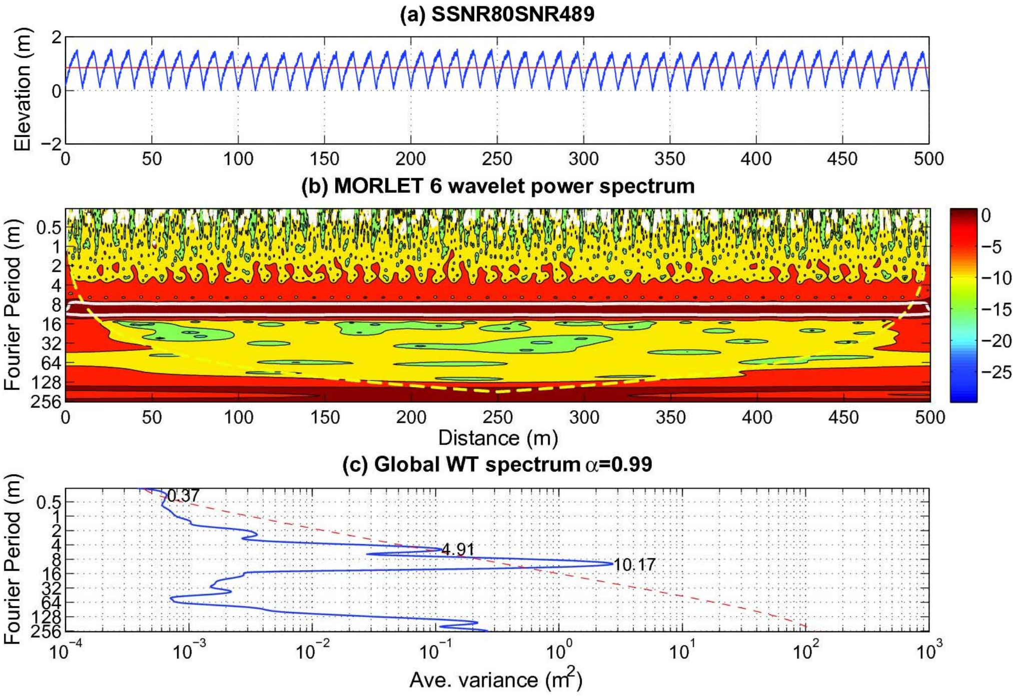

Figure 2.9: Wavelet analysis output for synthetic signal SSNR80SNR489 (refer to Fig. 2.8 for details about the definition of the graphical representations). Notice the limitation of the wavelet transforms to retrieve wavelengths that are located closer to the edge of the cone of influence.

wavelength closest to 192 m (for SSNR80SNR489) or 337 m (for j=100) is found. These signals become the third level of bed form discrimination ($h_{3,3}$ in Figure 2.10 and $\eta_{3,3}$ in Figure 2.11).

4. $\hat{h}_3$ (or $\hat{\eta}_3$ for the synthetic signals) is defined as $\hat{h}_3 = h - h_{3,3}$ and contains the signal of dunes with superimposed smaller dunes (or superimposed ripples for the synthetic signals).

5. The $\hat{h}_3$ signal (or $\hat{\eta}_3$ for the synthetic signals) is filtered by using the robust spline filter with different values of the parameter s, to obtain several dune-like signals, named $\hat{h}_2(s)$. For the case of synthetic signals several ripple-like signals, named $\hat{\eta}_2(s)$, are obtained.

6. The $\hat{h}_3$ signal is subtracted from each $\hat{h}_2(s)$ to obtain a set of smaller-dune-like signals, named $\hat{h}_1(s)$ (or ripple-like signals, named $\hat{\eta}_1(s)$ for the synthetic signals).

7. A wavelet analysis is performed on each $\hat{h}_1(s)$ and this determines a mean wavelength of 0.6 m (an arbitrary threshold that defines ripples) and 5m (an arbitrary threshold that defines small dunes) for SSNR80SNR489 and j=100, respectively. These criteria are, as stated above, the objective criteria used to define ripples and small dunes. The chosen signal then becomes the first level of the bed form discrimination ($\eta_{1,3}$ in Figure 2.11 and $h_{1,3}$ in Figure 2.10), and the corresponding $\hat{\eta}_2(s)$ and $\hat{h}_2(s)$ becomes the second level of bed form separation ($\eta_{2,3}$ in Figure 2.11 and $h_{2,3}$ in Figure 2.10).

2.2.3 Results

2.2.3.1 Accuracy of the Method The accuracy of the method is assessed by analyzing the synthetic signals. Our results reveal that the method provides a high accuracy in retrieving information from the bar and dune form scale signals. A cross-correlation analysis of the retrieved and actual bar and dunes signals is persistently higher than 0.9 at lags equal

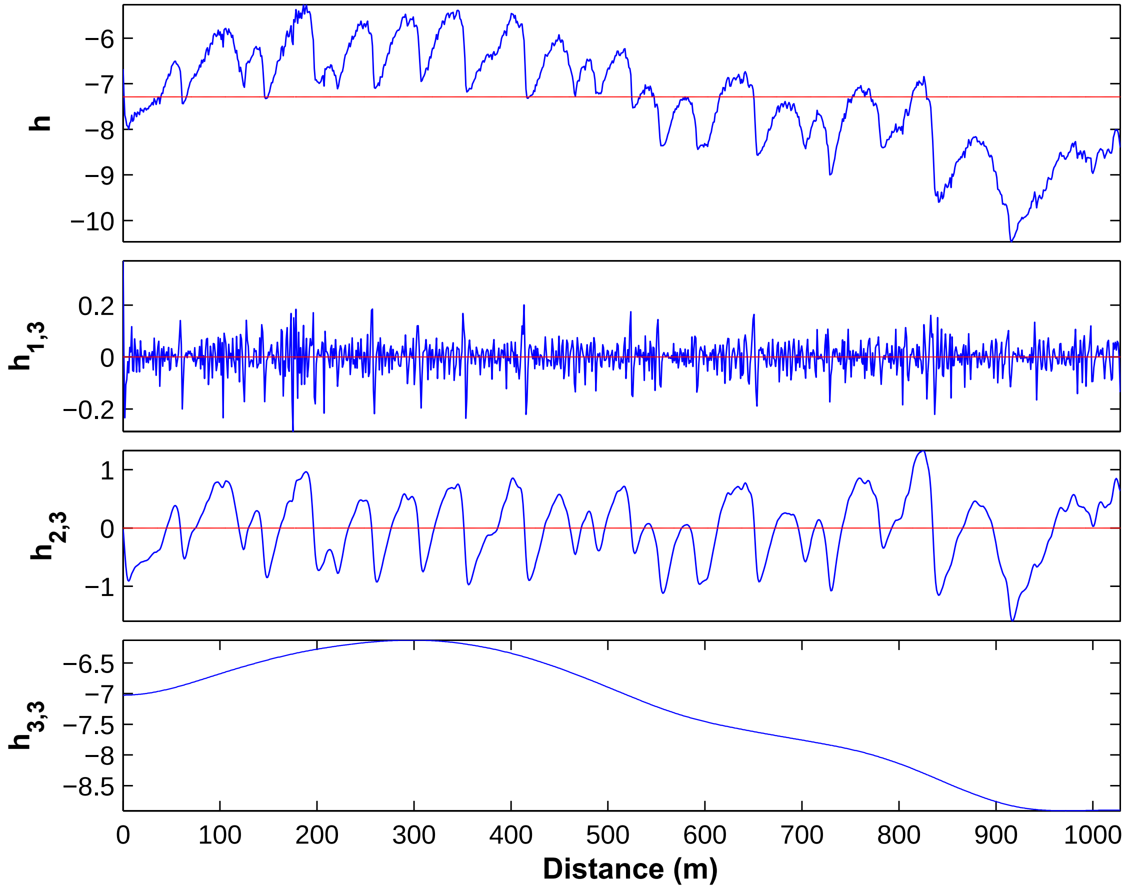

Figure 2.10: Wavelet-Spline discrimination output for section j=100. $h_{1,3}$ represents the first bed form hierarchy (small dunes), $h_{2,3}$ represents the second bed form hierarchy (large to medium size dunes), and $h_{3,3}$ represents the third bed form hierarchy (bars).

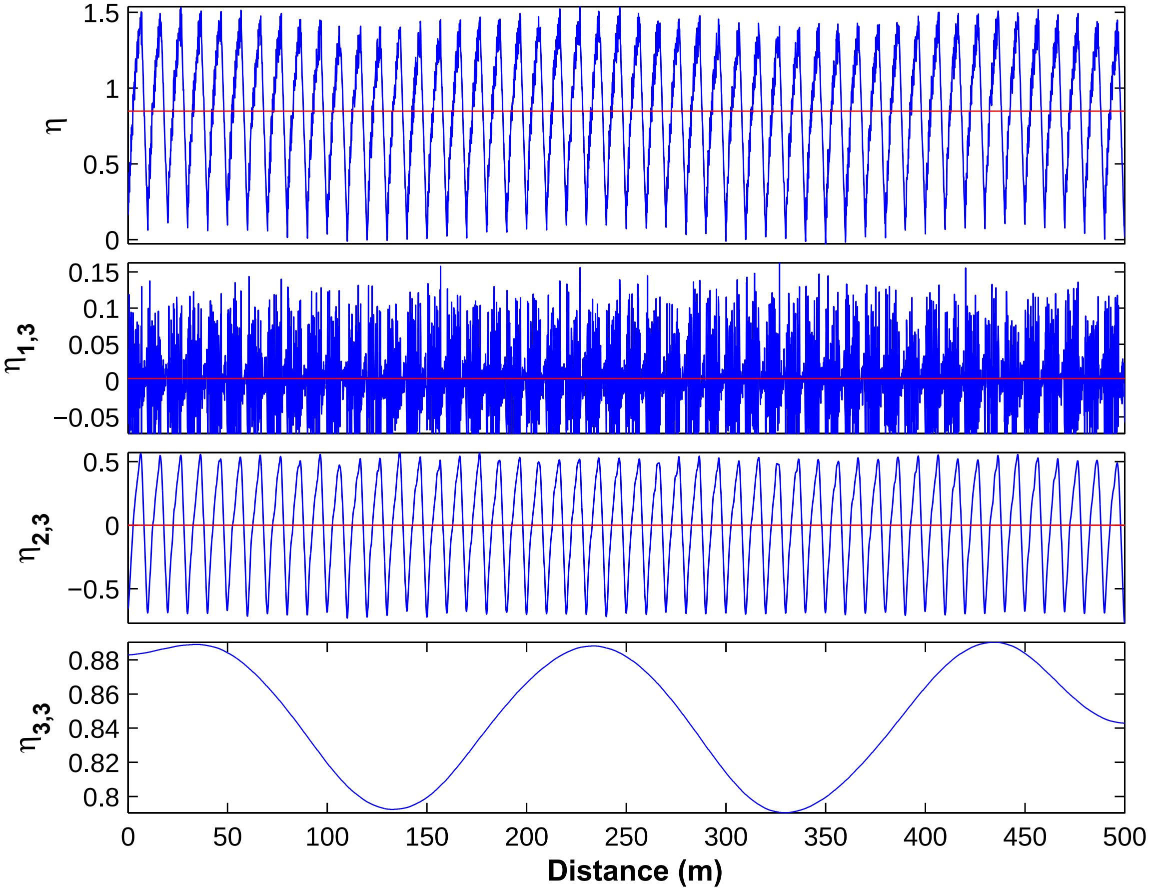

Figure 2.11: Wavelet-Spline discrimination output for the synthetic signal SSNR80SNR489. $\eta_{1,3}$ represents the first bed form hierarchy (ripples), $\eta_{2,3}$ represents the second bed form hierarchy (dunes), and $\eta_{3,3}$ represents the third bed form hierarchy (bars).

to zero for NR>25 at any SNR (see Figures 2.12b-c and Figures 2.13b-c). Likewise, their standard deviation ratios (Figure 2.14b and Figure 2.14c) are markedly closer to a value of unity for NR>25 at any SNR.

Filters necessarily induce some deformation on the signals [211, 180], and this is critical for retrieving higher-frequency ripple signals. A closer analysis of these signals indicates that the cross-correlation between the actual and recovered signals is higher than 75% for NR>25 (see Figure 2.12a), and that the robust spline filter does not lag the ripple signal as shown in Figure 2.13a. However, the robust spline filter does distort the amplitudes (see Figure 2.14a), especially for NR>25 and SNR<5, with most of the amplitude deformations occurring in the bed form troughs. It is important to note that among the different filters, the robust spline filter minimizes such trough deformation [211]. Our results reveal that this limitation of the filters is improved when the points of the ripple signal with negative elevations, and below 2.5 times the standard deviation threshold, are considered as outliers, and are therefore fixed at such a threshold.

In order to assess the reproducibility of the ripple frequencies, the reproducibility ratio, defined as the ratio between the number of common peaks (of the actual and retrieved ripple signals) detected in at least 50% of the whole spectra and the total number of peaks corresponding to the number of peaks detected across all the spectra [180], was quantified. These results highlight that the reproducibility is higher than 70% for NR>25 (Figure 2.15).

Synthetic data that exhibits self-similarity was used. The synthetic data is comprised by ripples (Gaussian distributed), small and medium dunes (whose height follows the Gamma distribution) and bars (generated by using the sinusoidal equation described above. The methodology also shows good performance, with a higher efficiency being observed in bars and dunes than for the case of ripples. Figure 2.16 presents an instance of the synthetic signal and a set of results from the analysis. They indicate that the best results are achieved for $NR > 30$. This type of signals were also used to generate two-dimensional synthetic bed form data (see Section 5.3.1.2).

2.2.3.2 Discrimination of Bed Form Scales at the Fieldsite

After the procedure outlined above is applied to the 370 fieldsite BFPs, various scales of bed forms are found

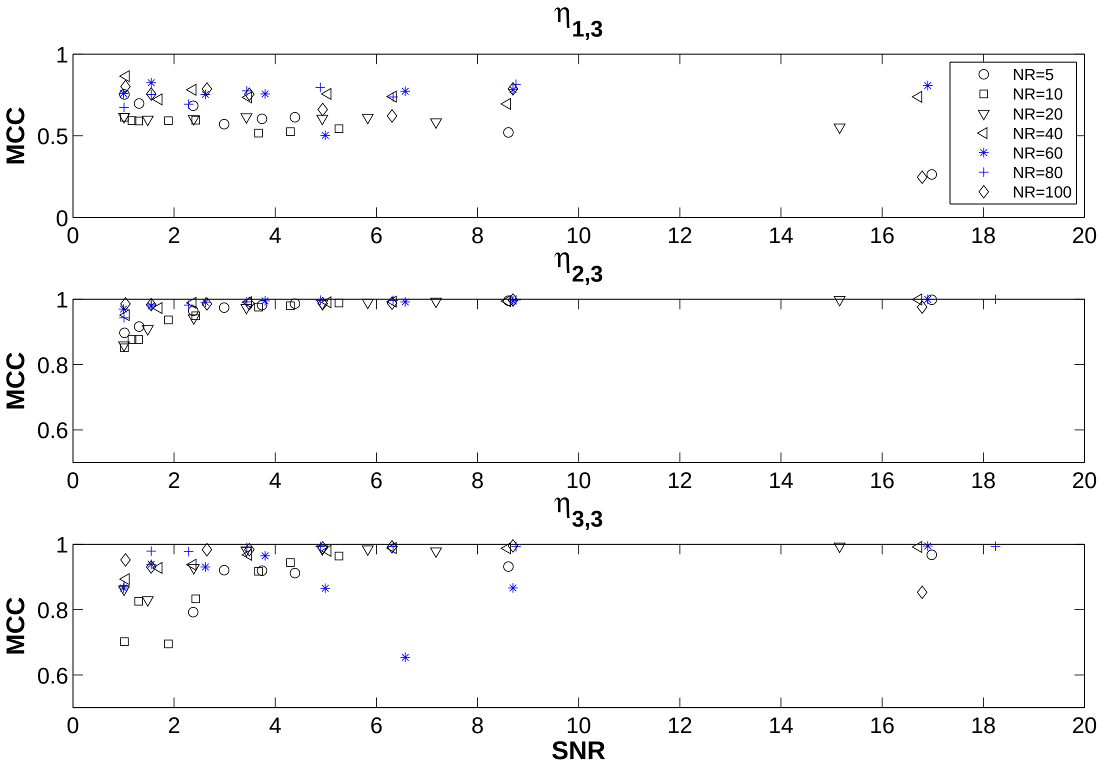

Figure 2.12: Maximum cross correlation(MCC) between retrieved and the actual (a) ripple, (b) dune, and (c) bar synthetic signals.

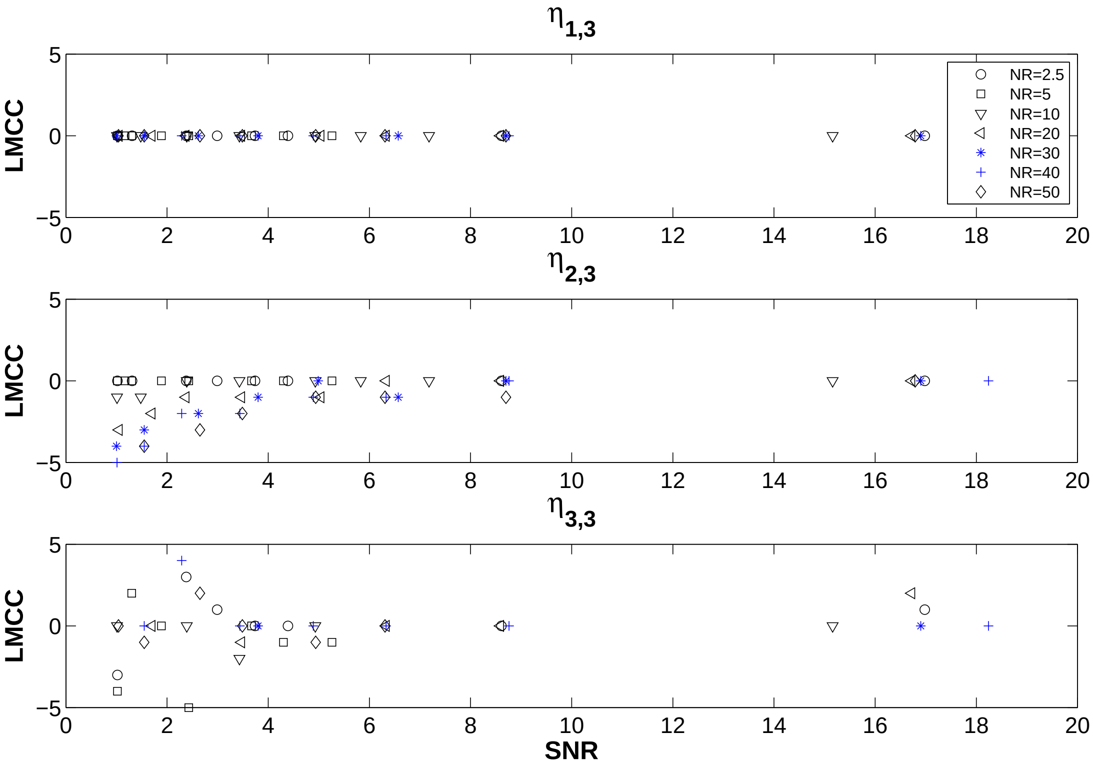

Figure 2.13: Lag at the maximum cross correlation (LMCC) between retrieved and actual (a) ripple, (b) dune, and (c) bar synthetic signals.

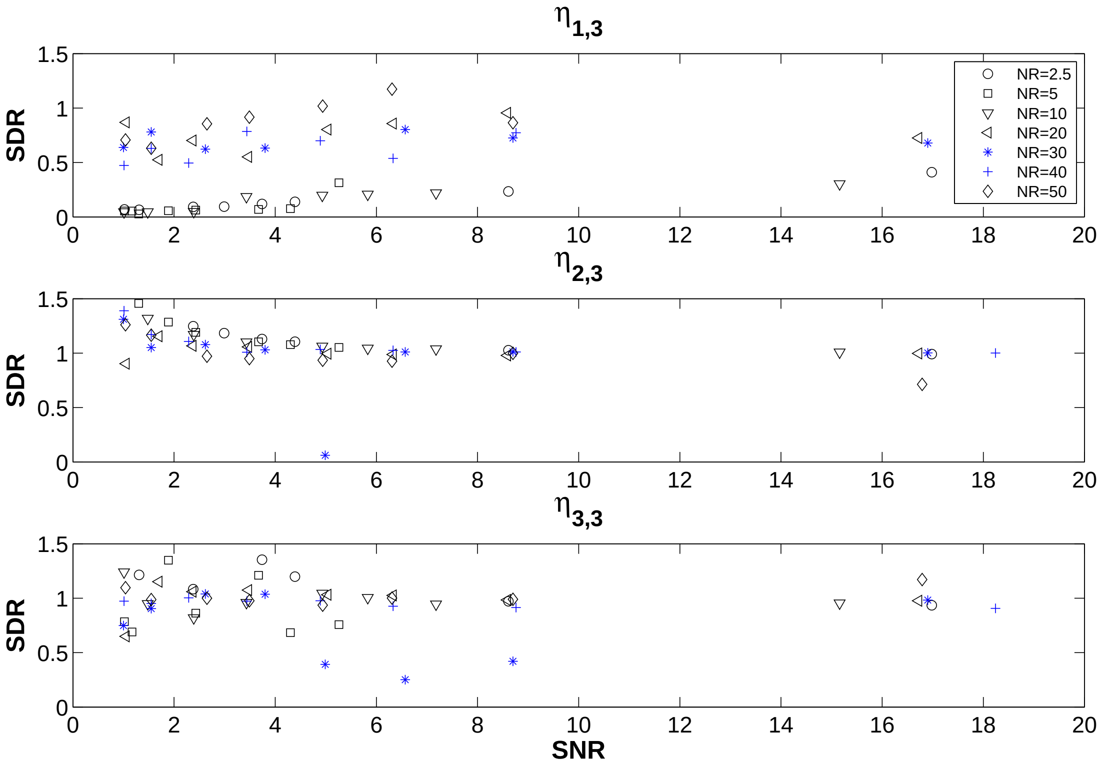

Figure 2.14: Standard deviation ratio (SDR) between retrieved and actual (a) ripple, (b) dune, and (c) bar synthetic signals.

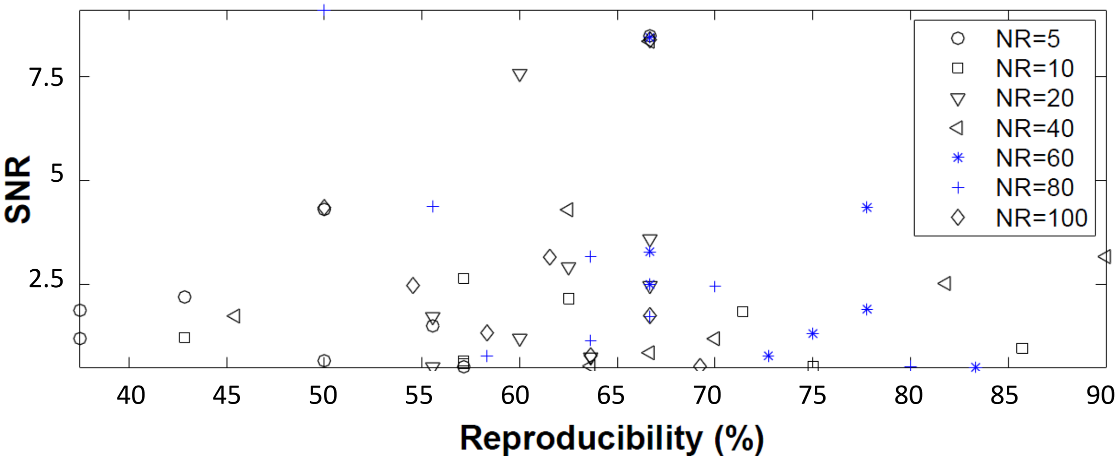

Figure 2.15: Reproducibility of the synthetic ripple frequencies.

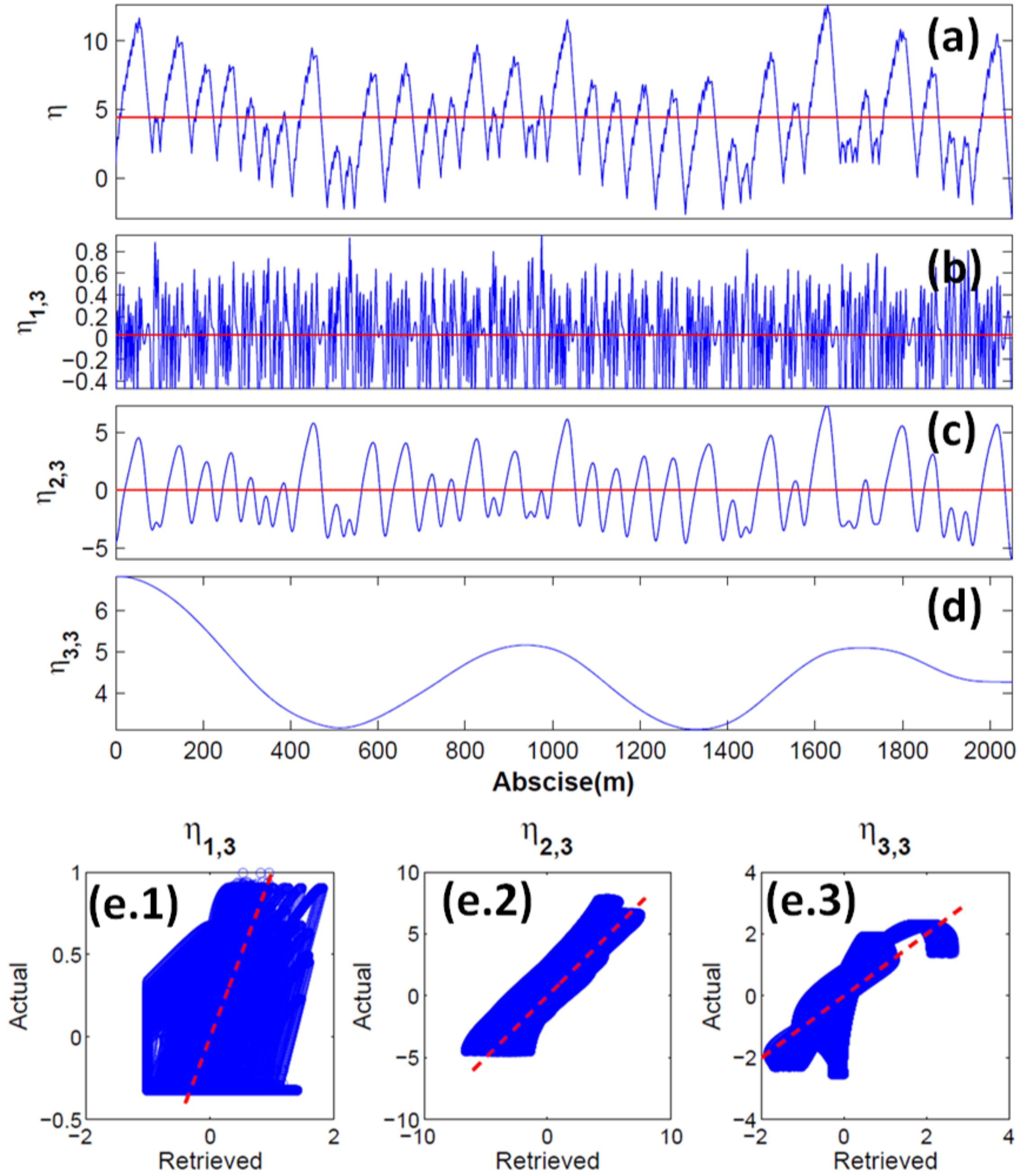

Figure 2.16: Discrimination of synthetic signals exhibiting self similarity. (a) Synthetic signal comprised by ripple, small dunes, medium dunes and bars; (b) retrieved ripple signal, (c) retrieved dune signal; (d) retrieved bars signal; (e.1) retrieved ripples, (e.2) retrieved dunes: and (e.1) retrieved bars.

(Figs. 2.17-2.19), respectively. Figure 2.17b shows that for the case of markedly 3D medium and large dunes, the small dunes with higher amplitudes are concentrated near to the troughs and their amplitudes tend to increase as they near the crests of the larger dunes, denoting that the process of bed form amalgamation is prevalent for 3D dunes. This pattern is absent for large dunes that are more 2D and with crests sub-parallel with their neighbors, and may be explained by the fact that obliquity of the crestline influences the length of any separation zone and thus influences the magnitudes of the leeside Reynolds stresses, drag coefficients and the dispersal patterns of sediments [35]. Indeed, Figure 2.18 shows that crestal platforms are commonly present over 3D large dunes. According to [168] and [253], turbulence generated by 3D dunes is weaker than the 2D case, due to the generation of secondary flows over the 3D forms, perhaps highlighting a process of the crest having conditions transitional to an upper stage plane bed. Figure 2.19 shows that the bar is highly variable along the survey area, and thus a linear representation of this feature is too simplistic.

A wavelet analysis using the Morlet wavelet function (Eq. 2.11) on the $\hat{h}_3$ signals was also conducted, and the average wavelet power spectrum, namely the power Hovmöller, for 4-8 m and 8-16 m bands was obtained. The power Hovmöller is a 2D contour plot used to display the wavelet variance of the bed form profile along the x-axis at distinct transverse locations, y. This 2D contour plot allows assessment of the variability of the power distribution in both the longitudinal and transverse directions, as well as isolation of features characterized by a certain range of dimensions, such as wavelength [58]. Figure 2.20a indicates that the higher frequency bed forms are located mainly in the troughs and at the lower portions of the stoss sides of the larger dune forms. Likewise, Figure 2.20b indicates that the second band is densely distributed with large dunes, especially close to the troughs.

Since the methodology analyses stream wise transects, it has the potential to locate the crests and troughs of the bed form hierarchies present in the study area even for temporal bed form analyses, although it is limited in fully describing the 3D nature of the bed forms.

2.2.3.3 The Statistics of Bed Form Features The data for different sized bed forms, filtered as the signal of the smallest bed forms over the stoss side of the larger dunes are

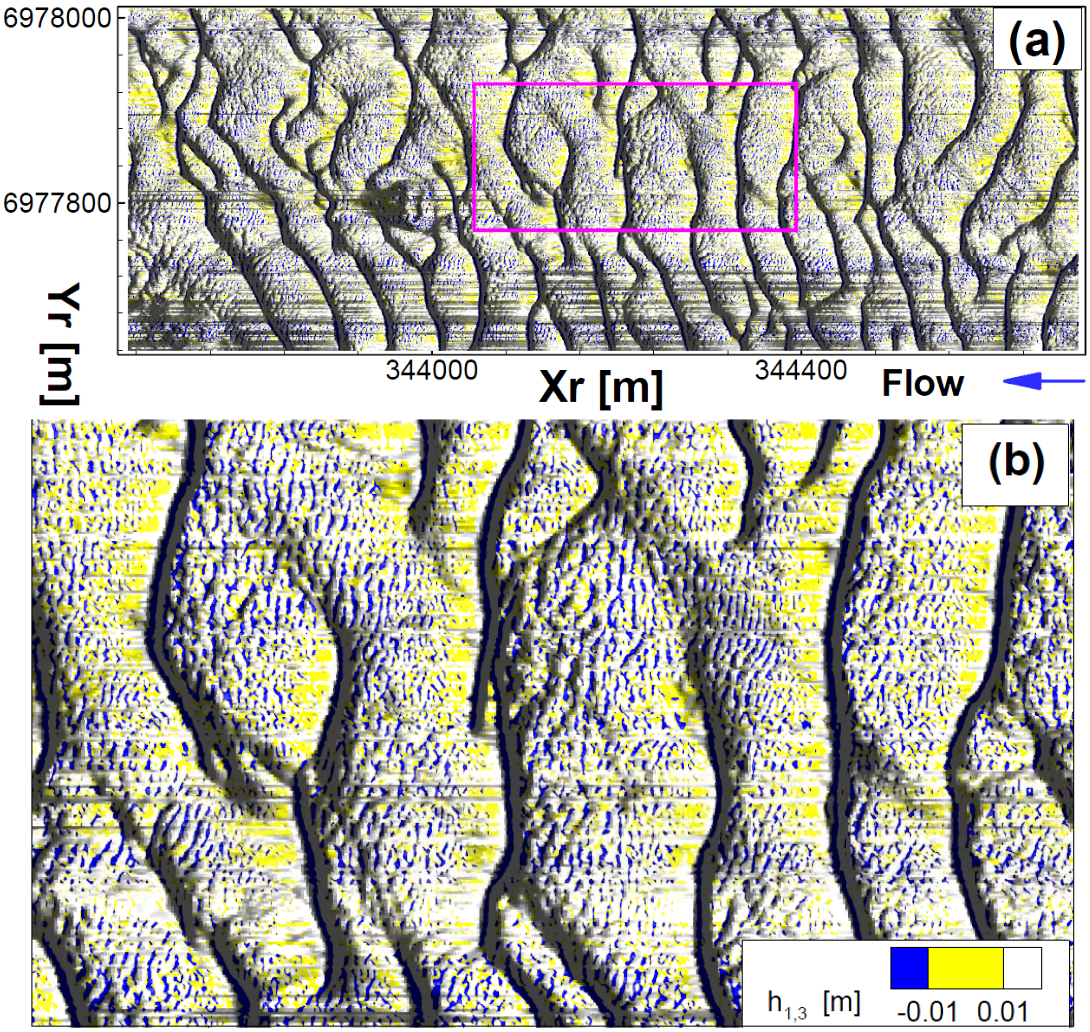

Figure 2.17: (a) $h_{1,3}$ (small dunes) data of the Río Paraná survey, and (b) inset of small dunes superimposed on markedly three-dimensional larger dunes. Here, the smaller dunes (yellow areas) concentrate in the trough region of the larger dunes and grow in amplitude as they get closer to the crests of the larger bed forms. Flow is from right to left.

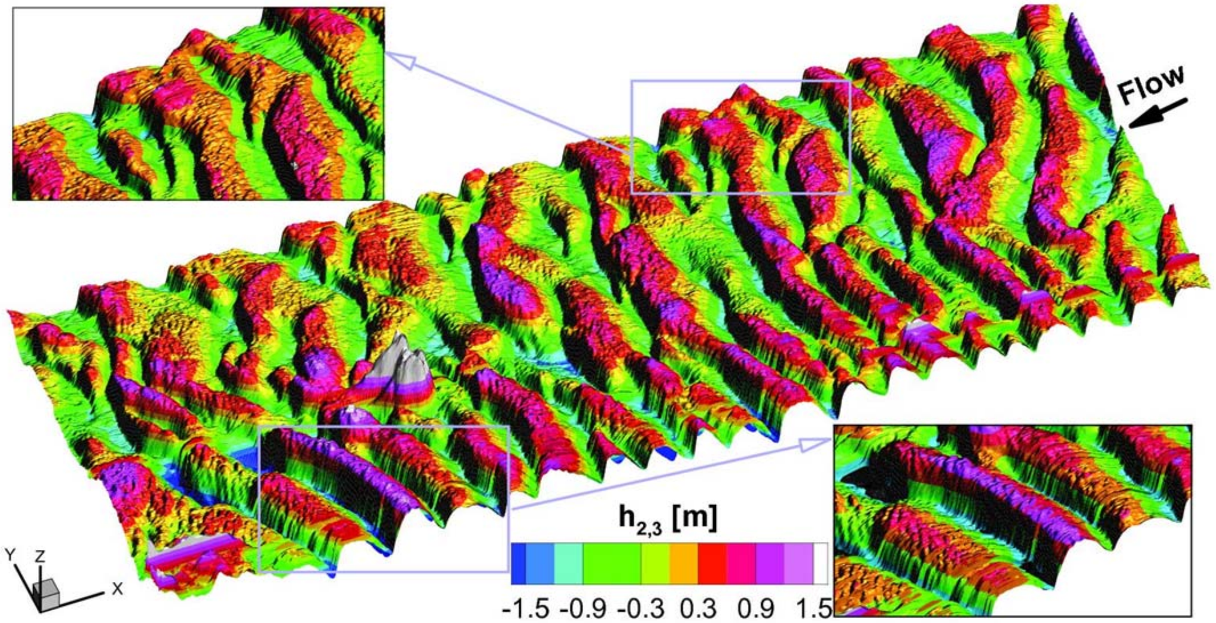

Figure 2.18: $h_{2,3}$ (medium to large dunes) data of the Río Paraná survey. Note that crestal platforms are developed on the shallower, markedly three-dimensional, larger dunes. Subparallel larger dunes tend to be more two-dimensional. Bed forms migration from right to left.

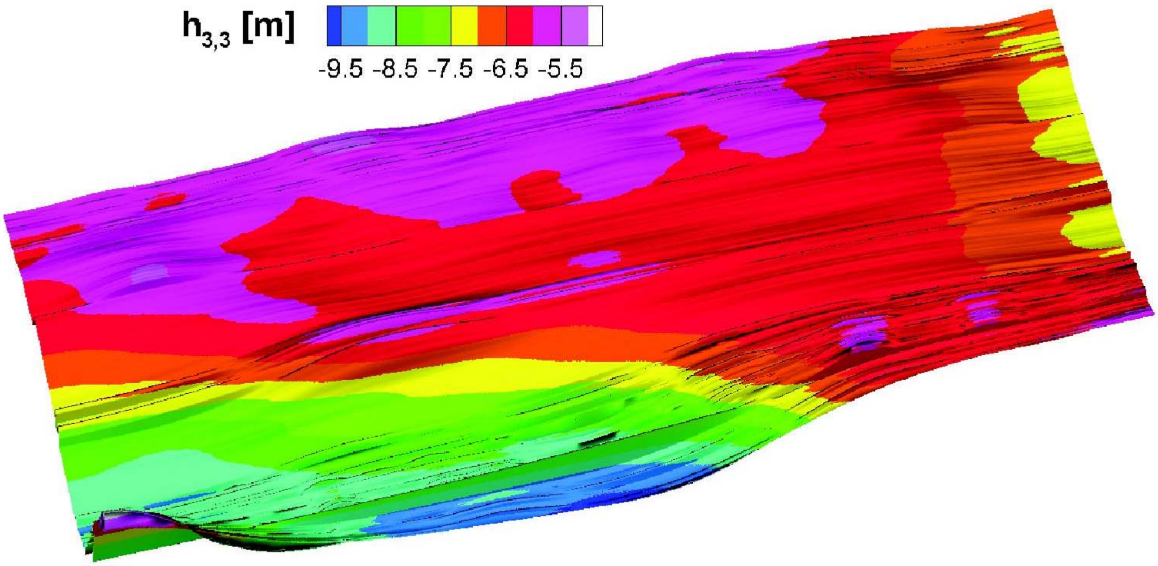

Figure 2.19: $h_{3,3}$ (bars) data of the Río Paraná survey. Flow is from right to left. This bed form hierarchy imposes a highly non-stationary condition on the BFPs. A linear representation of this feature would be too simplistic for this survey.

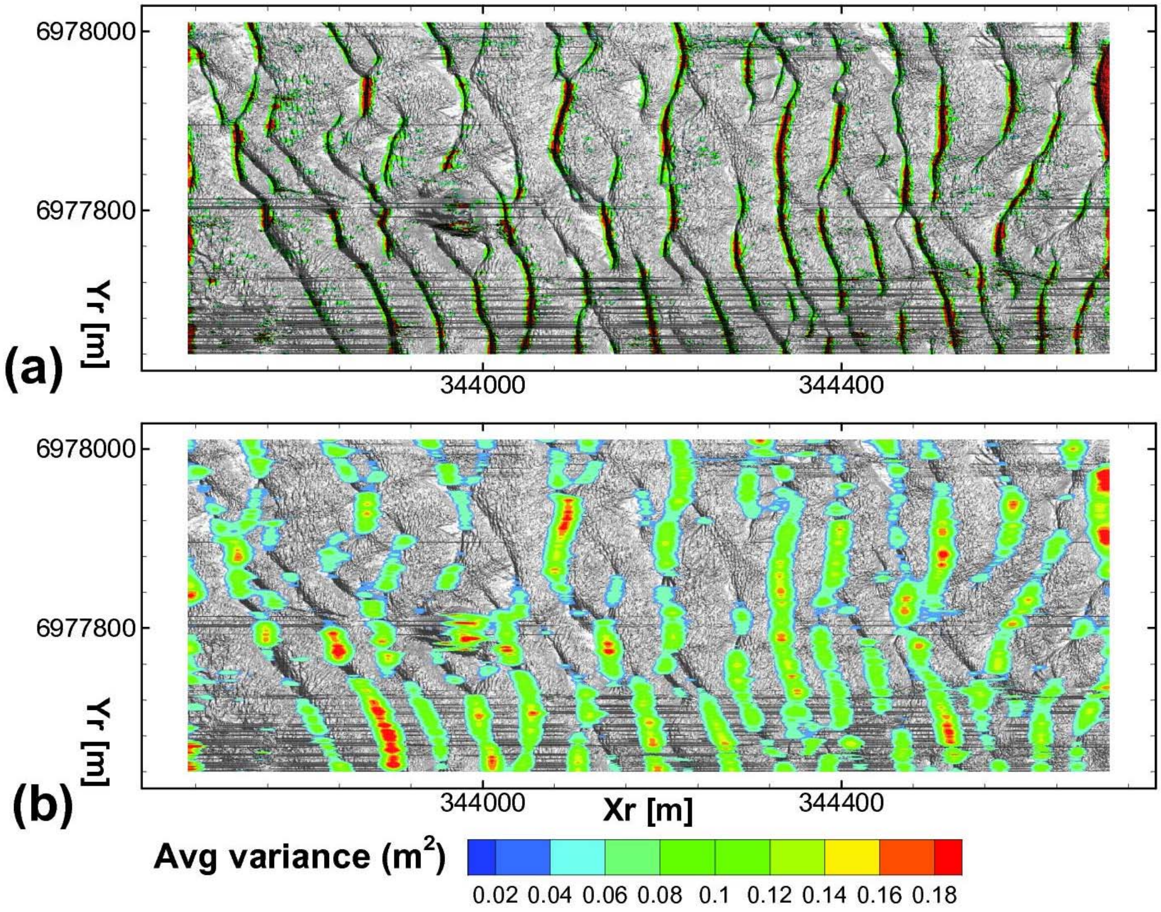

Figure 2.20: Power Hovmöller of the averaged wavelet power spectrum for two scale bands of the $h_{2,3}$ swath: (a) $[4-8]$m (small dunes), (b) $[8-16]$m (medium size dunes). In all cases, the contours present the variance with a 95% confidence level.

analyzed statistically later. The histograms of the dune descriptors (see Figure 2.21a-f) show that there is a marked difference in the distribution of the wavelength of smaller features on the lee and stoss sides. Similar results have been reported by [113], [92], [132] and [136]. Our results also indicate that there is a strong correlation between the wavelength and amplitude of the superimposed smaller dunes on the stoss side; conversely, the same parameters are not correlated on the lee side.

The probability distribution functions (PDFs) of the dimensionless descriptors of the large and small dunes, together with the Weibull, Gaussian, Gamma, GEV, and Pareto distributions, are shown in Figure 2.22. In each case, the dimensionless value of each descriptor is defined as the descriptor divided by its mean value. The goodness of fit of some distribution functions was also evaluated by the normalized Anderson-Darling test (normalized with the Gamma A2, denoted A2*; see Table 2.1) that allows testing of a wider range of distributions when some of the parameters may not be known [75]. The minimum A2* value denotes the best fit to the PDF. In most of the cases (Figs 2.22a-2.22d and Table 2.1), the Gamma distribution provides the best goodness of fit. Likewise, all the parameters show a positive skewness and leptokurtic distribution. A similar analysis was performed on the small dune sample population (Figs 2.23a and 2.23b; Table 2.1). The histograms (Fig. 2.21d-f) demonstrate that the wavelength of these bed forms on both the stoss and lee sides present the characteristics of discrete variables. On the other hand, the absolute value of their amplitudes reveals that the characteristic amplitude is approximately 0.05 m. These slopes, when compared to that of the dunes, present lower values for the stoss side but similar values in the lee side. The Gamma distribution presents the best goodness of fit, with the kurtosis being positive and greater than that of the larger dunes, and possessing a leptokurtic distribution.

Thus, it is important to note that the recurrence of the Gamma PDF as the best describer of the bed form descriptors probability density justifies normalizing the Anderson-Darling test results with the Gamma's A2.

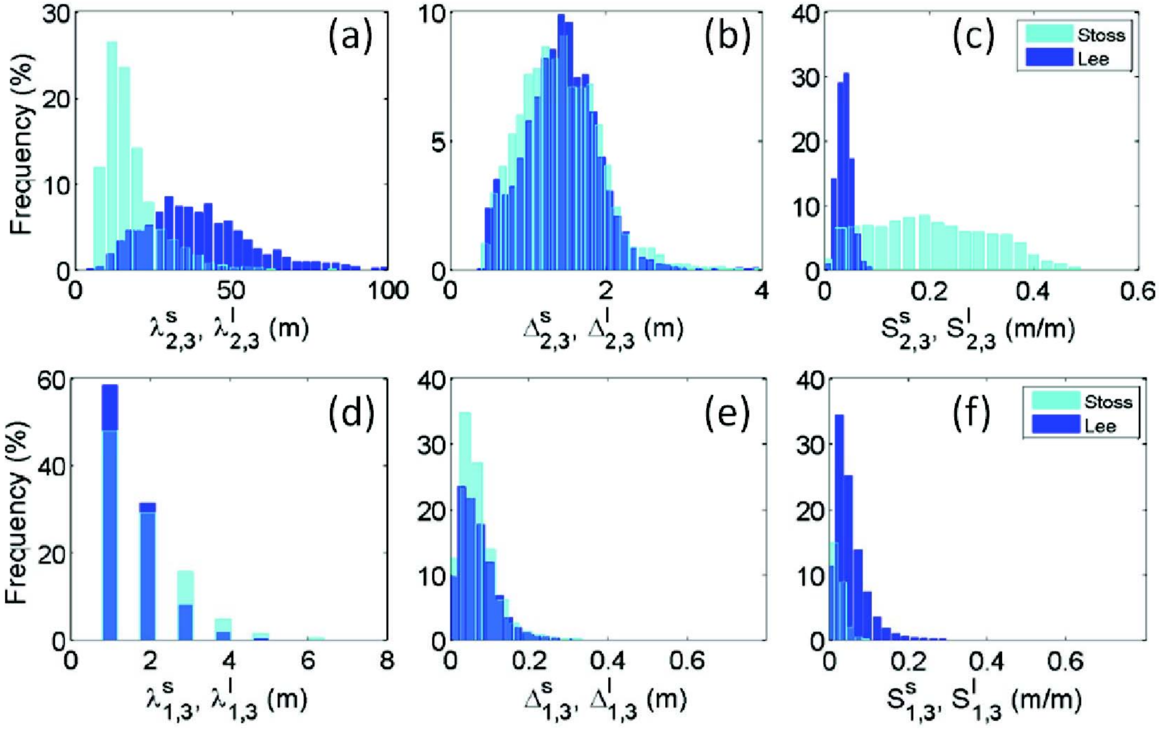

Figure 2.21: Histograms of the large dune descriptors: (a) The dimeswavelength of the lee side ($\lambda^l_{2,3}$) shows higher variability than that of the stoss side; (b) the amplitudes of the stoss and lee sides ($\Delta^s_{2,3}$ and $\Delta^l_{2,3}$) show similar distribution of frequencies; (c) the slope of the stoss side ($S^s_{2,3}$), shows an almost symmetrical distribution; however, the slope at the lee side ($S^l_{2,3}$), that is closely related to the angle of repose of the sediment material, shows higher variability. Histograms of the small dunes descriptors: (d) the wavelengths at the stoss and lee sides ($\lambda^s_{2,3}$ and $\lambda^l_{2,3}$) in the continuity of the interval is strongly determined by the sampling frequency; (e) the amplitudes at the stoss and lee sides ($\Delta^s_{2,3}$ and $\Delta^l_{2,3}$) shows similar distribution. The small dunes, that represent shorter life-span structures, appear not to be related to the angle of repose of the sediment material any more; (f) no markedly variability between the lee and stoss slopes.

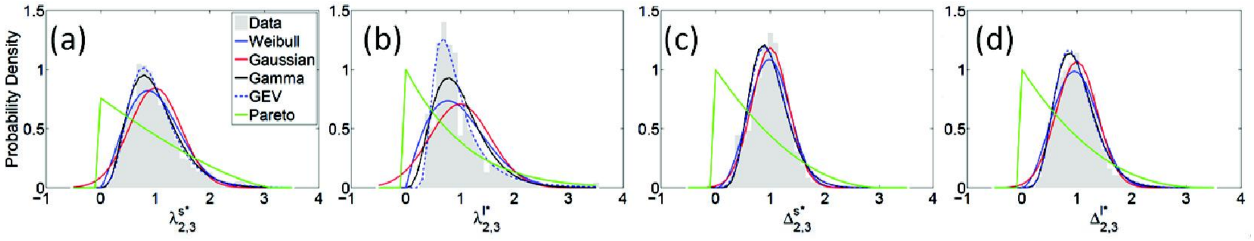

Figure 2.22: Probability distribution of the larger dunes dimensionless descriptors: (a) stoss amplitude, (b) lee amplitude, (c) stoss wavelength, and (d) lee wavelength.

Table 2.1: Normalized Anderson-Darling test results. The minimum value defines the standard probability density function that best describes a given normalized bed form geometric descriptor.

Descriptor	Gaussian	Weibull	Gamma	LEV
$\Delta^{l*}_{1,3}$	50.9	5.9	1.0	5.2
$\lambda^{l*}_{1,3}$	1.0	0.9	1.0	1.1
$S^{l*}_{1,3}$	9.4	1.4	1.0	3.2
$\Delta^{s*}_{1,3}$	45.7	3.4	1.0	6.1
$\lambda^{s*}_{1,3}$	0.9	0.9	1.0	1.2
$S^{s*}_{1,3}$	29.0	3.0	1.0	5.4
$\Delta^{l*}_{2,3}$	2.5	3.0	1.0	2.3
$\lambda^{l*}_{2,3}$	3.4	2.2	1.0	0.7
$S^{l*}_{2,3}$	0.5	0.5	1.0	0.6
$\Delta^{s*}_{2,3}$	0.2	0.7	1.0	1.7
$\lambda^{s*}_{2,3}$	13.3	6.5	1.0	0.6
$S^{s*}_{2,3}$	8.0	14.1	1.0	2.5

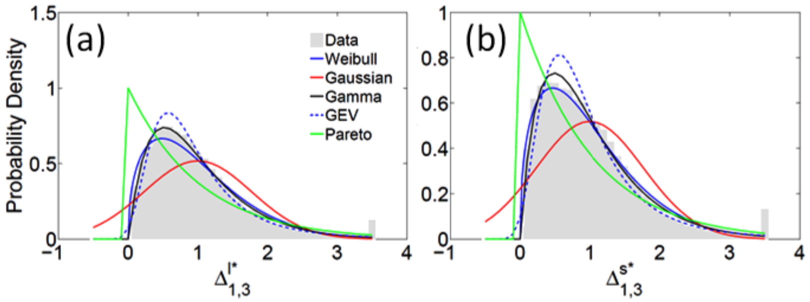

Figure 2.23: Probability distribution of the small dunes dimensionless descriptors: (a) lee amplitude, (b) stoss amplitude.

2.2.4 Discussion

2.2.4.1 Discrimination Method The new methodology proposed herein is based on the scaling definition of dunes and ripples, is applicable to laboratory and field measurements and overcomes the limitations of using a moving average and spectral analysis. The methodology allows the user to define the third level based on the potential scales of interest.

The present methodology has successfully discriminated larger bars and different scales of dunes. By analyzing synthetic signals, the procedure has also been shown to perform well in retrieving and quantifying the various scales of signal within a bed form series (up to the third-level wave) when at least one period of such a wave is present in the BFP, although it does impose some waviness where no single period is present. Therefore, there is an uncertainty in our results, although this is imposed by the data length rather than the methodology. Since the methodology solves for the $''s''$ parameter that minimizes this limitation, the retrieved larger scale signal is still more suitable than using a linear trend line (e.g. [249]) that may not be applicable for large rivers such as the Rio Paraná, where the mean river bed fluctuates over long distances.

Some researchers [249, 92] highlight that the definition of ripples as bed forms that have wavelengths less than 0.60 m is restrictive, although other researchers (e.g. [152]) have successfully used such a threshold. [65] suggest the use of a threshold bed form height to distinguish transient sand pile ups from stable bed forms that offer a resistance to flow. The estimates presented herein demonstrates that, even though the ripple definition is limited, when coupled with the capabilities of both robust spline filters and wavelet transforms such widely accepted discrimination criterion can retrieve relevant information for ripples and dunes for both their lee and stoss sides. Unfortunately, few studies have focused on the transitional areas between bed form states (e.g. see [33, 37]), even though they are critical to explain bed form scales.

The method proposed herein shows potential in retrieving the ripple signal with a reasonable level of accuracy, as demonstrated by the results of the synthetic signals analysis. Moreover, by using wavelet transforms, the distribution of the wavelengths of small dunes can also be estimated, and by using the robust spline filter the distribution of the amplitude of bed forms within the Río Paraná can be quantified and robustly assessed.

2.2.4.2 The Statistics of Bed Forms The bed morphology of the Río Paraná comprises bars (unit, point, complex bars), dunes (of various scales) and ripples with a three-dimensional morphology [198]. Bars have wavelengths from 325 m to >450 m, and generally larger bars are associated with larger dunes. A similar trend has been reported by [137], who studied the possible interaction between dunes and bars, and showed that the nonlinear coupling between relatively short (dunes) and long (bars) wavelength bed forms may cause the growth of bars.

In many instances in the present analysis, the dune signals show that higher trough-scour depths, relative to mean bed level, are succeeded by a higher upstream dune. Indeed the dunes within the present reach are markedly asymmetric, with the lee slope being nearly four times that of the stoss slope. As shown in Figure 2.5, the small dunes exhibit irregular three-dimensional features, which are similar to linguoid ripples that form under higher bed shear stresses, or have had longer development times, and represent the second stage of the transition from ripples to dunes [219].

If, similar to the signal to noise ratio, the scale-variance-ratio ($SVR_{i,j}$) is set as the ratio between the standard deviation of the hierarchy i and that of the hierarchy j, the present results show that $SVR_{1,2}$ (SVR between small dunes and medium-large dunes) is not correlated to the average water depth (see Figure 2.24a); the cross correlation between these signals is -3%. This implies that, similar to ripples, the height of the small dunes is not highly dependent on the water depth. This finding may be explained by some of the descriptors of the small dunes being governed by the local boundary layer thickness but being independent of the water depth [83]. On the contrary, $SVR_{2,3}$, the SVR between the medium-large dunes and bars (see Figure 2.24b), shows high dependence on the average water depth (the cross correlation between these signals is -87%), a relationship noted in the past work [218, 213, 66, 62, 67, 65]. Therefore, $SVR_{i,j}$ has the potential to become a robust frame in which to verify the accuracy of discrimination.

In the present study, the Anderson-Darling test was used to estimate the goodness of fit of the PDFs, which in past work has been assessed using a relative error [250] and the Kolmogorov-Smirnov test [252]. However, the Kolmogorov-Smirnov test presents two main limitations: [1] it tends to be more sensitive near the center of the distribution than at its tails, and, [2] perhaps a more serious limitation is that the distribution must be fully specified. Importantly, if the location, scale, and shape parameters are estimated from the data, then the critical region of the Kolmogorov-Smirnov test is no longer valid, and typically must be determined by simulation [188]. Use of the Anderson-Darling test, as proposed herein, overcomes these limitations and appears a more useful technique.

The PDFs of the dimensionless descriptors of bed form characteristics vary for different hierarchies. The PDFs that best describe the dune descriptors are the Gamma and Weibull functions, whereas the smaller dunes are best represented by the Gamma distribution. In all cases, the PDFs possess a positive skewness and leptokurtic distributions. Past studies [19, 250] did not analyze the PDFs of the stoss and lee descriptors, and highlighted that the PDFs are very sensitive to the preprocessing procedure. However, it is important to note that some of these studies found that both dune and ripple elevations are best described by the Gamma PDF [196, 153], whereas others found that the wavelengths, amplitudes and heights are best described by an exponential probability law [19].

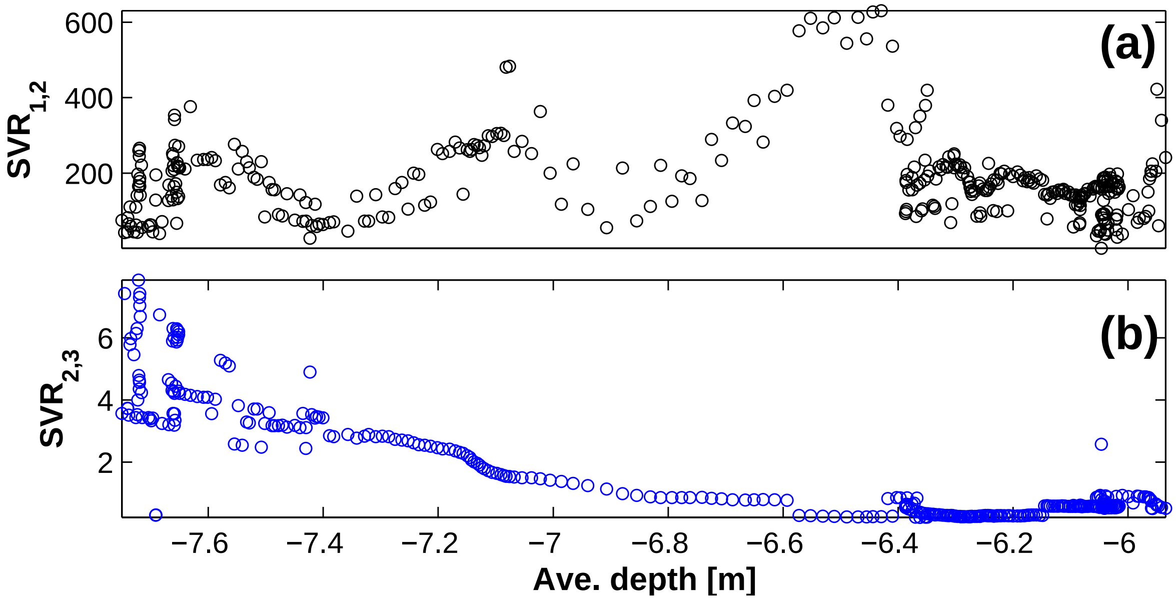

Figure 2.24: (a) $SVR_{1,2}$ (scale-variance-ratio between small and medium-large dunes), indicating no correlation with the averaged water depth; a characteristic similar to that of ripples. Conversely, (b) $SVR_{1,2}$ (scale-variance-ratio between medium-large dunes and bars), evidences strong dependence on the averaged water depth, as characteristic proper of the dunes.

2.2.5 Conclusions

The discrimination of different scales of bed forms is important in order to study the geometric variability, and quantify the influence of bed forms on the flow field and flow resistance. The present study has developed a methodology that combines the capabilities of continuous wavelet transforms and a robust spline filter to discriminate waves with different periodicities in bed form profiles, and has applied this methodology to 3-D bed form data from the Río Paraná, Argentina.

This method uses a symbolic representation of bed form descriptors (e.g. wavelength, amplitude and slope) for each hierarchy (e.g. small dunes, dunes, bars) and determines a delimitation of such descriptors that is in-line with past model, laboratory and field studies. The procedure has successfully retrieved the descriptors of the dunes scales for both the bed form stoss and lee sides.

The synthetic bed forms considered herein comprise wavelength scales ranges up to four orders of magnitude (e.g. bars of 200m down to ripples of 0.1m). For such a spectrum, the methodology proposed herein retrieved effectively information concerning the bars and dunes with a high accuracy for NR $>$ 25 and SNR closer to 5. For the case of ripples, the method retrieves a signal that is 75% correlated with the actual signal for NR $>$ 25. Likewise, the method retrieves around 70% of the wavelengths and 70% of the actual ripple amplitudes when the NR is higher than 25, but slightly decreases as the NR is increased. In cases where the frequency range is higher, the accuracy will tend to decrease as explained by the Heisenberg uncertainty principle. This methodology is shown to be robust when applied to bed form discrimination in the Río Paraná, Argentina, and allows separation of bar and various scales of dunes, which are superimposed on each other and on the larger barforms. One-dimensional wavelet transforms are not able to differentiate between a two-dimensional and a three-dimensional bed form feature. Since bed forms in natural channels are predominantly three-dimensional in planform, their scale-discrimination could be greatly assisted by the application of two-dimensional wavelet transforms and coupled with two-dimensional robust spline filters as proposed herein.

3.0 PLANFORM CHARACTERIZATION OF MEANDERING RIVERS BY USING WAVELET TRANSFORMS, PRINCIPAL COMPONENT ANALYSIS AND FRECHÉT DISTANCE

3.1 INTRODUCTION

Meandering patterns are ubiquitous in natural channels [205], and are also present in other phenomena such as rivulets running down plates [72, 49], water flowing over ice [76], ocean currents [164, 244], channels carved by molten lava on the Moon, Mars and Venus [124], subaqueous channels [112, 70, 12], barotropic jet stream paths [28], lightning paths [102, 16], among others.

The quantification of the variability of meandering river morphometrics is necessary for scientific and practical purposes. For scientific purposes it is key for studying: [1] the interrelationship between meanders and riparian vegetation [202, 50], [2] the influence of sinuosity on surface and groundwater interrelationship [52], [3] distinguishing natural from modeled channels [90, 108], [4] describing the implications of planform shapes into the morphodynamics of subaerial channels [2], among others. For practical purposes it is necessary for: [1] the design of civil infrastructure protection [247], [2] impact of reservoir on meandering planforms [230], [3] river restoration [177, 1], among others.

Past approaches towards meanders classification (e.g. [63, 47, 228, 222]) were developed with the aim of assessing stable and highly unstable planform patterns from maps, aerial photographs or visual inspection and without field data. Based on these criteria the [47] scheme was found to be the most appropriate [144]. According to the Brice classification scheme (see [144] for details on the planform characteristics of each class), meandering rivers have the following characteristics: [1] class A single phase with equiwidth and incised channels; [2] class B_1 single phase, equiwidth channel; [3] class B_2 single phase, wider at bends, no bars, [4] class C single phase, wider at bends with point bars; [5] class D single phase, wider at bends with point bars, chutes common; [6] class E single phase, irregular with variation; [7] class F two phase underfit, wandering; [8] class G_1. two phase, bimodal bankfull sinuosity equiwidth; and [9] G_2 two phase, bimodal bankfull sinuosity, wider at bends with point bars.

Past approaches to the quantification of meandering curvature variability have used and applied spectral analysis [235, 60, 88, 76, 106, 108, 170]. These spectral analyses were carried out by using the Fourier transforms which assumes that the data is stationary although river planform parameters possess trend, or non-stationarities. The latter is due to the continuous increase of the flow rate hence the increase of river size going downstream [60]. Fourier analyses have severe limitations for analyzing signals that include significant departures from stationarity [60]. And, a high number of Fourier coefficients is necessary to take into account structures which are visible on some intervals and invisible on others [143].

Past research in meandering morphometrics has followed two main approaches, namely, techniques in which a bend or loop as a whole is considered and those in which certain parameters of form or change are analyzed [106]. In the present contribution we follow the latter approach and use wavelet transforms to quantify meandering morphometrics. Wavelet Transforms were developed to overcome some of the limitations of the Fourier transforms and have been successfully applied to other quasi-periodic geophysical signals such as bedform profiles [158, 58, 98] and water waves [160, 171, 81, 82]. The present contribution extends Abad, 2009's ([7]) original application of the Wavelet transforms to the analysis of a planform curvature signal of meandering rivers.

3.2 METHODS

3.2.1 Data

3.2.1.1 Synthetic Meanders Sine generated meanders where proposed by Langbein and Leopold, 1966 [146]. They are based on the theory of minimum variance and are widely accepted as descriptive of self forming river planform geometry [264, 234, 174]. Sine generated meanders are defined from the angle ϕ_i (in radians) that the curve, at a given point, makes with the mean down valley direction [174], such that:

$$\phi_i = \omega_i \sin\left(\frac{2\pi s}{M_i}\right), \tag{3.1}$$

where ω represents the curve maximum angle of deflection, M is the bend length or arc-wavelength, s is the distance along the stream, and the sub index i denotes the number of bends being considered in the meander. Recent work performed by Mecklenburg and Jayakaran, 2012 [174] defined the amplitude, plan wavelength (L_m) and global curvature ($K = M/L_m$) of the sine generated meanders. They found the following approximated relationship between K and ω:

$$\omega = (12 + \frac{(-62208/K + ((-62208/K - 31104)^2 + 322486300)^{0.5} - 31104)^{1/3}}{3(2)^{1/3}} - \frac{144(2)^{1/3}}{(-62208/K + ((-62208/K - 31104)^2 + 322486300)^{0.5} - 31104)^{1/3}})^{1/2} \tag{3.2}$$

Thus, a set of synthetic meanders were generated. They comprise: [1] single-period meanders with $M_1 = 20$ and K_1 that ranges from 1.1 to 6; [2] two-period meanders with $M_1 = 4000$ and $M_2 = 70$, and $1.1 \geq K_1 \leq 3$ and $3.5 \geq K_2 \leq 5.5$; and [3] three-period meanders with $M_1 = 10,000$, $M_2 = 500$ and $M_3 = 5$ and $1.1 \geq K_1 \leq 2$ and $2.5 \geq K_2 \leq 3.5$ and $4 \geq K_3 \leq 5$. Subsequently, the meander curvature was estimated as $C = -d\phi_i/ds$ and the geometric coordinates of the meander at point $j + 1$ were estimated by the following relationship:

$$\begin{bmatrix} x^{j+1}(s) \\ y^{j+1}(s) \end{bmatrix} = \begin{bmatrix} x^j(s) + ds\cos(\phi_i(s)) \\ y^j(s) + ds\sin(\phi_i(s)) \end{bmatrix} \tag{3.3}$$

Figure 3.1 presents the details of the generated single-period meanders. Likewise, Figure 3.2a and 3.2b show instances of the two-period and three-period meanders, respectively.

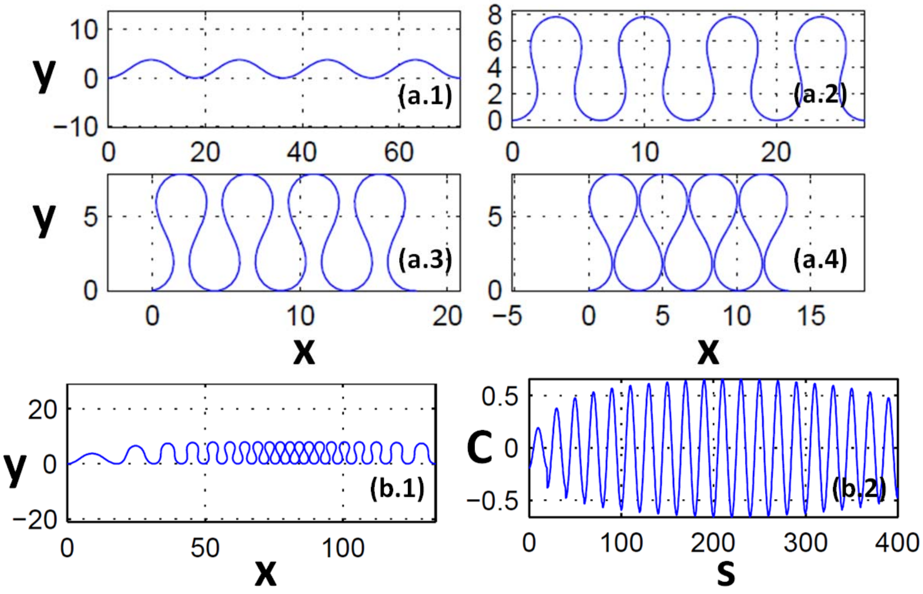

Figure 3.1: Generated single-period bends: (a.1, a.2, a.3 and a.4) geographical detail of the curves with $k = 1.1$, 3, 4.5 and 6, respectively; (b.1) single bends in juxtaposition; and (b.2) curvature signal of the bends presented in (b.1).

3.2.1.2 Natural Meanders Meander geometry is typically described in terms of the curvature (C) which is estimated based on the discretization of the channel centerline in equally-spaced points in local (curvilinear) or intrinsic coordinates [184, 108, 170, 154]. To convert geographical (e.g. Easting, Northing) coordinates into local coordinates (e.g. s, n), [154] proposed an algorithm that involves parametric description of the channel centerline using cubic splines, calculation of centerline normal vectors and curvature using results from differential geometry, and a local search to find in-channel data points and to compute their local coordinates. The inverse transformation finds the nearest vertices of a discretized

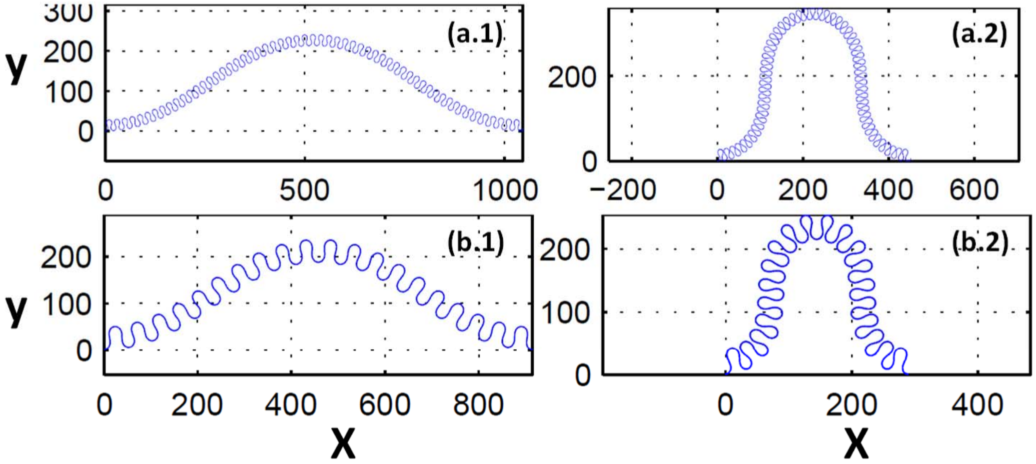

Figure 3.2: Synthetic meanders. Two-frequency instance for (a.1) $K_1 = 1.1$ and $K_2 = 3.5$, (a.2) $K_1 = 3$ and $K_2 = 5.5$. Likewise, three-frequency instance for (b.1) $K_1 = 1.1$, $K_2 = 2.5$ and $K_3 = 4$; and (b.2) $K_1 = 2$, $K_2 = 3.5$ and $K_3 = 5$

centerline and uses a finite difference approximation to the streamwise rates of change of the centerline's Cartesian coordinates to obtain the geographic equivalent of a point. Past research in meandering morphometrics has demonstrated that discretization of meanders at spacing of approximately one channel width is suitable to avoid noisy from curvature signals [106, 154, 182].

The data used herein is presented in Table 3.1 and includes rivers that range from class B_1 to class G_2 according to the Brice modified classification scheme [47] and are located in North and South America. Rivers class A, which represent the first degree on confinement [157], are not considered in this contribution because they are deeply inset into geological competent material such as bedrock, or they may be actively cutting through erodible material but having negligible lateral migration [144]. In all cases, except the Ucayali River (due to data scarcity), a minimum sample length of about 50-60 bends were used to avoid highly variable statistics, as suggested by [108]. Likewise, centerline data for the years 1990 and 2000 were obtained for Beaver, Carauari, Madre de Dios, Pearl, and El Tigre Rivers. For the Tahuamanu River, centerline data series for the years 1985, 1989, 1993, 1997, 2000, 2003, 2006, 2009 and 2011 were obtained. Likewise, for the Ucayali River, centerline data series for the years 1975, 1980, 1985, 1990, 1996, 2000, 2005, and 2010 were obtained.

Table 3.1: Study Rivers, $\bar{B}$ is the mean river width.

River	**Location**	**Mean Coordinates**	$\bar{B}$ **(m)**	**Brice Class**
Beaver	Canada	54° 16.511'N, 109° 43.572'W	54	F
Carauari	Brazil	4° 4.953'S, 66° 25.972'W	359	D
Las Piedras	Peru	112° 2.437'S, 69° 42.630'W	157	G2
Madidi	Bolivia	12° 50.044'S, 67° 32.122'W	135	D
Medicine	Canada	52° 12.357'N, 114° 15.121'W	43	B2
Pariamanu	Peru	12° 23.139'S, 69° 35.045'W	78	B1
Pascagoula	USA	30° 43.982'N, 88° 39.599'W	158	C
Pearl	USA	30° 47.552'S, 89° 49.229'W	89	C
Red Deer	Canada	51° 1.500'N, 111° 57.116'W	165	F
Steen	Canada	59° 27.246'N, 117° 11.767'W	122	F
Tahuamanu East	Bolivia	11° 25.619'S, 69° 4.187'W	153	G2
Tahuamanu West	Peru	11° 23.032'S, 69° 36.952'W	155	G1
Tigre East	Peru	4° 1.189'S, 74° 19.362'W	315	B2
Tigre West	Peru	3° 21.611'S, 74° 57.047'W	200	E
Ucayali	Peru	5° 19.587'S, 74° 21.968'W	1123	C (US), D(DS)
Yapacani	Bolivia	16° 24.356'S, 64° 8.694'W	133	G2

3.2.2 Continuous Wavelet Transforms

Wavelets can be generally classified as discrete (DWT) and continuous (CWT). The former is the analogue of the discrete Fourier transform (applicable to inputs that are often created by sampling a continuous function) and is more appropriate for data compression and signal reconstruction, the latter is analogous to the Fourier transform and is usually applied to the analysis and detections of signal singularities and patterns [20].

The unidimensional wavelet transform (WT) of a signal $x(t) \in L_2$ is obtained by the convolution of the signal and the wavelet function (WF) or mother wavelet $\psi(t)$ as expressed by Equation (4.1), where a is the scale parameter, b is the location parameter and $\bar{\psi}_{a,b}(t)$ is the complex conjugate of $\psi_{a,b}(t)$, as mathematically represented by Equation (4.2). According to the Parseval's theorem [14] the same wavelet transform can be expressed by Equation 4.3.

$$T(a,b) = \int_{-\infty}^{\infty} x(t)\bar{\psi}_{a,b}(t)\,dt, \text{ for } a > 0, \tag{3.4}$$

$$\psi_{a,b}(t) = \frac{1}{\sqrt{a}}\psi(\frac{t-b}{a}) \tag{3.5}$$

$$T(a,b) = \frac{1}{2\pi}\int_{-\infty}^{\infty} \hat{x}(f)\bar{\hat{\psi}}_{a,b}(f)\,df \tag{3.6}$$

where $\hat{x}(f)$ and $\hat{\psi}_{a,b}(f)$ are the Fourier transforms of $x(f)$ and $\psi_{a,b}(f)$, respectively. The wavelet power spectrum is defined as $|T(a,b)|^2$; and in terms of computational cost, it is less expensive to quantify it from Equation (4.3) [243].

The most commonly-used continuous WFs are the Morlet and the $n-th$ derivatives of the Gaussian, being the Ricker, or so-called Mexican hat wavelet, the second derivative. According to the uncertainty in Heisenbergs principle, there is a lower limit to the product of frequency and time resolution; in such a way that as time resolution is improved, frequency resolution degrades and vice versa [14]. The Morlet function provides lower area of the Heisenberg cell than the derivatives of the Gaussian wavelet functions and retrieves wavelengths of higher frequencies. This efficiency of the Morlet wavelet function is particularly important to retrieve higher frequencies of bedforms [98] and river curvature. Therefore, the continuous wavelet analysis is performed by using the Morlet wavelet function and a modified version of the wavelet software provided by [243].

3.2.3 The Principal Component Analysis - Discrete Wavelet Filter

Aminghafari et. al, 2006 ([17]) combined the ability of the principal component analysis (PCA) to decorrelate the variables by extracting a linear relationship with that of the DWT to extract deterministic features and approximately decorrelate autocorrelated measurements [27, 17, 111, 180].

The DWT should meet the following requirements: [1] having compact support, it means having a finite number, namely $N_k - 1$, of scaling coefficients (c_k) and being smooth to some degree. [2] Having a vanishing moment. The Daubechies wavelets have $N_k/2$ vanishing moments which implies that they can suppress parts of the signal which are polynomial up to the degree $N_k/2 - 1$ [14]. [3] In order to minimize the number of high amplitude coefficients, the support size should be reduced. Daubechies wavelets are optimal in the sense that they have a minimum size support for a given number of vanishing moments [169]. Therefore, the selection of the appropriate wavelet from the Daubechies wavelets family is highly dependent on the physical and mathematical properties of the signal being analyzed.

PCA is a non parametric method of extracting information in high dimension and reducing the number of descriptive variables from a data set matrix X of dimensions n x p (the number of measurements and variables, respectively) by projecting it onto a lower dimension space P of dimension $q \leq min(n, p)$, where the new variables defining this space are called the principal components [180]. This operation is carried out assuming that: [1] there is a linear relationship between the data components; [2] the principal components with higher associated variances represent the principal components, while those with lower variances represent noise; and [3] the principal components are orthogonal, otherwise the PCA is not soluble [119].

The Wavelet Principal Component Analysis (WPCA) scheme encompass the following steps [17]: [1] perform the wavelet transform at level J of each column of the matrix X; [2] Define $\hat{\Sigma}_\epsilon$, the estimator of the covariance matrix, as $\hat{\Sigma}_\epsilon = MCD(D_1)$ and then compute V such that $\hat{\Sigma}_\epsilon = V \Lambda V^T$; where $\Lambda = diag(\lambda_i, 1 \leq j \leq J)$ and $MCD(D_1)$ is the Minimum Covariance Determinant [224] applied to the D_1 the matrix of the details at level 1. Apply to each detail after change of basis (namely $D_jV, 1 \leq j \leq J$), the p univariate thresholding strategies using the threshold $t_i = \sqrt{2\lambda_i \log n}$ for the $i - th$ column of D_jV; [3] Perform the PCA of the matrix A_j and select the appropriate number p_{J+1} of useful principal components; [4] Reconstruct the denoised matrix $\hat{X}$ from the simplified detail and approximation matrices, by inverting the wavelet transform; and [5] perform a final PCA of the matrix $\hat{X}$ obtained at step 4 and select the $\hat{p}$ principal components. It is important to remark that for steps 3 and 5 the components associated to eigenvalues greater than 5% of the sum of all the eigenvalues are retained [17]. Herein, a methodology that combines of WT and PCA is applied to different types of meandering rivers based on Brice classification scheme.

3.2.4 The Fréchet Distance

The Fréchet distance measures the closeness of two time series if stretching and compression in time is allowed, but temporal succession is to be preserved [79]. The algorithm to estimate the Fréchet distance uses a reparameterization continuous function $f : [0, 1] \rightarrow [0, 1]$ which is orientation-preserving, such that $f(0) = 0$ and $f(1) = 1$. Thus, given two reparameterization functions f and g for two curves π and σ in $\Re^d$, respectively, their width is defined by Eq. 3.7.

$$width_{f,g}(\pi, \sigma) = \max_{s \in [0,1]} \parallel \pi(f(s)) - \sigma(g(s)) \parallel \tag{3.7}$$

This can be interpreted as the maximum length of a leash one needs to walk a dog, where the dog walks monotonically along π according to f, while the handler walks monotonically along σ according to g. In this analogy, the Fréchet distance is the shortest possible leash admitting such a walk [77]. Recent application of the Fréchet distance to the analysis of geophysical signals encompasses the similarity or dissimilarity of hydrographs [79] and salinity stratification [161].

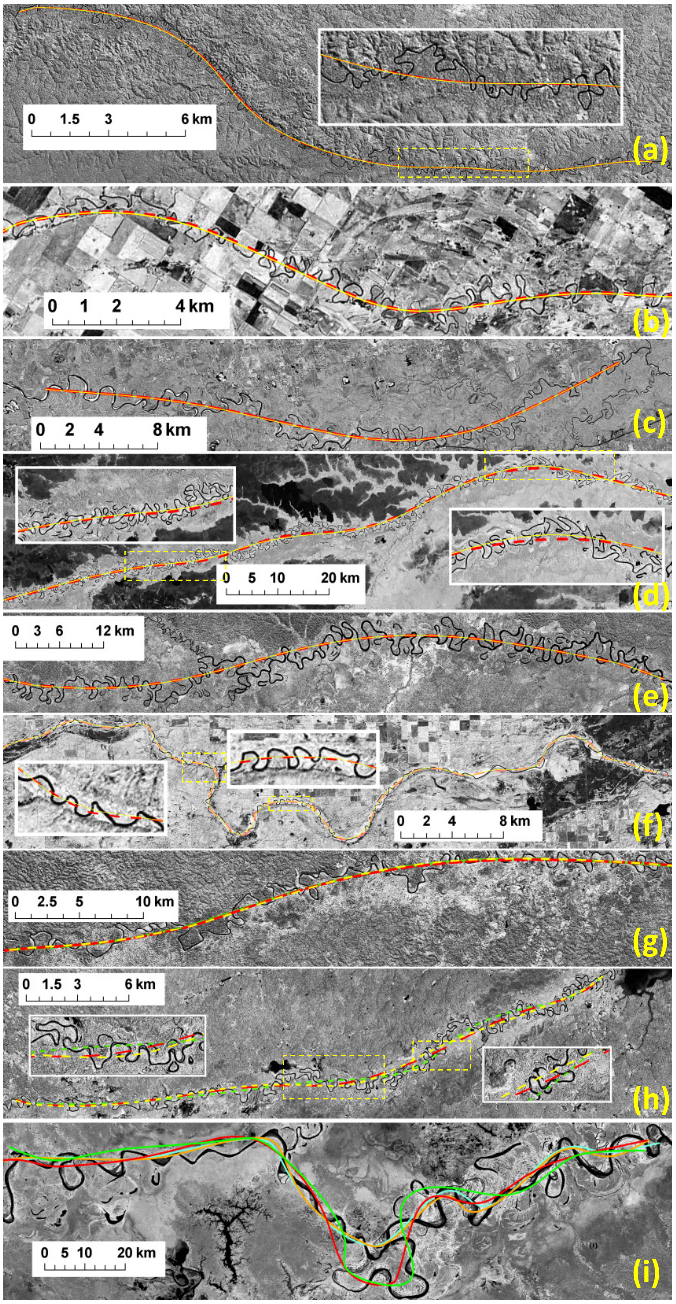

Figure 3.3: Mean centers for rivers: (a) Pariamanu (continuous yellow line: MC at 1990, red dotted line: MC at 2000); (b) Medicine River B_2; (c) Pearl; (d) Madidi; (e) Tigre-West; (f) Beaver; (g) Tahuamanu-West(yellow dots: MC at 1985, red dots: MC at 2000, and green dots: MC at 2011); (h) Tahuamanu-East; and (i) Ucayali (green, red, orange and cyan lines are the MC at 1975, 1990, 2000, and 2010 respectively). In all figures, the MCs are overlapped on 2000 LandSat images EarthSat MrSID Coverage.

3.3 RESULTS AND DISCUSSION

3.3.1 Wavelet Analysis of the Synthetic Data

The analysis performed on the synthetic data reveals that the continuous wavelet transforms (not shown here) can only retrieve the higher frequency of the synthetic data, although it identifies the other periods. This result was expected since the quantification of the curvature implies taking the derivative of the deflection angle ϕ_i with respect to the local coordinate s. This operation detrends the deflection angle; and thus, the lower frequencies of the curvature are attenuated. Therefore, the meander planimetry spectrum cannot be fully described by analyzing the curvature signal. Complementary estimation of the mean center is necessary to retrieve information of the lower frequencies. This fact is discussed in detail in the next section.

3.3.2 The Mean Center: MC

We define the mean center (MC) as the midterm lifespan (e.g. 10 years or more) coherent wave of the meanders centerline. In order to apply the wavelet-PCA (WPCA) method on the centerline data, the centerline coordinates are treated as complex numbers in which the real and imaginary parts are represented by the Easting and Northing coordinates respectively. Similar consideration were applied in the past to study wind fields pattern recognition [256, 135]. We applied the WPCA filter on meandering rivers discretized at different sampling rates that ranges from $0.5\bar{B}$ to $2\bar{B}$, where $\bar{B}$ the mean river width. Our estimates show that the Daubechies-10 wavelet best represents the aforementioned definition and the results exhibit high sensitivity to the centerline's sampling rate. The MC get stable at sampling rates equal to $\bar{B}$ and lays inside the rivers geological walls and floodplains. Since the Daubechies-10 wavelet has 5 vanishing moments, the MC represent the river centerline wave having the polynomial up to the fourth degree suppressed.

The WPCA at $J = 1$ represents the river centerline itself. Lower values of J are necessary to obtain the MC for rivers that show low variability with respect to the MC (e.g. confined meandering rivers). Confined meanders are those that are unable to fully develop the planform geometry of freely meanders because their lateral migration is constrained by the walls of the relatively narrow valley through which they flow. Most of them have very sharp bends at the point of impingement on the valley walls [185]. Our results demonstrate that the WPCA at level $J = 5$ performs well for confined meanders (class F based on Brice modified classification scheme [47]) and for freely meanders (class B_1, B_2, C, D, D, G_1 and G_2) WPCA at levels of $J = 7 - 8$ provides good results. It is important to note that in confined meandering rivers such as the Beaver River, the actual valley center could be closer to the MC, while in the case of freely meandering rivers (e.g. Ucayali River, Tahuamanu River, etc.), it could differ from the valley center. In practice, river study reaches are comprised by different Brice class sub-reaches; therefore, in order to define the appropriate WPCA level J the MC should be compared with the available geological data. Our results with the analysis of the composite cases for Tahuamanu West and East and Tigre West and East show that a good approximation is achieved by $J = 6 - 8$.

The present study uses satellite image data which has been available for around 35 years, and rivers large enough to be visible on satellite images (as those included in the present contribution). These rivers may evolve too slowly to reveal all their dynamical properties over this time span [238]. This fact represents a limitation of fully quantification of the upper margin of the MC lifespan. Figure 3.2.4 shows some of the results of the MC. Figures 3.2.4a-f show that the MC for river class B_1 to F slightly vary for the period 1990-2000 and we argue that such condition is also valid for longer periods. For the case of Tahuamanu-West River (Figure 3.2.4g), which is class G_1, the MC slightly varies for the period 1985-2011 (27 years) and it could keep on remaining the same for longer periods of time. On the other hand, the Tahuamanu-East River (Figure 3.2.4h), which is class G_2, the MC; slightly varies at each 10 years. The Ucayali River (Figure 3.2.4i), which is a composite river (class C at the upstream stretch and class D at the downstream stretch), present subtly changes in its MC for the period 1975-1996 (21 years), and for the period 2000-2010 (10 years). For the period 1996 to 2000, the MC changes dramatically due to a reported man-made cutoff occurrence. This anthropogenic distortion consisted of digging out small-width channels alongside a path that crossed the neck cutoff to facilitate navigation and transportation to the local major cities. Similarly, Coomes et. al., 2009 [69] described that the small-scale human action like enhancing meander cutoff resulted in significant ecological and economic consequences. They mentioned that the 1998 Masisea cutoff (orange line in Figure 3.2.4i) in the Ucayali River produced the most dramatic planform change in the River in the last 200 years.

As shown above, the WPCA could be used to obtain a reliable approximation of the true valley centerline, thus the MC centerline serves as input to long-term morphodynamic models such as RVR Meander (www.rvrmeander.org) [1, 182] for predicting meander evolution of specific rivers by considering the valley planform configuration.

3.3.3 The Interrelationship Between the Mean Center and Centerline Curvatures

The interrelationship between the MC and centerline curvatures is analyzed. To this end, the normalized curvature signals from both entities were obtained by multiplying the curvature by river width ($\bar{B}$) and their local abscissas were normalized with their respective total length. Thus obtaining $C^* - S^*$ datasets. Subsequently, both signals were evenly discretized and thus, time series were obtained. In all the instances in which the MC curvature present marked peaks the local cross correlation was quantified using the wavelet coherence. This methodology was proposed by [95] and has been used in the analysis of the periodicities of solar activity [248], morpohological patterns in sandbar systems [226], paleoclimatic records [125], sand transport in aeolian environments [24], among others. The analysis reveals that even though the global correlation between the MC and centerline normalized curvatures is weak (below 0.3 in most of the cases), a strong local correlation exists between them. Figures 3.4a-f show that, in general, peaks in the centerline are strongly correlated with peaks in the MC for the case of freely meanders. For the case of confined meanders, there is also a strong correlation between global maxima curvature in the MC and lower curvature in the centerline curvature. A visual analysis also confirms this fact.

Likewise, some instances show that cutoffs are produced in the vicinity of peaks in the MC local curvature. This is explained by the fact that each cutoff has a tendency to trigger other cutoffs in its vicinity by causing accelerated local change, and therefore, generating a cluster of cutoffs in space and time [237, 5].

Figures 3.4a-f also show that there are either positive or negative lags in the development of peaks in the centerline curvature triggered by peaks in the MC curvature. Is is important to note that in order to have reliable wavelet coherence estimates in the higher frequencies, the data should not be highly non-normal [95]. An statistical analysis of the normalized centerline curvature signals reveals that they can be approximated to a bivariate normal distribution after performing the Johnson transformation with a 95% of confidence interval. The Johnson transformation consist of three types of functions to transform a given variable Y: [1] the Log-normal system $g_L(Y) = \ln(Y)$, [2] the bounded system $g_B(Y) = \ln[1/(1-Y)$, and [3] the unbounded system $g_U(Y) = \ln[Y^2 + \sqrt{Y^2+1}]$ [57]. In all the cases, the unbounded system best describes the meanders curvature. Figure 3.5 shows three examples of this statement no mater the class of river we are dealing with. As it can be inferred from the aforementioned relationships, the data needs to be positive. In order to have positive normalized curvature data all the data set were translated to an origin equal to a value of 9, thus $\hat{C}$ was obtained.

Past researchers [90, 108] have used straight lines to perform the classification of river bends and quantify the half-meander statistics. By using the appropriate wavelet level (e.g. $J = 5-8$), the MC also be used as a robust framework to perform such analysis. The above correlation between the MC and the river centerline could be used as a surrogate for floodplain modulation (e.g. geology, vegetation, soil distribution) into the development of complex meander shapes.

3.3.4 The Planform Amplitudes

The planform amplitudes are defined as the orthogonal distance from the river centerline to the MC. They are normalized with the mean river width and are denoted as Δ^* in this

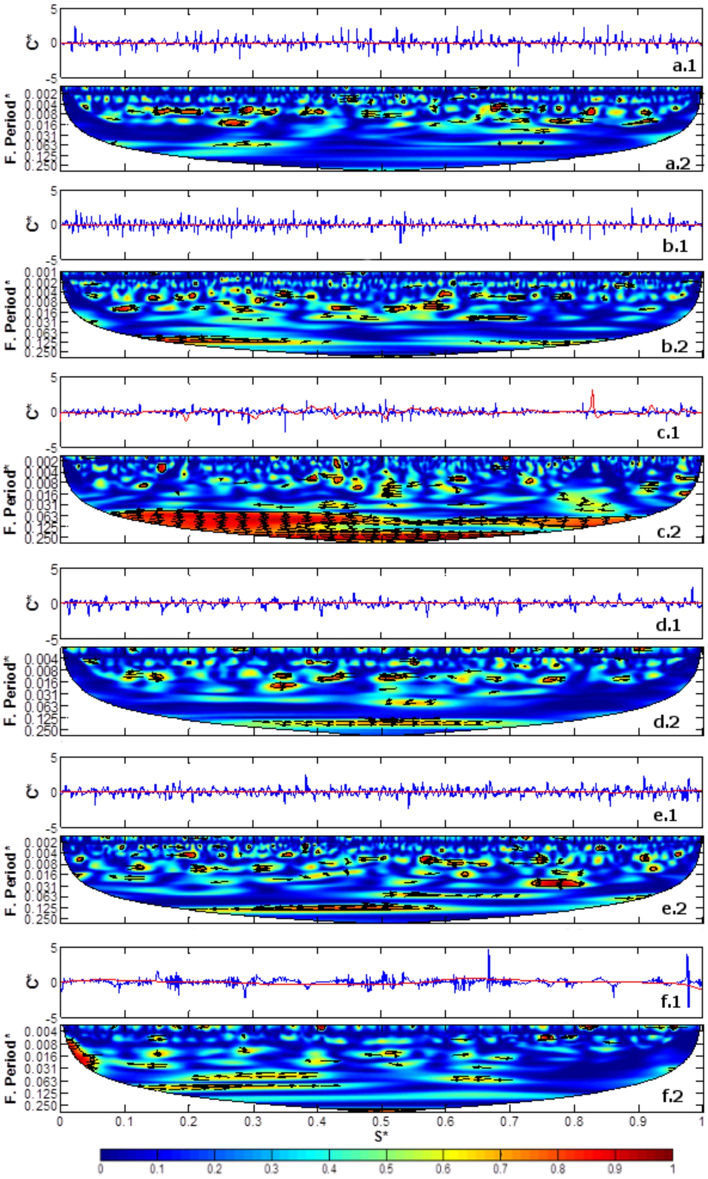

Figure 3.4: At the top of each sub-figure the centerline (blue line) and MC curvatures (red line, vertically scaled 10 times for the sake of visibility) are shown; at the bottom, the wavelet coherence between these signals is shown for the rivers: (a) Pariamanu, (b) Madidi, (c) Beaver, (d) Tahuamanu-West, (e) Tahuamanu-East, and (f) Ucayaly. In all cases, the peaks in centerline curvature are strongly correlated with peaks in the MC curvature for freely meanders; for the case of confined meanders (e.g. Beaver River) higher peaks in the MC curvature are also correlated with lower centerline curvatures. The contours are showing the degree of correlation.

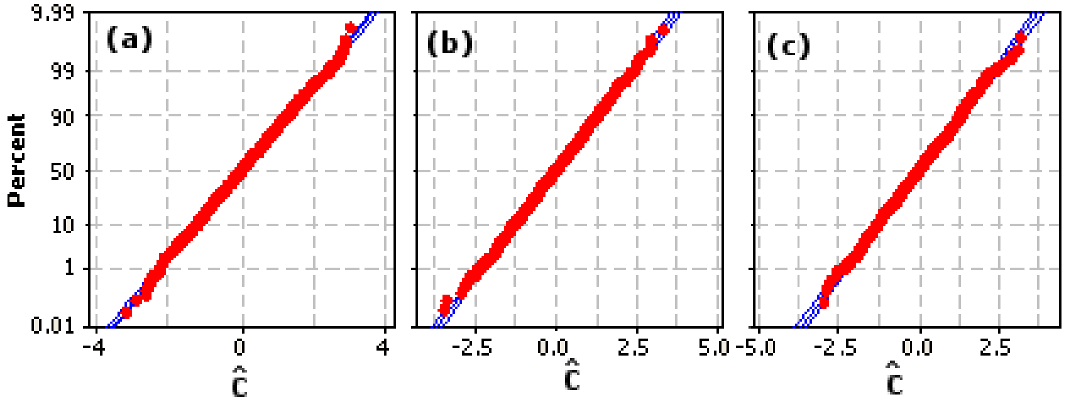

Figure 3.5: Normal distribution after the Johnson transform of the centerline curvature the Pariamanu River at 2000 (left), Beaver River at 2000 (center) and Ucayali at 2000 (right). In all cases, the abscissa represents the normalized amplitudes. The $\hat{C}$ data was obtained by translating the C^* data to an origin located at 9.

contribution (Figure 3.6). Typically, the planform amplitudes for freely meanders are in the interval $\sim[8-20]$. The higher values correspond to rivers class B_1-F (Figure 3.6a-e) whereas lower values correspond to river class G_1 (Figure 3.6g). It is important to note that $\Delta^* > 20$ were estimated for meanders that are located in tidal environments such as the Pearl or Pascagoula river (not shown here but included in the data set). This fact was expected because tidal meanders, as they evolve, exhibit strongly non stationary morphometric descriptors (e.g. wavelength, radii of curvature and width) and remarkably different from those observed in meandering rivers [170]. The normalized planform amplitudes in confined rivers vary in the interval $[2-5]$, where the large values correspond to higher values of $\Delta|S_{WT}|$ such as the Beaver River (Figure 3.6f).

An statistical analysis of the amplitudes reveals that it is strongly normal distributed. This was expected because the WPCA discriminated the coherent wave from transient wave that coexist in the centerlines signals. This fact also indicates that this distribution can be used in Monte Carlo simulations for midterm horizons.

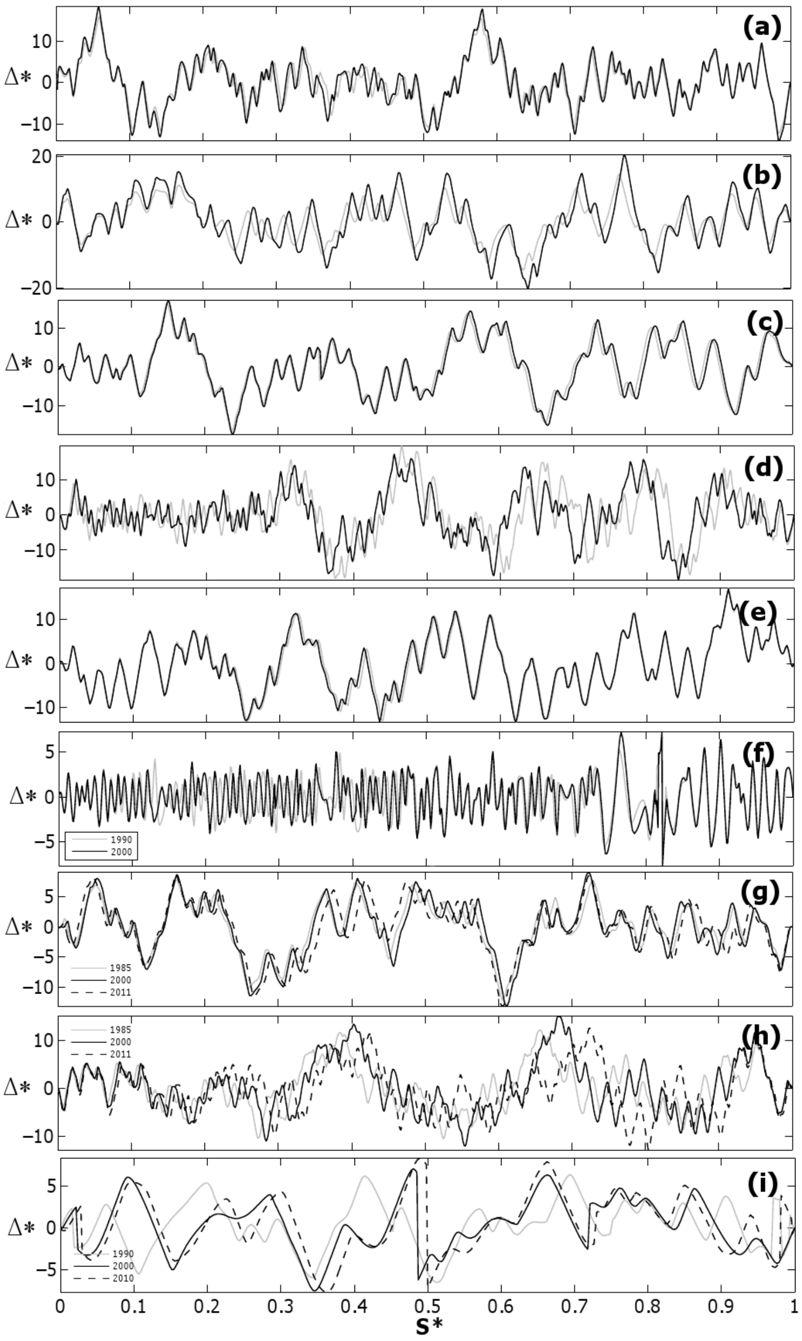

Figure 3.6: Normalized historical planform amplitudes for River: (a) Pariamanu, (b) Medicine, (c) Pearl, (d) Madidi, (e) Tigre-West, (f) Beaver, (g) Tahuamanu-West, (h) Tahuamanu-East, and (i) Ucayali.

3.3.5 The Meanders Wavelet Entropy and the Normalized Fréchet Distance

The wavelet entropy is a nonlinear chaotic measure that is used herein to quantify the degree of either order or disorder of the meanders curvature signals. It is used herein to retrieve useful information about the underlying dynamical process associated to each meandering class. An ordered process is defined as a periodic mono-frequency signal (a signal with a narrow band spectrum) having a wavelet representation resolved in one unique wavelet resolution level because all relative wavelet energies are negligible, except the wavelet resolution level which includes the representative signal frequency [215]. In meandering rivers, such kind of signals would be represented by the curvature of ordered meanders that shift downstream with a constant speed while maintaining a coherent shape [197]. On the antithesis of this condition, chaotic meanders, characterized by alternating phases of lateral migration that acts to increase sinuosity and sporadic shortening by cutoff events and subsequently oxbow lakes formation, also exist. In the ordered state cutoffs act to destroy order, whereas in the chaotic state cutoffs create order[237].

We use the Shannon wavelet entropy (S_{WT}), which is defined by Eq. 3.8 [23], where S is the signal being analyzed and (S_i) are wavelet coefficients of S in an orthonormal basis. Subsequently, the absolute value of the annual entropy gradient ($\Delta|S_{WT}|$) is obtained.

$$S_{WT} = -\sum_i S_i^2 \log(S_i^2) \tag{3.8}$$

We define δ_F^* as the Fréchet distance between the meander centerline and its MC normalized with the absolute value of the maximum planform amplitude; thus, the meander valley control can be dimensionless quantified. Figure 3.7 shows the results obtained from the 52 realizations considered in the present study. This metric identifies a threshold of $\delta_F^* \sim 650$ to discriminate freely from confined rivers. By means of it, scales of the second and third degree of confinement identified by [157] can also be quantified. Likewise, the $\Delta|S_{WT}|$ metric suggests that there are 4 categories of rivers laying in the intervals (e.g. $[10^{-1} - 10^0]$, $[10^0 - 10^1]$, etc.). Therefore, these objective metrics have the potential to become meandering classifiers, although more data and analysis is needed in this regard. We argue that based on these classifiers boundaries of subresonant and superresonant morphodynamic regimes proposed by [229] and [148] can also be identified.

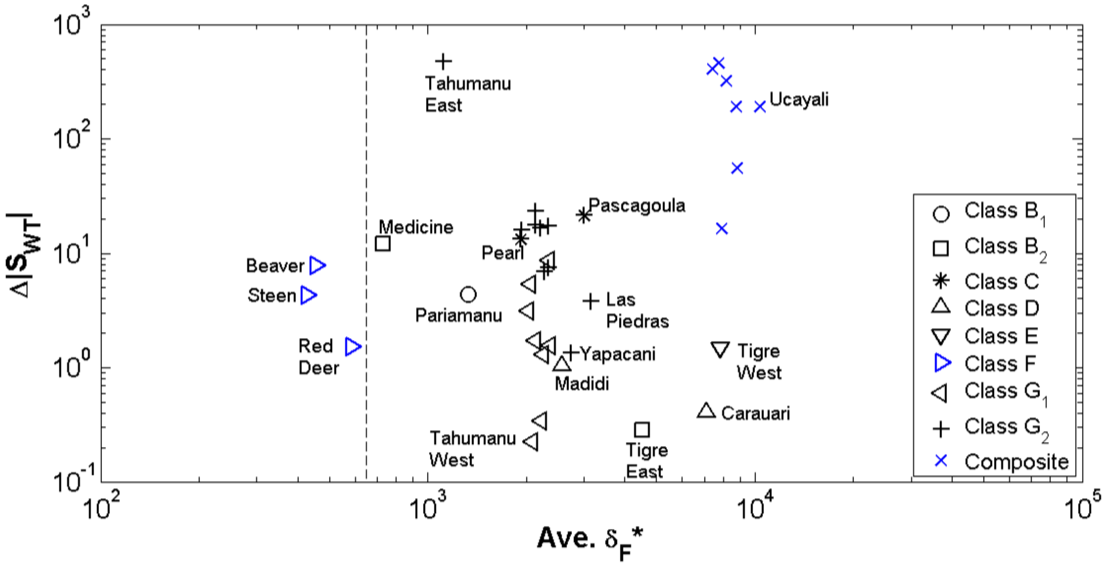

Figure 3.7: Classification of meandering rivers based on the normalized Fréchet distance (δ_F^*) and the annual gradient of the Shannon wavelet entropy ($\Delta|S_{WT}|$). The divide that discriminates confined from free meanders (black dotted line) is located at $\delta_F^* \sim 650$.

3.3.6 Wavelet Analysis of the Dimensionless Planform Amplitudes and Curvature

The wavelet analysis of the meanders dimensionless curvature-local abscissa ($C^* - S^*$, where $C^* = C\bar{B}$ and $S^* = S/\bar{B}$) was also performed using the Morlet wavelet function. Such analysis concentrated in quantifying the arc wavelength, namely, the wavelength along the river centerline.

Figure 3.8 shows the capability of the wavelet transforms to retrieve information from the arc wavelength (e.g. dominant periods and spatial distribution of the frequencies) along the entire stretch of the Pariamanu River for the year 1990. The dimensionless curvature (Figure 3.8a) varies in the interval $\sim[-2.5 to 2.5]$ and shows to be non-stationary, namely, having a non-constant mean value along the study stretch. Therefore, the Fourier analysis would be limited in fully describing the spectrum of frequencies of this signal; moreover, it would

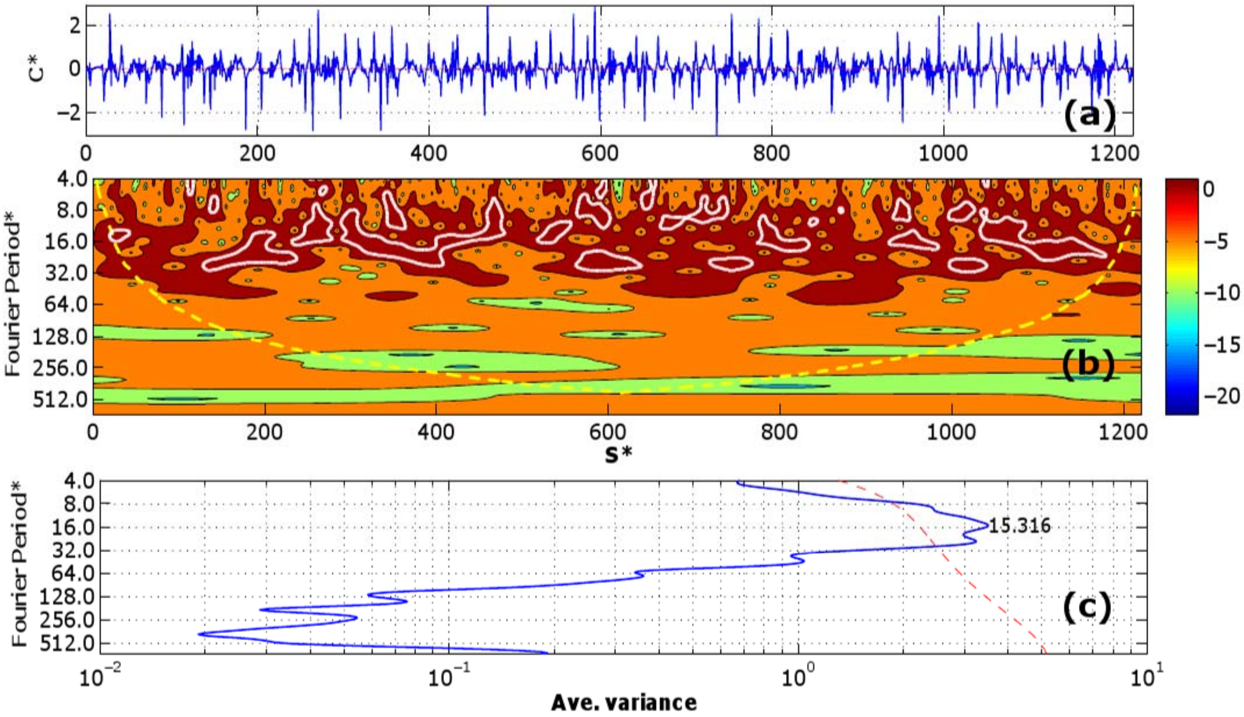

Figure 3.8: Wavelet output for Pariamanu River for the year 1990. (a) The $C^* - S^*$ signal (where $C^* = C\bar{B}$ and $S^* = S/\bar{B}$) ; (b) wavelet spectrum of arc wavelength at 95% of confidence (the dotted line represents the cone of influence border); and (c) the global wavelet spectrum (the dotted line represents the 95% interval of confidence limit). Based on this analysis, the dominant wavelenghts for the Pariamanu River (class B_1) are respectively $\sim 2\bar{B}$ and $\sim 15\bar{B}$.

not provide information about the spatial distribution of such spectrum. Conversely, wavelet power spectrum (Figure 3.8b) shows that two marked frequency intervals are developed along the stretch (bold white contours). They represent peaks in the frequency variance (Figure 3.8c) at 95% of confidence; being the high and low coherent arc-wavelengths respectively ∼2 and ∼15 times of the river mean width (∼78m). It is important to mention that the wavelet software provided by [243] also estimates the confidence intervals of the wavelet analysis such as the cone of influence (yellow dotted in Figure 3.8b) that bounds the edge effect of the wavelet transforms, and the coherent arc-wavelength peaks at 95% of confidence, represented by the peaks located over the 95%-divide (red dotted line in Figure 3.8c).

Figure 3.9a-h presents the C^* wavelet spectra in which the contours below the 95% of confidence have been filtered. They show that typically the lower coherent period is weaker than the higher one and that regardless the meander class, it is $\sim 3\bar{B}$. In the present contribution, we have considered stretches that range from 50km to 440 km, therefore, this parameter exhibit not marked sensitivity to the reach length when an appropriate number of bends (e.g. 50-60) are considered in the analysis. The higher coherent period ranges from $\sim 20\bar{B}$ to $\sim 25\bar{B}$. In such interval, the lower range corresponds to confined rivers. Intermittent middle periods are developed specially for class G_2 and composite rivers such as the Ucayali River.

A comparison of the river curvature historical wavelet spectrum provides information about the temporal changes in the meanders frequencies distribution. The occurrence of higher frequencies are related to planform dynamics such as horizontal and vertical heterogeneities that are splitting elongated meanders and producing smaller meanders [181]. Figure 3.10 presents the historical distribution of the frequencies of the contours at 95% of confidence. A threshold that represents around the 25% of the whole frequency spectrum is set to defined the lower and higher frequencies (black dotted lines in Figure 3.10a-c). Thus, for the period 1990-2000, the Yapacani River (class G_2, Figure 3.10a) shows a marked decrement (∼50%) in the relative area of the higher frequencies at the expense of an increment in the relative area of the lower frequencies (∼50%), resembling an amalgamation process. For the case of the Steen River (class F with lower normalized Fréchet distance, Figure

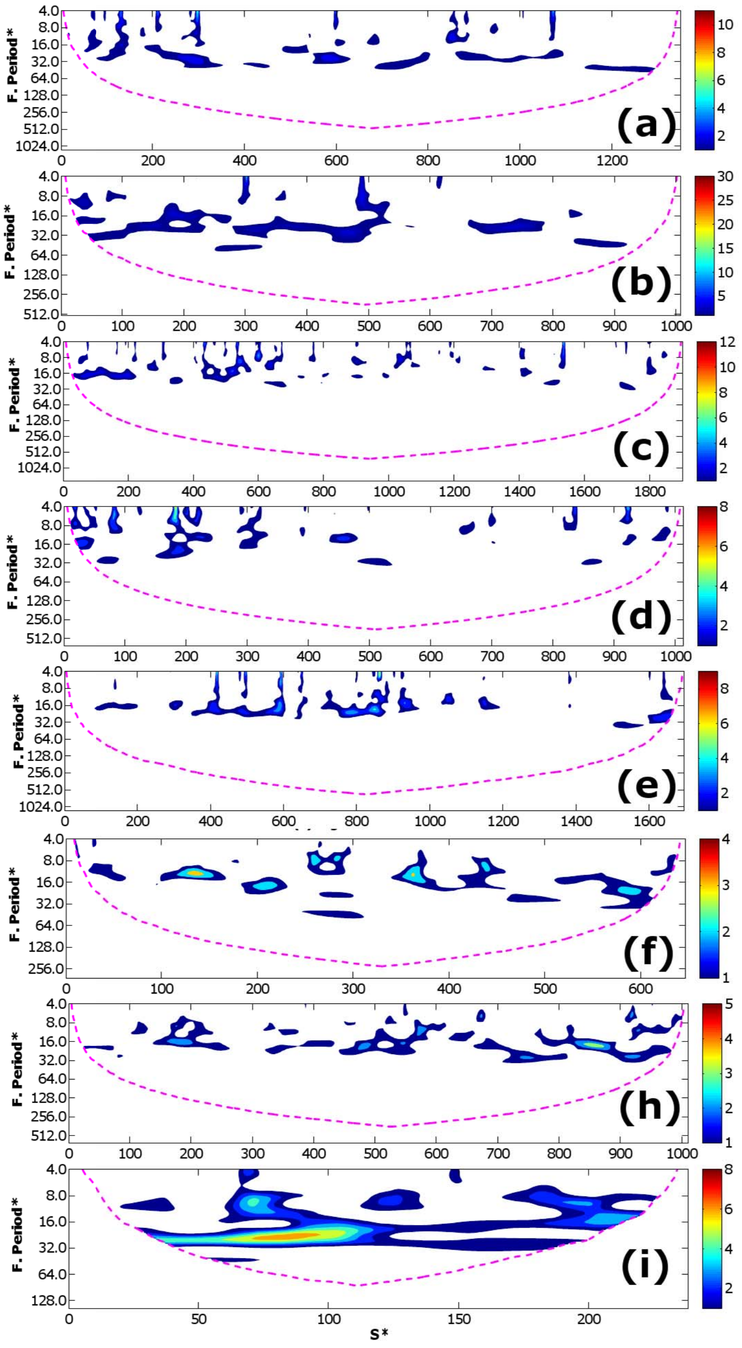

Figure 3.9: Wavelet spectrum output for the normalized curvature of Rivers (a) Medicine, (b) Pearl, (c) Madidi, (d) Tigre-West, (e) Beaver, (f) Tahuamanu-West, (g) Tahuamanu-East, and (h) Ucayali. The spectra show only the contours at 95% of confidence and the cone of influence (dotted magenta lines). Regardless of the river class, the lower coherent period is typically $\sim 3\bar{B}$ and the higher coherent period varies $\sim 20\bar{B} - 25\bar{B}$. In all cases the represented year is 2000.

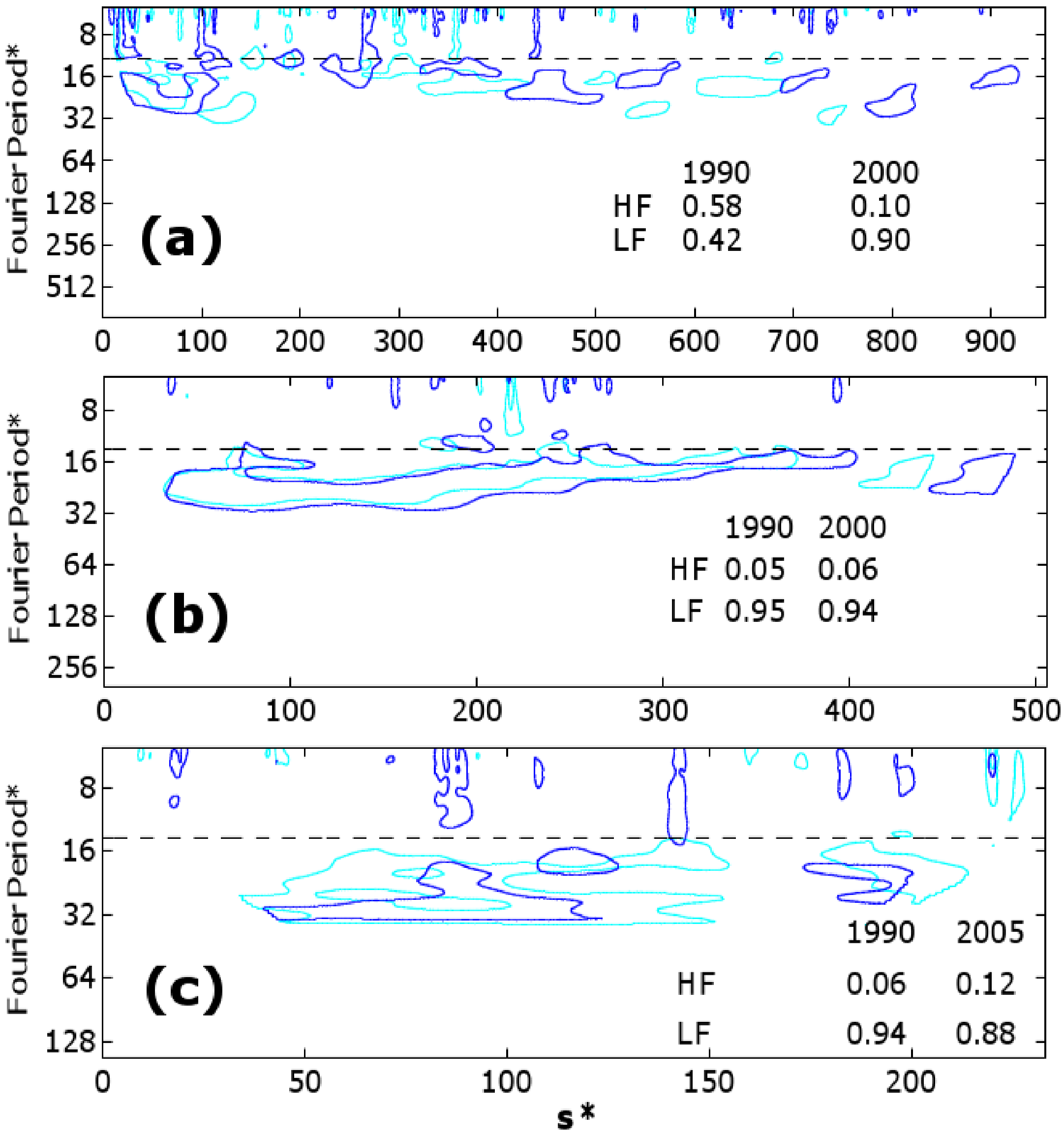

Figure 3.10: Historical spatial distribution of the arc wavelength frequencies for: (a) Yapacani River (class G_2) for the period 1990-2000, (b) Steen River, class F (1990-2000), and (c) Ucayali River, composite, (1990-2005). In all cases, blue contours represent earlier years than the cyan contours. The quantities in the figures represent the density of the higher (HF) and lower (LF) frequencies for a given year.

3.10b) shows a slight change in the area of the lower and higher frequencies. On the other hand, for the period 1990-2005, the Ucayali River (Figure 3.10c) presents an increase of ∼200% in the area of the higher frequencies at the expense of a ∼10% decrement in the lower frequencies, resembling a markedly splitting process of the lower frequencies to produce higher frequencies (the bend planform shape is becoming more complex). Both the splitting and the amalgamation processes are also observed in river bed form configurations [98]. The capability of the continuous wavelet transforms to identify and quantify changes in the frequency spectrum could also be compared with those of simulated meanders to assess the effectiveness of the model to replicate the observed processes. Based on this analysis, it is evident that the balance in frequency of meanders is a notorious process at which planform shapes are constantly adapted along the river evolution, and it could show its potential when comparing paleochannels to modern channels for understanding climatic effects into morphodyamics of meandering rivers.

The continuous wavelet analysis performed on the planform amplitudes (Figure 3.11) reveals that this parameter has a quasi periodic behavior ranging from markedly polymodal with a peak period of $\sim 40\bar{B} - 120\bar{B}$ in the case of freely meanders (Figure 3.11a-d and Figure 3.11f-h) to monomodal with a period of $\sim 20\bar{B} - 40\bar{B}$ (for the case of confined rivers, Figure 3.11e). In the former case the lower magnitude of the wavelength interval corresponds to river class B_2 and the upper one to river class G_2. In the latter case, the lower margin of the wavelength interval corresponds to confined rivers with higher $\Delta|S_{WT}|$ such as the Beaver River, and the upper marging to lower $\Delta|S_{WT}|$ such as Steen and Red Deer Rivers.

3.4 CONCLUSIONS

The quantification of the variability of meandering rivers morphometrics is necessary for scientific (e.g. analyzing the interrelationship between meanders and riparian vegetation, the influence of sinuosity on surface and groundwater interrelationship, distinguishing natural from modeled channels, among others) and practical purposes (e.g. . the design of civil

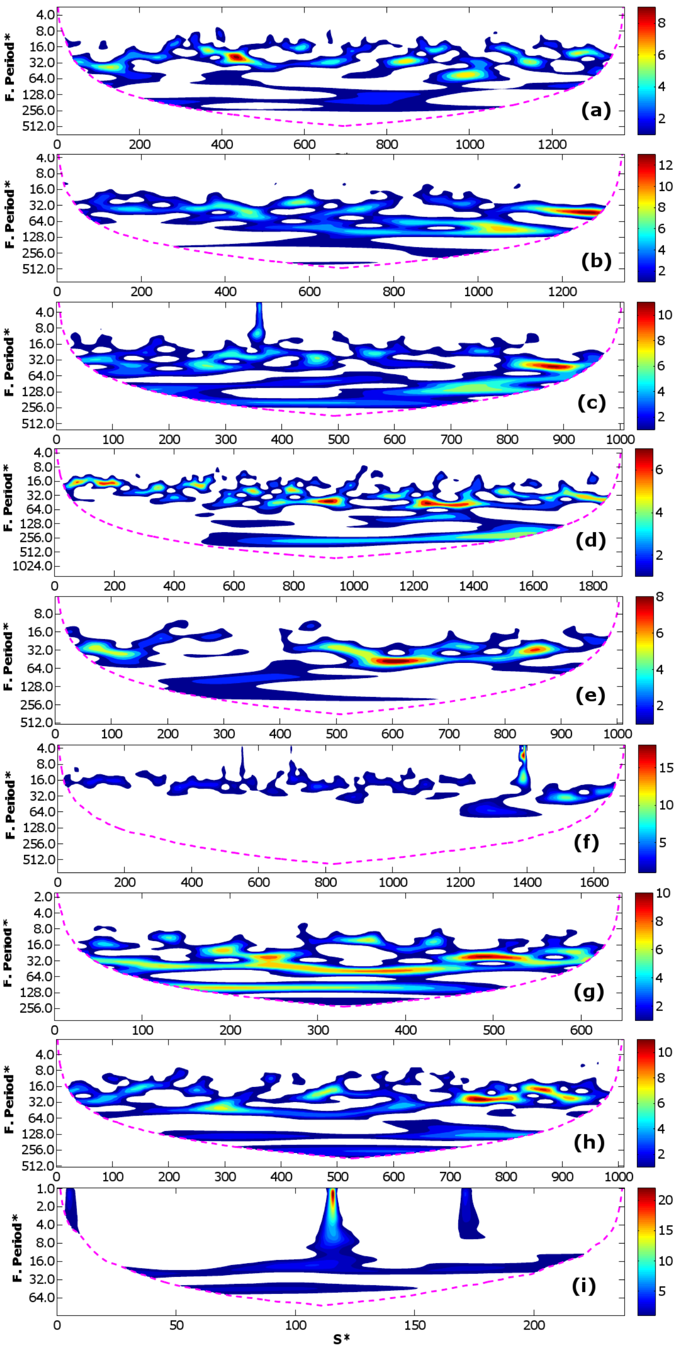

Figure 3.11: Wavelet spectrum output for the planform amplitude from Rivers (a) Pariamanu, (b) Medicine, (c) Pearl, (d) Madidi, (e) Tigre-West, (f) Beaver, (g) Tahuamanu-West, (h) Tahuamanu-East, and (i) Ucayali. The spectra show only the contours at 95% of confidence and the cone of influence (dotted magenta lines). They show a polymodal spectrum for the case of free meanders (Figure 3.11a-e and Figure 3.11g-i) and a monomodal spectrum for confined meanders (Figure 3.11f). In all the cases the represented year is 2000.

infrastructure protection, impact of reservoir on meandering planforms, river restoration, among others). Herein, a set of 16 meandering rivers (providing a total of 52 realizations) from various geographical locations that ranges class B_1, B_2, C, D, E, F, G_1, and G_2 according to the Brice modified classification scheme are studied in the present contribution. Meandering rivers geographical coordinates are treated as complex numbers such that the real part is the Easting coordinate and the imaginary part is the Northing coordinate. The combined application of the discrete wavelet transforms and the principal component analysis provides a reliable methodology to define the mean center (MC) of the river. The MC represents a robust reference to analyze river meandering parameters for middle-terms (e.g. 10-∼30 years). Historical analysis of the river centerlines shows that the Daubechies-10 wavelet —at level $J = 5$ for class F and $J = 7 - 8$ for class B, C, E, and G—best defines the MC. Therefore, the MC represents the wave from the river centerline signal having the forth-degree polynomial suppressed. The MC in confined meandering rivers (class F) is closer to the valley center; however, in the case of freely meandering rivers, it could differ from the actual valley center. Therefore, the MC shows to be a strong frame to estimate the middle term migration of meandering rivers.

The application of wavelet transforms on the normalized $C^* - S^*$ signals provides spatial distribution of the arc wavelength, the amplitudes and sinuosity with respect to the MC. The application of the wavelet coherence on the C^* reveals that these parameters exhibit high correlation with the local curvature of the MC. Thus, in confined rivers, lower local curvature at the river centerlines are related to higher MC local curvatures; conversely, in free meandering rivers, compound bends and multiple loops are associated to higher MC local curvatures; and most of the instances show that cutoffs are produced in the vicinity of peaks in the MC local curvature. The dimensionless centerline curvature fits the normal distribution after the Johnson transformation is performed. Likewise, the historical analysis of the arc wavelength provides insight on the changes in the frequency spectrum; thus, the amalgamation process of higher frequencies to produce a lower ones and the splitting of lower frequencies to produce higher ones can be quantified and identified not only in a stretch scale but also in a local scale.

We define the planform amplitudes as the orthogonal distance of the centerline from the mean center. In all of the cases, this parameter, when normalized with the river mean width, is normally distributed and typically ranges in the interval ∼2-7 for confined rivers and in the interval ∼8 to higher than 20 for free meanders (the upper bound corresponds to meanders located in tidal environments).

We introduce the application of the Fréchet distance to measure the similarity between the river centerline and the MC and the curvature wavelet entropy. When normalized with the absolute value of the maximum amplitude, the former metric shows to be a strong frame to classify free from confined meanders. Confined meanders are bounded by a normalized Fréchet distance ∼650. The absolute value of the wavelet entropy gradient effectively quantifies four degrees of dynamics of the meandering curvature signal.

4.0 CHARACTERIZATION OF CONFLUENCES OF FREE MEANDER TRAINS AT THE UPPER AMAZON BASIN

4.1 INTRODUCTION

River confluences are ubiquitous features in river networks. They represent entities at which rapid changes in flow, sediment discharge and hydraulic geometry must be accommodated [34]. Past research in this topic has shown that the main parameters that influence the dynamics of confluences are the momentum ratio between the combining flows and the three-dimensional geometry of the junction, namely the degree of discordance (defined as the relative depth of incision of the confluent thalwegs [129]) and the planform confluence angle [43]. There is also evidence that the curvature of the incoming channels should also be taken into account [39]. Geologically, river confluences are locations with different sedimentary facies which could provide significant insights into the paleomorphology of river systems [34, 56, 246]. [32, 38, 43, 216] and [217] proposed conceptual models for the hydrodynamic, bed morphodynamic and sedimentary processes that take place in river confluences. These models progressively identified six different zones at confluences: [1] zone of stagnation, [2] flow deflection zone, [3] flow separation zone, [4] zone of maximum velocity, [5] zone of flow recovery and [6] zone of shear (and the existence of a second zone of shear for pronounced bed discordance cases); and determined that the extent and location of these zones vary with the junction angle, the degree of discordance and the hydrological variability of the tributary confluences. From the morphological stand point, channel confluence can broadly divided into three elements: [1] distinct, and commonly steep, avalanche faces that form at the mouth of each of the confluence channels, [2] a region of pronounced scour within the center of the junction, and [3] bars of sediment which are formed within the post-confluence channel [34]. Earliest research (e.g. [179, 22, 32, 34]) determined that there is a positive correlation between the maximum scour depth and the confluence angle.

Contrary to the Playfair's Law [204] that stated that fluvial confluences are morphologically accordant, namely having negligible degree of discordance, past studies have demonstrated that they are mainly discordant (e.g. confluences having tributary beds higher than those of the main channel). This issue was attributed to differences in channel forming discharges and diversity in the geology and sediment size of the bed and the banks [129]. Likewise, in cases of temporal variations in uplift rate result in discontinuities in slope (knickpoints) that propagate upstream through the channel network. In the absence of diffusion or spatial heterogeneity in erodibility or uplift rate, these knickpoints progress with constant vertical velocity [186].

Confluence flow structures show some resemblance to those in meander bends, but modified because of the abrupt change in tributary direction as well as general difference involving the presence of a free-shear layer between the confluent flows. The introduction of asymmetry in terms of velocity ratio reduces sensitivity to junction angle. By far the strongest changes in secondary circulation strength arise from the introduction of bed discordance, and even low magnitude discordance may have a significant, albeit localized effect [46]. Sediment research at confluences [246, 217] indicates that [1] tributary sediments impact on the main stream, thus punctuanting the downstream trend in sediment size decrease; [2] the size of the tributary is an important factor for tributary impact on the main stream; and [3] the particle size decreases from the active flow bed towards the banks and bars.

Ribeiro et al., 2012 [217] stressed the fact that current understanding of channel confluences is based on experimental (e.g. [179, 209, 242]), field (e.g [212, 122, 199, 151, 149, 200, 246, 216]) and numerical models (e.g. [44, 45, 46, 43, 220, 68, 217]) that surprisingly represent a small number of investigated configurations. To the best of our knowledge, these configurations do not include confluences in meandering rivers. Ribeiro and collaborators also stated that although these studies have provided valuable insight in the dynamics of confluence zones, they do not represent the full range of channel confluences encountered in nature that vary in, e.g. planform and slope of the confluent channels, confluence angle, discharge and momentum ratios, bed material and sediment supply. Likewise, [199], based on field data from the confluence-diffluence case in the Parana River, warned that caution must be applied in assuming that processes observed in small channels can be scaled up linearly with increasing channel size. This limitation in the representativity of natural confluence configurations is particularly critical for the case of tropical rivers, such as those located in the Amazon catchment, from which even limited knowledge is available as underlined by [150].

River confluences are the mixing of three waters: two distinct river waters and one ground water, even if this latter is generally obscured by the higher discharge of the rivers [145]. Probably, this active interface leads to a high concentration of biota in their proximities [30, 78, 200, 193]. For the case of the Amazon system, for instance, this aspect of the confluences has a paramount importance, in the sense that confluences may have a preponderant role in its ecosystem structure. The present contribution, focuses on the study of the planimetric characteristics of the confluences of meandering rivers or meander trains located in the upper Amazon River. To that end, Wavelet transforms are applied on the curvature signals of the meandering rivers and subsequently, the transient changes of the curvature frequencies imposed by the main channel over the tributary and the by the tributary over the main channel are analyzed. Wavelet transforms have been successfully used in the analysis of river morphodynamic signals (e.g. bed forms and meander morphometrics) [58, 233, 98, 97]. Herein, this study is based not only at the point of confluence but considering the meander patterns of the upstream rivers, since the point of confluence is a consequence of the dynamics of meander trains.

4.2 DATA AND METHODOLOGY

4.2.1 Data

The confluences are comprised by three elements (Figure 4.1), namely the main channel stretch located upstream of the confluence (M), the tributary stretch (T) and the main channel stretch located downstream of the confluence (MT). The dominant arc-wavelength or Fourier period (λ), mean width (B) and reach length (L) of the aforementioned stretches are also described. Likewise, the confluence angle (ψ) is estimated using the nearest incoming channel curvatures into the confluence (see Figure 4.1).

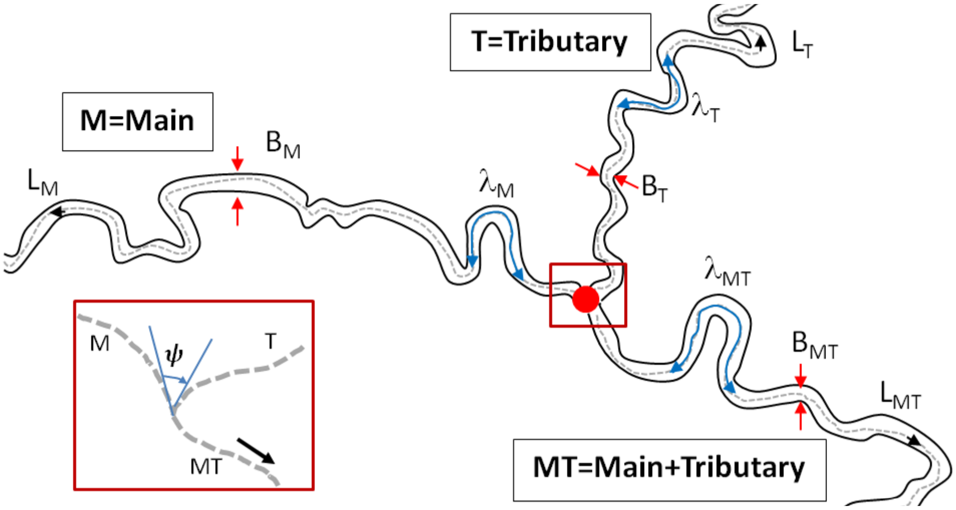

Figure 4.1: Main parameters in a confluence of meander trains. Main channel upstream of the confluence point (M), tributary channel (T) and Main channel downstream of the confluence point (MT). The M, T and MT channels were digitalized from satellite images covering an average of 40-60 bends (L_M, L_T, and L_{MT}) in each channel. The dominant arc-wavelength of the M, T and MT channels are λ_M, λ_T and λ_{MT}, respectively. The mean width of the M, T and MT channels are B_M, B_T, and B_{MT}.

The present study is based on 20 confluences located in the upper Amazon catchment (Figure 4.2) that represent confluences with the width-ratio $\beta = B_T/B_M$ ranging from 0.2 to 1. These confluences are located in the North East of Peru and North West of Brazil. Proper of environments with homogeneous and gently sloped geologic beds [30], the catchments in the study region are dentritic, as can be inferred from the flow direction shown in Figure 4.2. All of the confluence parameters are summarized in Table 4.3 and the planform configurations (satellite images from year 2000 was provided by NASA [173]) of the confluences are found in Figures 4.4 and 4.5. Notice that the confluence of meander trains involve at least the digitalization of around 40-60 bends, thus the sampling data is quite representative from confluences the world.

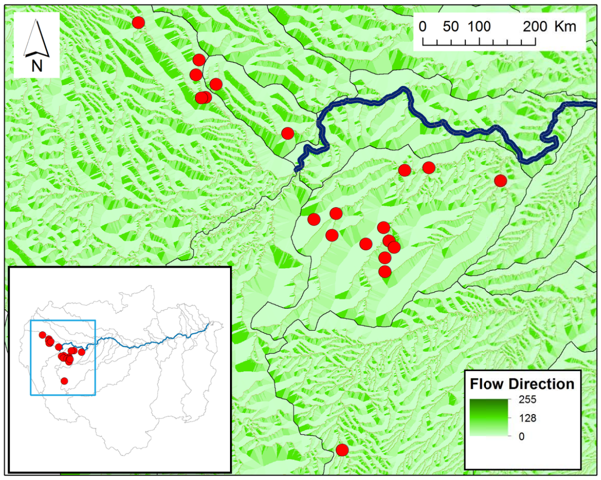

Figure 4.2: Location of the confluences used in this study and the flow direction in the study area, after [172]. The inset shows that the studied confluences are located in the upper part of the Amazon river (represented by the bold blue line). The flow direction map indicates that the river network is dentritic.

4.2.2 Methodology

The continuous wavelet analysis of the meander curvature signals for the M, T and MT channels is performed herein. The continuous unidimensional wavelet transform of a signal $x(t) \in L_2$ is obtained by the convolution of the signal and the wavelet function or mother wavelet $\psi(t)$ as expressed by Equation (4.1), where a is the scale parameter, b is the location parameter and $\bar{\psi}_{a,b}(t)$ is the complex conjugate of $\psi_{a,b}(t)$, as mathematically represented by Equation (4.2). According to the Parseval's theorem [14] the same wavelet transform can be expressed by Equation (4.3).

$$T(a,b) = \int_{-\infty}^{\infty} x(t)\bar{\psi}_{a,b}(t)\,dt, \text{ for } a > 0, \tag{4.1}$$

$$\psi_{a,b}(t) = \frac{1}{\sqrt{a}}\psi(\frac{t-b}{a}) \tag{4.2}$$

ID	**Longitude**	**Latitude**	**L_M**	**L_T**	**L_{MT}**	**B_M**	**B_T**	**B_{MT}**	**β**	**ψ**
			(Km)	**(Km)**	**(Km)**	**(m)**	**(m)**	**(m)**	**BT/BM**	
1	74.969	3.322	248	91	152	165	113	235	**0.7**	74
2	75.069	2.726	36	49	50	89	46	99	**0.5**	83
3	75.119	2.964	50	35	91	99	45	113	**0.5**	82
4	75.035	3.332	73	23	78	229	37	240	**0.2**	89
5	73.652	3.898	185	62	127	111	110	204	**1.0**	51
6	76.035	2.128	78	89	136	75	73	128	**1.0**	69
7	74.802	3.116	27	43	78	43	40	69	**0.9**	61
8	72.119	5.402	136	97	245	111	100	176	**0.9**	52
9	71.402	4.447	302	183	324	175	173	294	**1.0**	104
10	71.785	4.488	192	138	110	158	106	204	**0.7**	81
11	72.885	5.177	79	93	108	93	81	135	**0.9**	129
12	73.235	5.271	53	39	93	63	48	81	**0.8**	111
13	72.952	5.524	102	42	77	79	49	93	**0.6**	73
14	72.402	5.665	64	60	97	61	54	80	**0.9**	161
15	72.035	5.615	77	34	59	105	49	116	**0.5**	76
16	72.102	5.884	88	52	77	80	69	105	**0.9**	36
17	72.102	6.106	36	37	52	52	42	69	**0.8**	105
18	71.952	5.718	18	12	34	38	30	49	**0.8**	40
19	70.252	4.653	105	106	88	129	124	218	**1.0**	67
20	72.785	8.951	180	76	249	86	59	112	**0.7**	81

Figure 4.3: Confluences in the North East of Peru and North West of Brazil.

$$T(a,b) = \frac{1}{2\pi}\int_{-\infty}^{\infty} \hat{x}(f)\bar{\hat{\psi}}_{a,b}(f)\,df \tag{4.3}$$

where $\hat{x}(f)$ and $\hat{\psi}_{a,b}(f)$ are the Fourier transforms of $x(f)$ and $\psi_{a,b}(f)$, respectively. The wavelet power spectrum is defined as $|T(a,b)|^2$; and in terms of computational cost, it is less expensive to quantify it from Equation (4.3) [243]. Past experience has demonstrated that the Morlet wavelet function is the most efficient function in retrieving higher frequencies of bedforms [98] and river curvature [97]. Therefore, the continuous wavelet analysis herein is performed by using the Morlet wavelet function and a modified version of the Wavelet toolbox provided by [243].

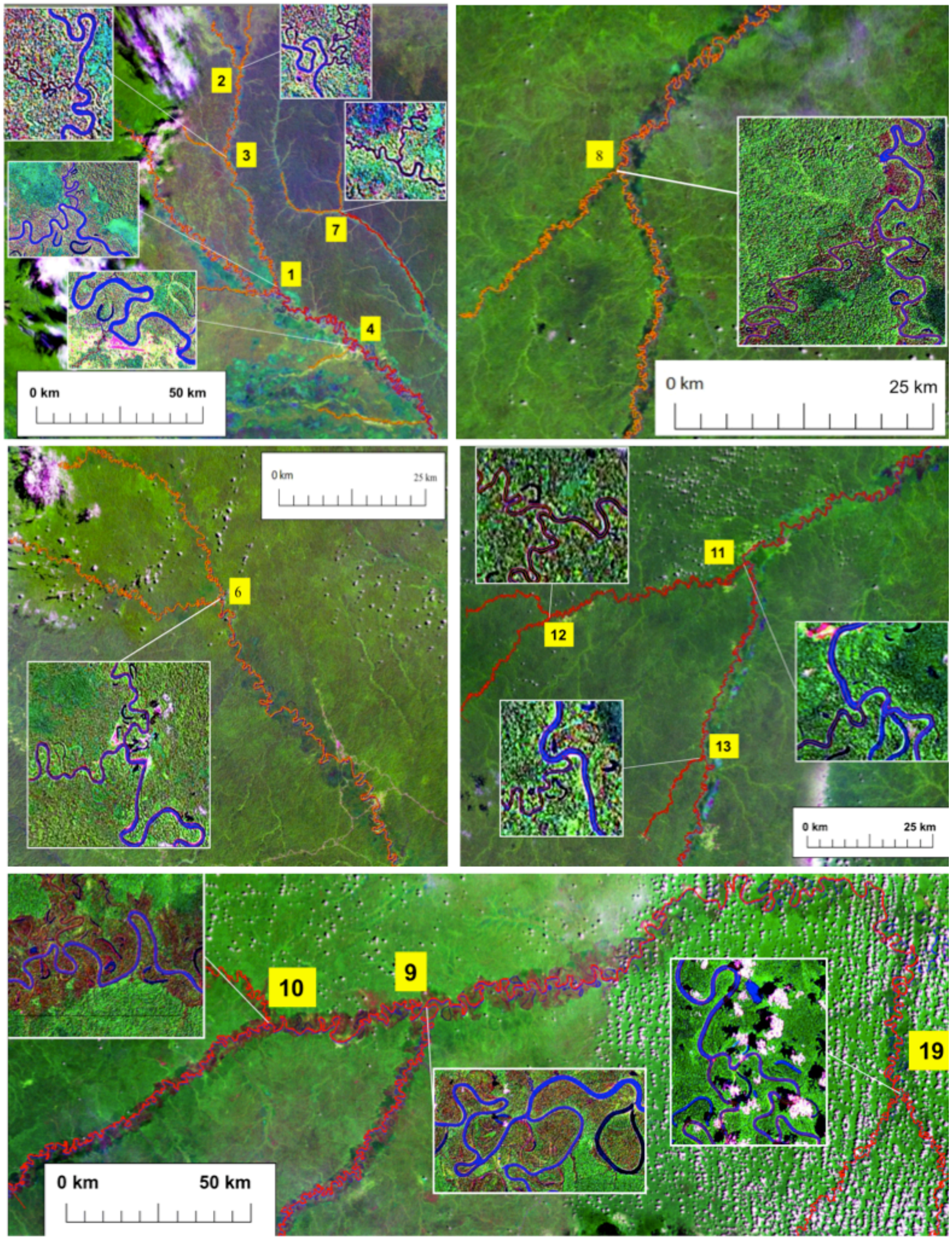

Figure 4.4: Plan view of some of the confluences (1, 2, 3, 4, 6, 7, 8, 9, 10, 11, 12, 13, and 19). For their geographic locations, please see Figure 4.3.

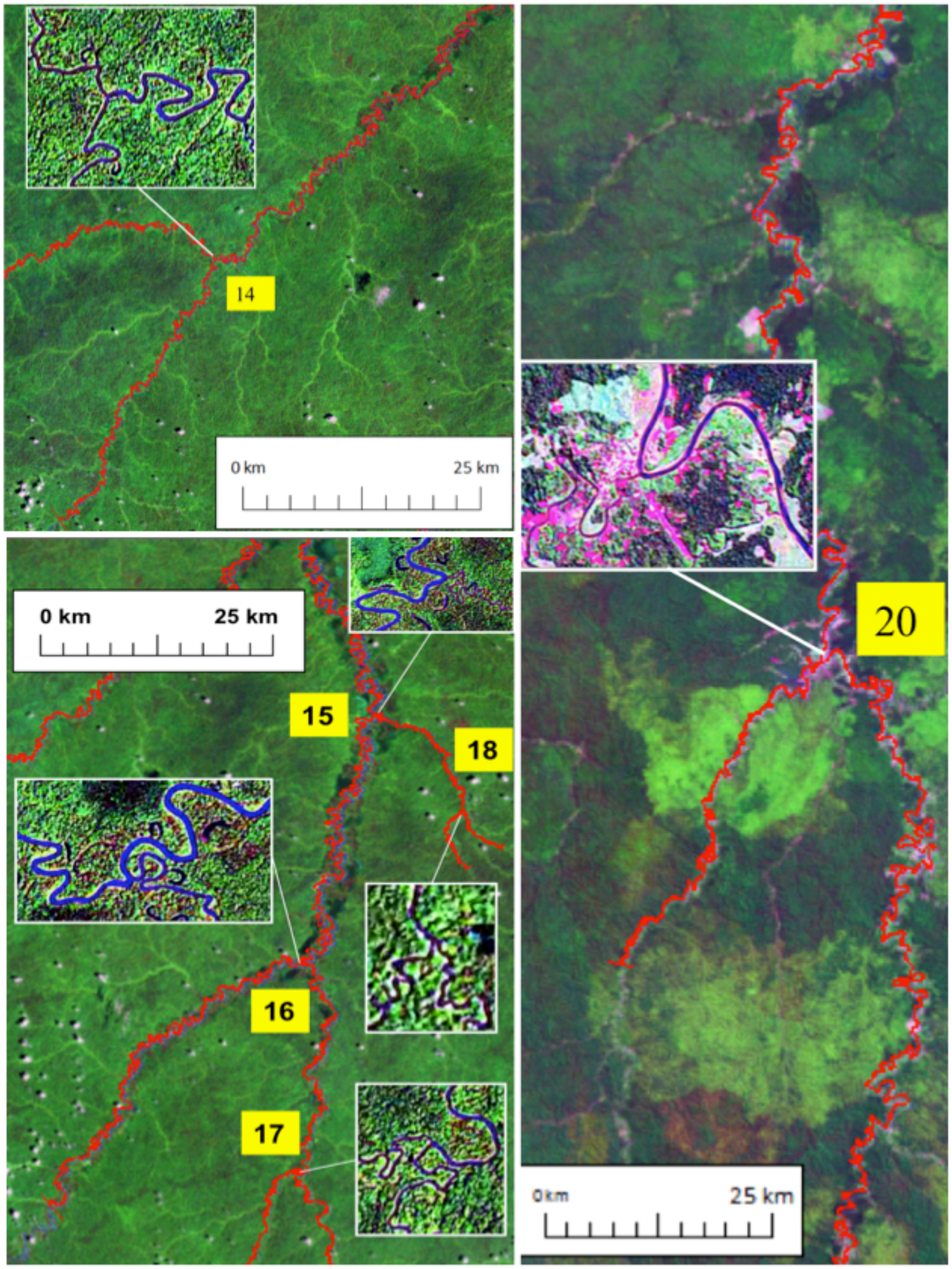

Figure 4.5: Plan view of some of the confluences (14, 15, 16, 17, 18, and 20). For their geographic locations, please see Figure 4.3.

4.3 RESULTS

4.3.1 Changes in the Curvature Patterns

Some reserachers stated that in terms of flow processes, the confluence angle is an independent variable [246]; although some modeling (e.g. [107, 73]) and field evidence (e.g. [74]) suggest that confluence angles can be described by a Gaussian distribution with an average of 72° and that they are a function of $Q\alpha So^z$, where Q is the water discharge, So is the bed slope and z ranges from $-2 \leq z \leq 0$. [107] suggested that the confluence angle (ψ) can be estimated by the following relationship:

$$\psi = \cos(So_{MT}/So_M) + \cos(So_{MT}/So_T) \tag{4.4}$$

Q and So were not estimated in the present study; however, they are considered to be proportional to the mean channel width [194, 155]. Thus, α was estimated by replacing So by B in Equation 4.4, but neglecting the cosine operator. Figure 4.6 shows that the $\alpha = 3.5$ approximately represent the mean value of the data. The highest value corresponds to Confluence 4 and can be explained by the fact the there is another confluence located upstream and closer to Confluence 4. Certainly, further work is needed to estimate a relationship between ψ and α that fully describe the confluence angle in meandering rivers.

4.3.2 Spatial Variability of Dominant Arc-wavelengths Along the Transitional Region

The planimetric geometry of meandering rivers is typically described in terms of the curvature (C). This parameter is obtained by discretizing the channel centerline in equally-spaced points and it is expressed in local or intrinsic coordinates [184, 108, 170, 154, 181]. The analysis presented herein was performed by using normalized curvature (C^*) and normalized local abscissa (S^*) data, such that $C^* = CB_M$ and $S^* = S/B_M$ (S is the streamwise coordinate). Figures 4.4 and 4.5 show the planform configuration of the confluence of meander trains, herein, only few of these confluences will be explained in detail.

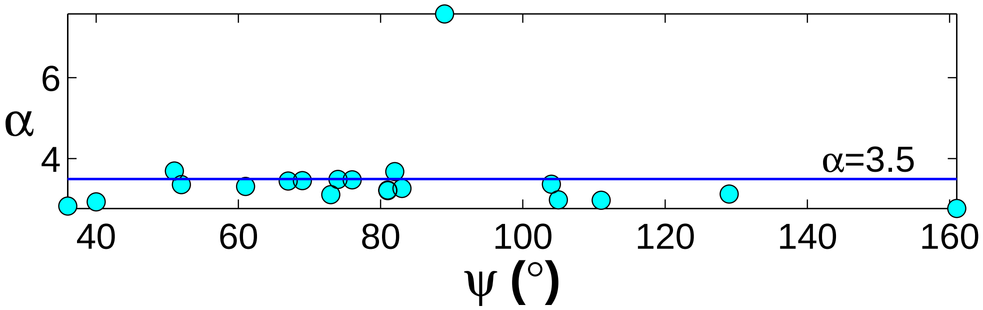

Figure 4.6: Actual angle of confluence (ψ) and α, the indirect estimate of ψ from Equation 4.4 (replacing So by B and neglecting the cosine operator). The red bold line ($\alpha = 3.5$) represents the mean value of the data. The highest value corresponds to Confluence 4, located very close to another confluence (not included in the present study) located upstream of Confluence 4.

4.3.2.1 Confluence 5 ($\beta \sim 1.0$ and $\psi = 51°$) Figure 4.7(a) presents the confluence of almost two identical rivers (in terms of the channel width, $\beta = 1$). Figure 4.7(b.1) shows that in a geological time scale, there would be a radius of influence where the instantaneous point of confluence can change depending on the dynamics of the M and T channels. Herein, we are not showing historical evidence of the radius of influence (R^c) for Confluence 5, since, thus, this study is focused on the arc-wavelenghts of the instantaneous configuration of the M, T and MT channels (Figure 4.7(b.2) and (b.3)). Figure 4.7(c) shows the normalized curvature signal for M and MT channels. It shows that after the confluence point, the peaks of the curvature decreases, thus the adaptation of the morphodynamic shapes require some spatial parameters such as R^*_M, R^*_T, and R^*_{MT} (these parameters are being normalized by using B_M). Figure 4.7(d) shows the wavelet output for the M and MT channel (using the M and MT channel curvature), where the dominant arc-wavelenght (calculated using the Wavelet power spectrum) for the M and MT channels are $\lambda^*_M \sim 14.9B_M$ and $\lambda^*_{MT} \sim 24.2B_M$, respectively. This increase in the MT arc-wavelength can be observed on the Satellitle image (Figure 4.7(a)). Due to the confluence of these two freely meandering rivers, there is an effect upstream and downstream where the planform morphology requires some lag for adaptation.

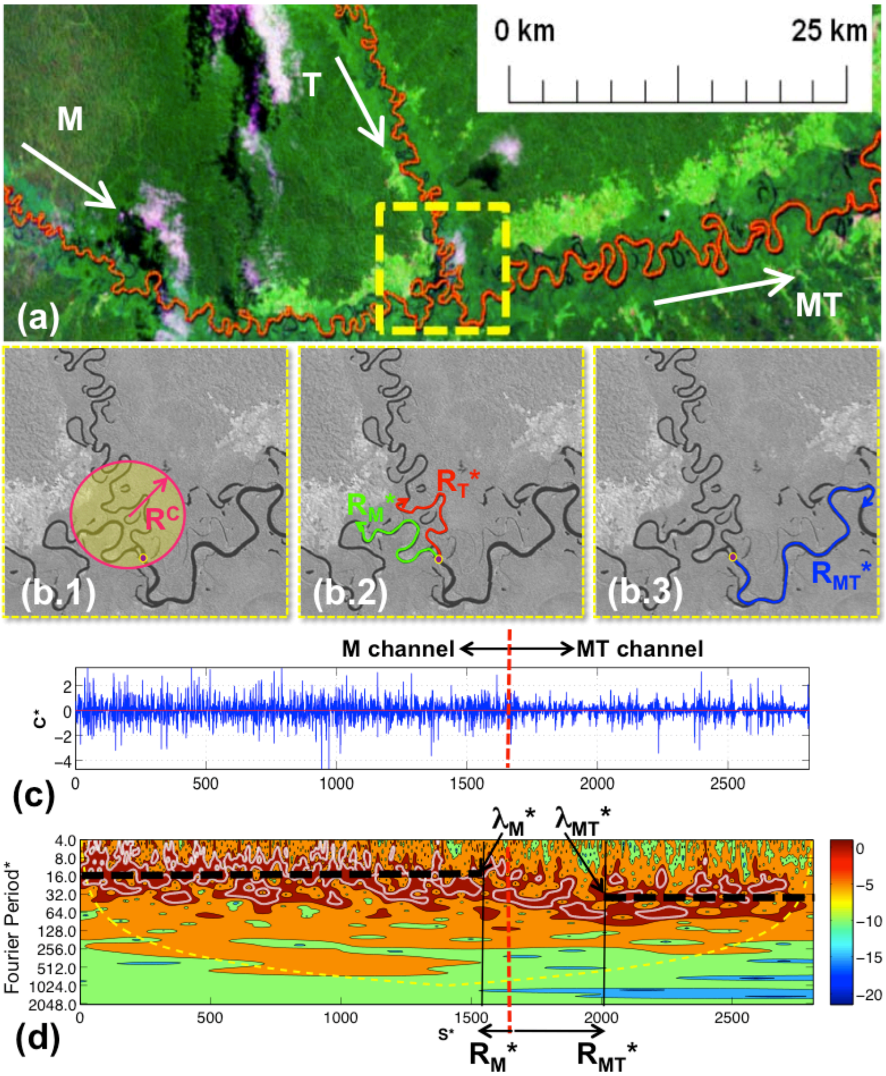

Figure 4.7: Confluence 5. (a) Plan view in the year 2000, (b) plan view detail in year 2011 (b.1: Radius of the confluence point, b.2: R_M^* and R_T^*, and b.3: R_{MT}^*), (c) Normalized streamwise curvature ($C^* = CB_M$) versus the normalized streamwise coordinate ($S^* = S/B_M$), (d) Wavelet output (normalized Fourier period represents that normalized arc-wavelenght) of the M and MT channels. Notice that the red dashed line shows the confluence location. The dotted yellow line represents the cone of influence border and the bold lines represent the contours at 95% of confidence of finding bends at those locations. The normalized streamwise coordinate (S^*) and the normalized Fourier Period or arc-wavelength ($F.\ Period^*$) are being normalized by B_M.

These influences are denominated $R^*_M \sim 118.3B_M$ and $R^*_{MT} \sim 331.7B_M$. Herein, these parameters were computed by using the Wavelet power spectrum and by observing the tendency of the wavelet output (Figure 4.7(d)). These transitional regions (upstream and downstream of the confluence point) could depend on several specific parameters (e.g. flow hydrograph of the M and T channels, bed elevation at the point of confluence, geological constrains of the M and T channels, among other parameters), herein, the characterization of the transitional regions are made based solely on the normalized curvature signal for the M, T and MT channels. Even though β is close to 1 for this confluence, the position of the confluence point has not moved in the last 30 years, suggesting that a relative slow evolution takes place in this confluence. However for geological time scale, some evidence of changes on ψ and the confluence planform dynamics could be found.

4.3.2.2 Confluence 4 ($\beta \sim 0.2$ and $\psi = 89°$) For the Confluence 4, the Wavelet power spectrum output at 95% shows few bends along the M and MT channels, since the length of the upstream and downstream reaches might not be enough to be considered representative (there are confluences upstream and downstream); thus, a 75% confidence interval is used instead of the 95% to compute the dominant arc-wavelengths and the transitional region parameters. It seems that for this confluence, there is not a notorious difference between dominant parameters upstream and downstream of the confluence ($\lambda^*_M \sim \lambda^*_{MT} \sim 8-32B_M$), since the perturbations (from the T channel, $\lambda^*_T \sim 0.5-2B_M$) is quite small ($\beta = 0.2$). Thus, when β is quite small, the changes in the planform morphodynamics of the MT channel are not quite important or it could be neglected. Notice that this analysis is being performed considering only geometric parameters related to channel configuration and channel width. At this point, hydraulic and sediment transport processes are not incorporated explicitly, rather than analyzing the planform morphodynamic behavior of meander trains. For this case, the parameters for the transitional region, R^*_M, R^*_T, and R^*_{MT} are very small and they could be neglected.

4.3.2.3 Confluence 1 ($\beta \sim 0.7$ and $\psi = 74°$) For instance, Figure 4.9(a) shows the Wavelet power spectrum for the M and MT channels. The contour regions represent the

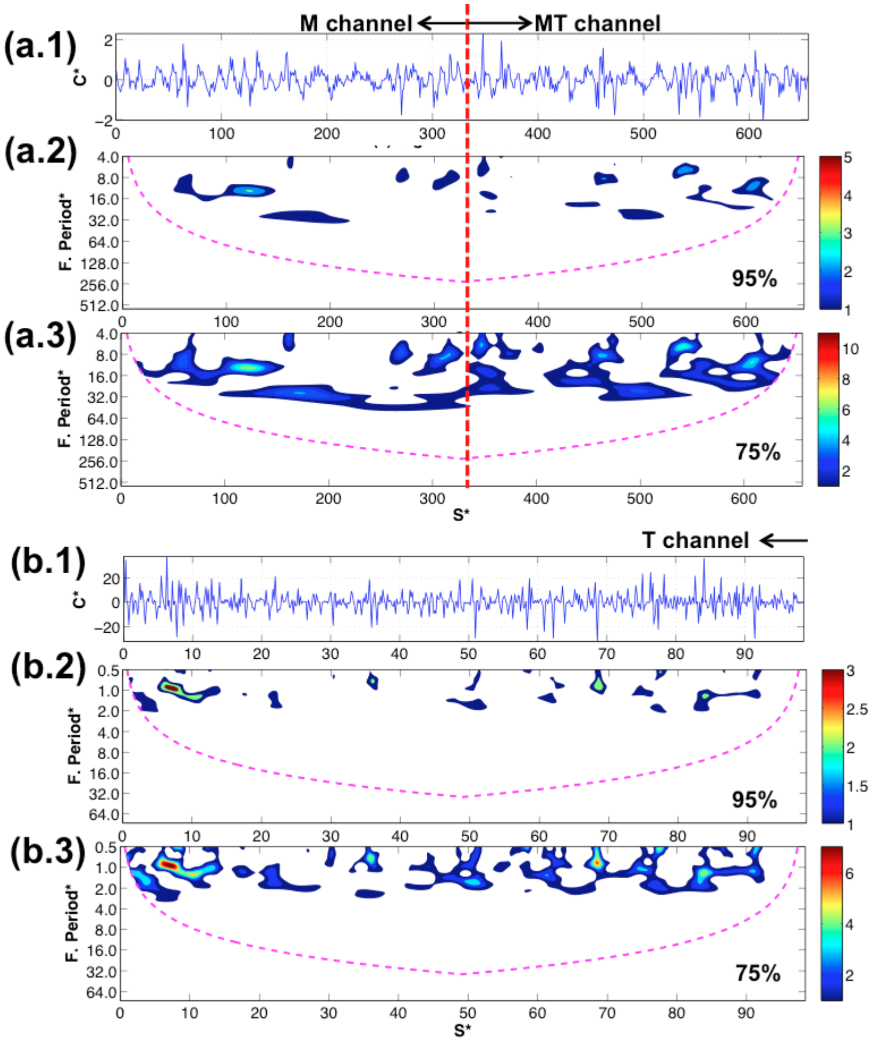

Figure 4.8: Wavelet output for Confluence 4. (a) M and MT channels, (b) T channel. Magenta dashed lines are showing the cone of influence border for 95% or 75%. The normalized curvature signal does not present major changes after the confluence point for the M and MT channel, and there is no an upstream effect into the T channel. The normalized streamwise coordinate (S^*) and the normalized Fourier Period or arc-wavelength ($F.\ Period^*$) are being normalized by B_M.

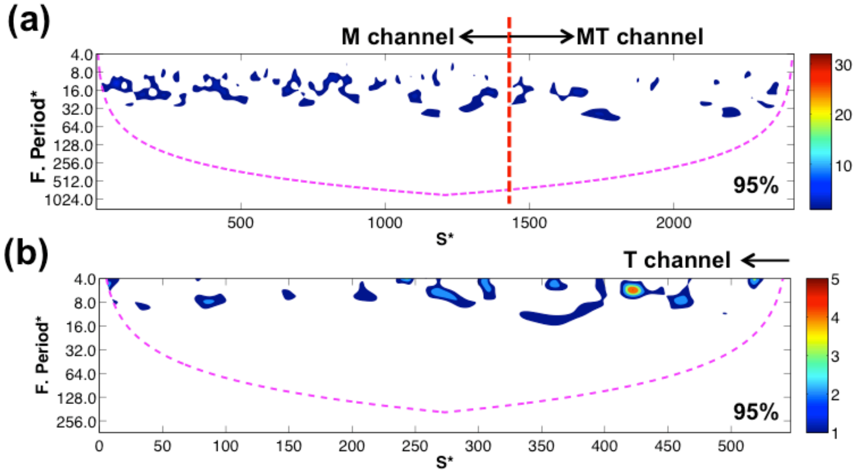

Figure 4.9: Wavelet power spectrum output of the dimensionless curvature at Confluence 1. (a) Wavelet spectrum of M and MT channels, (b) Wavelet spectrum of the T channel. The normalized streamwise coordinate (S^*) and the normalized Fourier Period or arc-wavelength ($F.\ Period^*$) are being made dimensionless by B_M.

wavelet power spectrum at 95% of confidence and the dotted magenta line represent the cone of influence. The vertical bold red dashed line represent the location of confluence 1 ($S^* \sim 1450$). At Confluence 1, no evident perturbation to the original curvature signal is observed (the train of bends from the upstream stretch along the main channel are maintained downstream of the confluence). It may be explained by the fact that there is an upstream confluence with $\beta = 0.6$ very close to Confluence 1 (see Figure 4.4), thus the train of bends enter to Confluence 1 region without recovering its dynamic equilibrium stage and bend maturity. Similarly, Figure 4.9(b) shows that no marked perturbation is imposed in the power spectrum of the T channel. The normalized dominant arc-wavelengths along the M, T and MT channels are: $\lambda_{M^*} \sim \lambda_{MT^*} \sim 8 - 32B_M$, and $\lambda_T \sim 4 - 10B_M$. Under these conditions, where no major changes on the dominant scales are described upstream and downstream of the confluence, the parameters for the transitional region (R^*_M, R^*_T, and R^*_{MT}) are negligible.

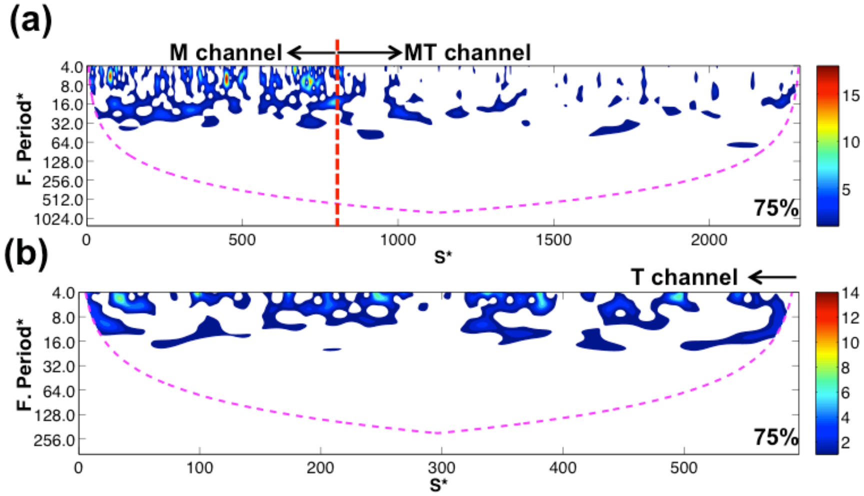

Figure 4.10: Wavelet output for Confluence 12. (a) M and MT channel stretches (the dotted vertical red line represents the location of the confluence), and (b) T channel. For the sake of better visualization, only the contours at 75% of confidence and the cone of influence (dotted magenta lines) are presented.

4.3.2.4 Confluence 12 ($\beta = 0.8$ and $\psi = 111°$) For Confluence 12, a marked perturbation in the dominant arc-wavelength in the M, MT and T channels is observed (Figures 4.10(a)-4.10(b). The dominant arc-wavelengths along the M, MT and T channels are: $\lambda_{M^*} \sim 4 - 32B_M$, $\lambda_{MT^*} \sim 8 - 64B_M$, and $\lambda_T^* \sim 4 - 16B_M$. Under these conditions, no major changes in the dominant arc-wavelength are described upstream and downstream of the confluence along the M, T and MT channels, however, there is a change in the periodicity of these bends as the contour regions diminished along the streamwise coordinate.

4.3.2.5 Confluence 19 ($\beta \sim 1.0$ and $\psi = 67°$) Figures 4.11 (a) and (b) present Wavelet power spectrum. The dominant arc-wavelengths along the M, MT and T channels are: $\lambda_{M^*} \sim 4 - 32B_M$, $\lambda_{MT^*} \sim 16 - 32B_M$, and $\lambda_T^* \sim 8 - 32B_M$. From Figure 4.11 it seems that even though there is not a notorious change in the dominant arc-wavelength, there is a change in the periodicity of finding bends with a specific length scale.

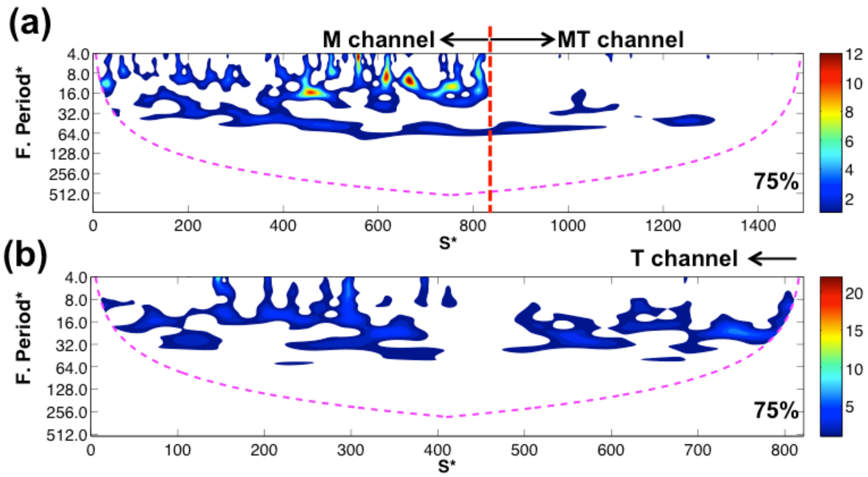

Figure 4.11: Wavelet output for Confluence 19. (a) M and MT channels and (b) the T channel. Note that a dramatic change in the main channel frequency spectrum is imposed by the confluence; in the tributary channel the channel is straighten close to the confluence as the higher and lower frequencies are suppressed.

4.3.3 Discussion

Most of the widely used softwares to model freely meandering channels (e.g. RVR meander, MIANDRAS, iRIC) are based on deterministic equations that are solved by assuming the simplifications described by [238]: [1] the channels width is spatially and temporal constant, [2] the water surface super-elevation is linear, [3] the energy gradient is uniform along the downstream direction, [4] the average channel depth is uniform in the downstream direction, [5] transient bed forms (e.g. ripples, dunes, migrating bars) are not included, [6] negligible sidewall effects exist on the near-bank flow. Likewise, it is assumed that the discharge is spatially and temporally constant [181]. At confluences, these assumptions may not be valid; therefore, future work in confluence modeling at catchment scales will require the coupling of the physically-based equations with statistical information retrieved from the channel morphometrics such as the probability distributions that describe the confluence angles ([74]) and meanders curvature ([97]).

The study of the morphodynamics of the meandering confluences should consider catchment parameters such as the proximity between confluences and the shape of the catchment. Previous studies indicate that heart shaped and pear shaped basins containing dentritic networks favor increasing tributary size and hence greater confluences effects downstream compared with rectangular basins containing trellis or parallel networks [30, 246]. This fact is closely related to the variability of the channel discharges. Past research has demonstrated that river geometry is a function of river flow time sequence, thus channels narrow as a function of increasing annual flood variability. Therefore, it is impossible to associate the channel geometry with a single discharge of a certain frequency of occurrence, because the role of the discharge depends heavily on the current channel form which is an end result of antecedent flows [266, 255]. Furthermore, [255] states that bank erosion rate distributions in a bend show a high sensitivity to the flow sequencing. Visconty and his collaborators observed a relevant downstream migration of the erosion regions in the experimental setups with a variable discharge. Field investigations also confirms (e.g. [203]) that channel width is influenced by a wide variety of formative discharges.

4.4 CONCLUSIONS

The study of confluences is important for practical and scientific purposes. For scientific purposes it is important to understand the confluence dynamics and the parameters that govern it. Several studies have revealed that confluences have a preponderant role in the ecosystem structure of rivers. Even though past studies have casted light to better understand the morphodynamics of confluences, they are based on the experimental, field and modeling representation of a limited number confluence conditions (e.g. slopes, discordance degrees, river types, discharge and momentum ratios) and localized to the instantaneous confluence point. This study focuses on meandering rivers confluences and, to the best of our knowledge, there is not precedent study on the matter, trying to identify the main morphometrics from confluences of meander trains.

Given the relevance of the the Amazon River as the world's largest river and its role to sustain the humankind, this study has focused on meandering confluences located in the upper Amazon catchment. The study is based on 20 confluences in which the width-ratio (β) ranges between $0.2 - 1$. Confluence of meandering rivers or meander trains (asumming one is the main channel and the other a tributary) imposes the following general changes in the planimetric configurations of these channels: [1] modulation of the morphodynamics of the upstream main (M) and tributary (T) channels and [2] modulation of the morphodynamics of the downstream main channel (MT), thus increasing the arc-wavelength and amplitude and resembling a constructive effect in the superposition of curvature waves. Thus, in all the channel stretches, transient curvature lengths are developed.

5.0 APPLICABILITY OF TWO-DIMENSIONAL WAVELETS IN THE ANALYSIS OF THREE-DIMENSIONAL BED FORMS

5.1 INTRODUCTION

Most of the past studies on river bedforms dynamics have concentrated on two-dimensional forms, with constant heights and straight crest lines transverse to the flow and their associated turbulent flow structure. This morphological simplification has imposed inherent limitations on the interpretation and understanding of dune form and flow dynamics in natural channels, where dune and ripples are predominantly three-dimensional [198].

Past approaches to the quantification of bedform variability have used and applied spectral analysis [115, 19, 156, 132], smoothing techniques such as a moving-average [250], signal roughness techniques [232], fractals [260], and logistic regression [123]. [98] applied robust spline filters and one-dimensional continuous wavelet transforms to discriminate bedform features at different scales, namely bedform hierarchies, and argued that two-dimensional wavelet transforms, when coupled with two-dimensional robust spline filters, would substantially improve the discrimination methodology for predominantly three-dimensional bedform features.

This chapter focuses in the state of the art of the application of two-dimensional wavelet transforms and in the design of synthetic bed form signals that might be used benchmark signals for calibration of the wavelet functions parameters (e.g. dilation, translation and rotation parameters). Future work in this regard may use this study to: (a) estimate the dominant wavelengths, amplitudes and slopes; and (b) retrieve the predominant directions of the bifurcations for three-dimensional (3D) bedform data.

5.2 CONCEPTUAL FRAMEWORK

5.2.1 Two-Dimensional Wavelet Transforms

Similarly to one-dimensional wavelets there are discrete and continuous two-dimensional wavelet functions. Generally speaking, the former wavelets functions have been used to the great extent in the analysis of images synthesis and compression; while the latter have been used in the determination of specific features, such as hierarchical structure, edges, filaments, contours, boundaries, etc. [20].

At present, 2D wavelets have not been used in the analysis of 3D bedforms. Antonie et. al., 2004 [20] pointed out that recent applications of 2D continuous wavelets in climatology (e.g. analysis of hurricanes, radar-depicted spatial rainfall, enhancement of thin-line features of in meteorological radar reflectivity images, etc.) and fluid dynamics (detection of coherent structures in turbulent flows, velocity field, disentangling of a wave train, etc.)
There are mainly two types of 2D continuous wavelet functions, namely: [1] isotropic wavelets (e.g. 2D Mexican hat wavelet), which are used when no oriented features are present in the or relevant in the signal; and [2] anisotropic wavelets (e.g. the 2D Morlet wavelet), whose effective support of its Fourier transform is contained in a convex cone in spatial frequency space with the apex at the origin. They are used when marked oriented features are present in the signal. Past experience in the matter indicates that the latter wavelets perform better when noise is present in the signal [20].

For the present research, 2D versions of the Mexican Hat (a real wavelet function) and Morlet (a complex wavelet function) wavelets will be used. Equations (5.1), (5.3) and (5.2) represent the mathematical definitions of the 2D wavelet transform, Morlet wavelet function and Mexican Hat wavelet function in its isotropic version, respectively. Graphical representations of the aforementioned wavelet functions are presented in Figure 5.1.

$$T(a,b) = \frac{1}{\sqrt{a}} \int_{-\infty}^{\infty} \int_{-\infty}^{\infty} f(x,y)\bar{\psi}(\frac{x-b}{a}, \frac{y-b}{a})\, dxdy, ; \text{for } a > 0 \tag{5.1}$$

$$\psi_{MH}(x,y) = (x^2 + y^2 - 2).e^{-\frac{1}{2}(x^2+y^2)} \tag{5.2}$$

$$\psi_H^{\theta}(x,y) = e^{i(w_1^0 x + w_2^0 y)} e^{-(x^2+y^2)/2}; \text{ for } |(w_1^0, w_2^0)|> 5; \text{ and } \theta = tan^{-1}\frac{w_2^0}{w_1^0} \tag{5.3}$$

where w^0 represents the wave vector and $0 \leq \theta \leq 2\pi$ indicates the direction of the wavelet [89]. The condition $|(w_1^0, w_2^0)|> 5$ is necessary to comply with the admissibility condition, namely $\hat{\psi_M^{\theta}}(0,0) = 0$ (the hat symbol denotes the Fourier transform).

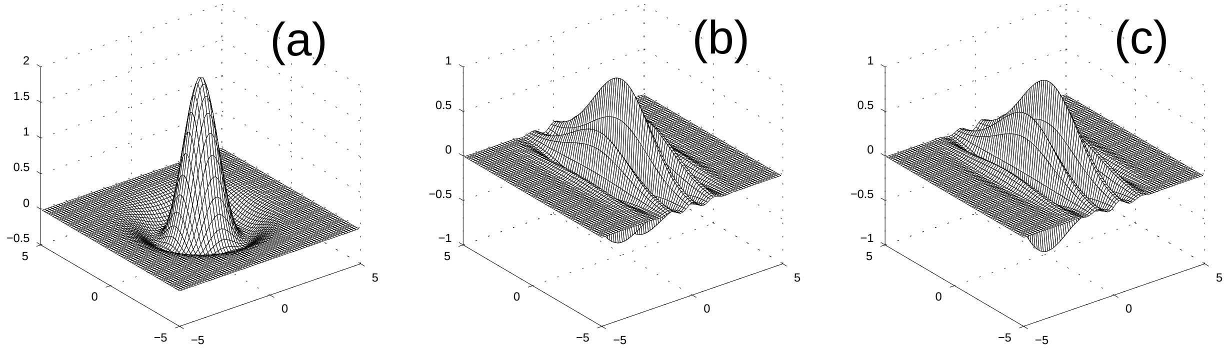

Figure 5.1: 2D wavelet functions: (a) Mexican Hat (isotropic version) in the position domain, (b) Morlet - real part in the position domain, and (c) Morlet - imaginary part in the position domain for $w^0 = (5, 500)$.

5.2.2 Recent Applications of 2D Wavelets in the Analysis of Surface Topography, Edge Detection and Geophysical Signals

In order to retrieve important information regarding to the orientation of the crests and troughs of bedforms at different scales, it is necessary to apply edge detection techniques. 2D continuous Gabor wavelets have been successfully used in palmprint verification (e.g. [262]) and wavelet entropy has been used to define an optimal threshold selection for edge detection (e.g. [261]). The former methodology couples the capabilities of the of two-dimensional Gabor wavelets and pulse coupled neural network and proved to be robust to the variations of orientations position of past approaches on the matter; although shows to be computationally expensive [262]. The latter methodology achieved the automatic selection of the optimal threshold by estimating the minimum entropy of the two-dimensional data and proved to be more efficient than the Donoho's and Madchakham's methods [261]. Having the peaks and troughs of the bed form data is particularly important to analyze multi-temporal bed form data which is common in experimental research, three-dimensional correlation can be performed in order to measure the three-dimensional evolution of bed form features (e.g. ripples, dunes, bars), estimate the rates of migration and quantify the descriptors of the bed forms splitting and amalgamation processes.

Dunes represent coherent structures in bed form data. Therefore, we believe that past experience of the application of wavelet transforms in the extraction of coherent structures in turbulent flow should be used. Discrete wavelet transform and discrete wavelet packet transforms have been used to discriminate low entropy "coherent" (similar to dune and bar features) and high-entropy "incoherent" (similar to ripple features) components of vorticity, as reported by [227]. This research work found that only about 3% of the large amplitude coefficients of the discrete wavelet transform and discrete wavelet packet transforms are necessary to represent the coherent component and preserve the vorticity probability distribution function and spatial and temporal correlations.

Past application of 2D real discrete wavelets transforms on image processing and surface topography has proved that they (first and second-generation wavelets) lack shift invariance and directional sensitivity, which resulted in aliasing and that they are limited in extracting morphological features without undesirable artifacts such as the pseudo-Gibbs effect [165]. This is explained by fact that wavelet transform focuses only on the low frequency decomposition in a successive manner but the dominant spatial frequencies of, for instance, image textures are usually located in middle frequency regions [61]. Thus, similar textures with symmetric orientations are almost indistinguishable in the wavelet domain [109]. In order to overcome these limitations of the discrete wavelet transforms the adaptive modulated wavelet transform (e.g. [110]) and the orthogonal quincunx wavelets with fractional orders (e.g. [86]) were proposed. Recently, complex ridgelets (e.g. [166]) and dual-tree complex wavelet transforms (e.g. [165], [59]) have been successfully used in minimizing the aforementioned artifacts of the real discrete wavelet transforms.

5.3 METHODS AND RESULTS

5.3.1 Synthetic Signals

In order to determine benchmark data to estimate the capabilities and limitations of the 2D Morlet and 2D Mexican hat wavelets two main types of synthetic bed forms were generated, namely:

5.3.1.1 Type 1 - Synthetic Signals They represent 3D data comprised by the same bars, dune and ripples waves described in Section 2.2.2.1. A variation of this data is represented by dunes that present waviness in the X-axis and Y-axis. The equation that describes this 3D synthetic bar is given by Eq. 5.4.

$$\eta_{3,3} = a_x \sin(2\pi X/T_x - c_x) + a_y \sin(2\pi Y/T_y - c_y) + s_3 X \tag{5.4}$$

where a_x = 0.05; a_y = 0.05; T_x = 400; T_y = 400; c_x = 100; c_y = 100; s_3 = -0.005; and X and Y represent the coordinate matrices at the x-axis and y-axis, respectively. Figure 5.3a-b respectively show a detail of this signal and the extension of the synthetic plot.

5.3.1.2 Type 2 - Synthetic Signals There is a constant scaling of bed form height versus length over five orders of magnitude (see Figure 5.2). These universal bed form data indicates that bed form steepness decreases continuously with increasing wavelength, and cast doubt on the idea that steepness is a diagnostic of bed form type [117]. Likewise, past research indicates that both dune and ripple height is best described by Gamma probability distribution. Therefore, the Type 2 - synthetic data was defined by: [1] generating Gamma distributed data with $5 < \lambda < 10$ (small dunes) and $10 < \lambda < 100$ (medium dunes); [2] generating random slopes bounded by 0.0677 and 0.16; thus, by knowing the slope and the wavelengths the dunes height were estimated; [3] using the equation that describes mature dunes (see Section 2.2.2.1) the geometry of the dunes were generated; and [4] 2D bars (see Section 2.2.2.1) and 3D bars similar to the ones used for generating Type 1 synthetic signals were used. Figure 5.3d-e show the geometry of a typical cross section and the 2D synthetic plot, respectively.

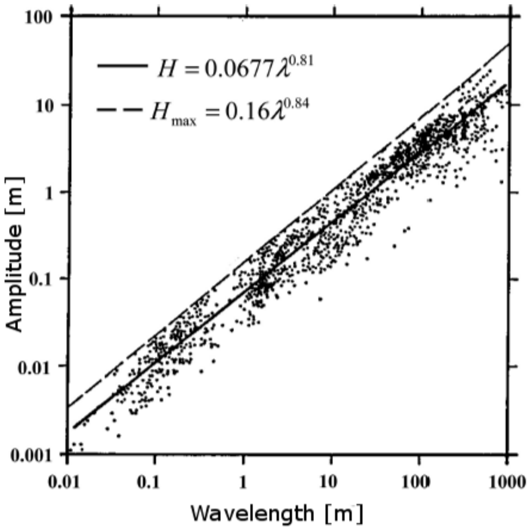

Figure 5.2: Plot of bedform height versus length (after [117]) for a collection of field and laboratory data. Mean and maximum best-fit power law relationships are shown on the plot.

5.3.2 Results

Perron et. al., 2008 ([201]) used two-dimensional Fourier transforms to study high resolution topographic maps. Perron and his collaborators successfully retrieved quasiperiodic ridge-and-valley structures. The two-dimensional Fourier transform was applied on the bed form synthetic signals. The results (Figures 5.3c and 5.3f) show that it is limited in identifying the spectrum of frequencies that are present in the signals. As shown in Fig. 5.3c, for the case of the Type 1 synthetic signal (Type1-SS), 2D Fourier spectrum barely identifies the dune frequency of $\sim$0.1 ($\lambda = 10$) but does not identify the bar frequency of $\sim$0.0025 ($\lambda = 400$) in the X-axis. In the Y-axis it does identify the bar frequency. Likewise, for the case of the Type 2 synthetic signal, Type2-SS, (Fig. 5.3f), it identifies the whole spectrum of wavelengths. This was expected for Type2-SS since, as a whole, it is more stationary than Type1-SS.

2D Morlet and Mexican Hat wavelets were applied on Type1-SS and Type2-SS. As observed in Fig. 5.4 the 2D Mexican hat wavelet coefficients defined by Eq. 5.1 provides limited information of the ripples and dunes from Type1-SS; although it improves for the bar scale. However, it performs better in retrieving information of small dunes, medium dunes and bars from Type2-SS (Fig. 5.5). This fact was expected because the Mexican hat wavelet is not efficient in detecting directions [20], even in the cases in which the anisotropic version where used (e.g. Figs. 5.4d, 5.4e, and 5.4f). The 2D Morlet wavelet is highly sensitive to the directional angle; thus for some orientations (e.g. $\theta = 0$ and $\theta = \pi/2$) it is limited in retrieving information from Type1-SS (Fig. 5.6); although, it improves for the case of Type2-SS (Fig. 5.7). At this point, neither the accuracy of the Morlet wavelet nor that of the Mexican hat wavelet has been assessed; to that aim, quantitative calibration tests are required. 2D Morlet, the Derivative of Gaussian and Mexican hat wavelets at scale $a = 1.5$ and $\theta = 0$ were used to evaluate their capabilities in retrieving the bed form features crests. Some results are presented in Figure 5.8. For this purpose the Derivative of the Gaussian wavelet performed better for the case of Type1-SS.

5.4 CONCLUSIONS

The use of two dimensional wavelets requires finding the most efficient angular, scale and sampling grid parameters. To this end, it is necessary designing benchmark signals that, to best extent, replicate bed form features (e.g. ripples, dunes and bars) in their realistic scales (e.g. ripples with wavelengths $\lambda < 0.60$m, dunes with $5 \leq \lambda \leq 200$m, and bars with $\lambda > 400$m) and following appropriate probability distributions (e.g. Gamma distribution for dunes and ripple heights). These signal should also replicate some bed form geometry singularities (e.g. crestal platforms, crestal joints and bifurcations, among others) that are commonly observed in natural environments. Subsequently, new methodologies (e.g. discrete wavelet packet transforms, adaptive modulated wavelet transforms, complex ridgelets, orthogonal quincunx wavelets with fractional orders, etc.) should be quantitative tested and, thus, their parameters calibrated.

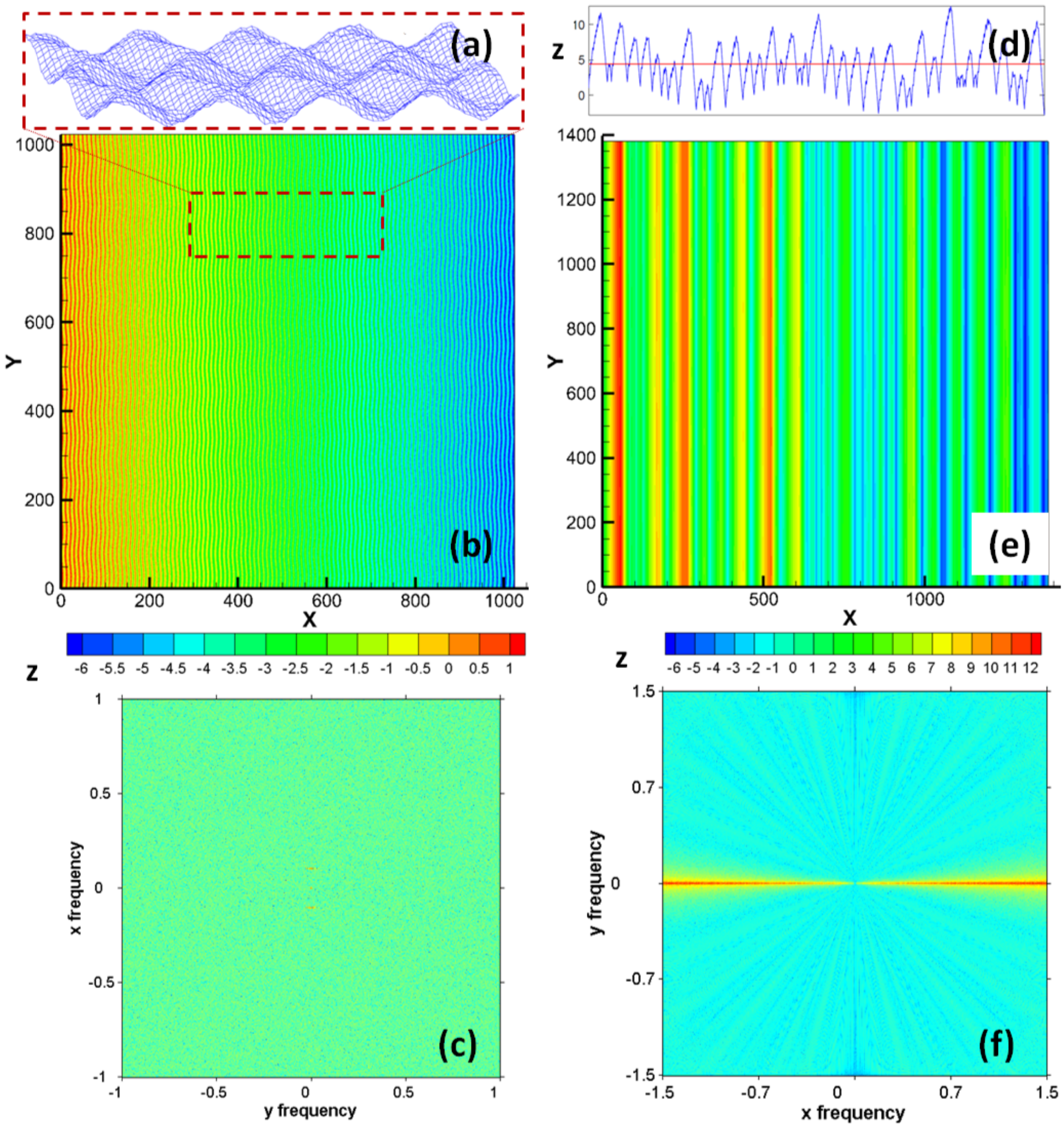

Figure 5.3: Bedform-like synthetic signals: (a) Detail of three-dimensional synthetic bed forms with uniform dune geometry superimposed over 3D bars, (b) extension of the synthetic plot, (c) 2D fast Fourier spectrum of the signal, (d) typical cross section of two-dimensional synthetic bed form plot with variable dune geometry, (e) extension of the synthetic plot, and (f) 2D fast Fourier spectrum of the signal.

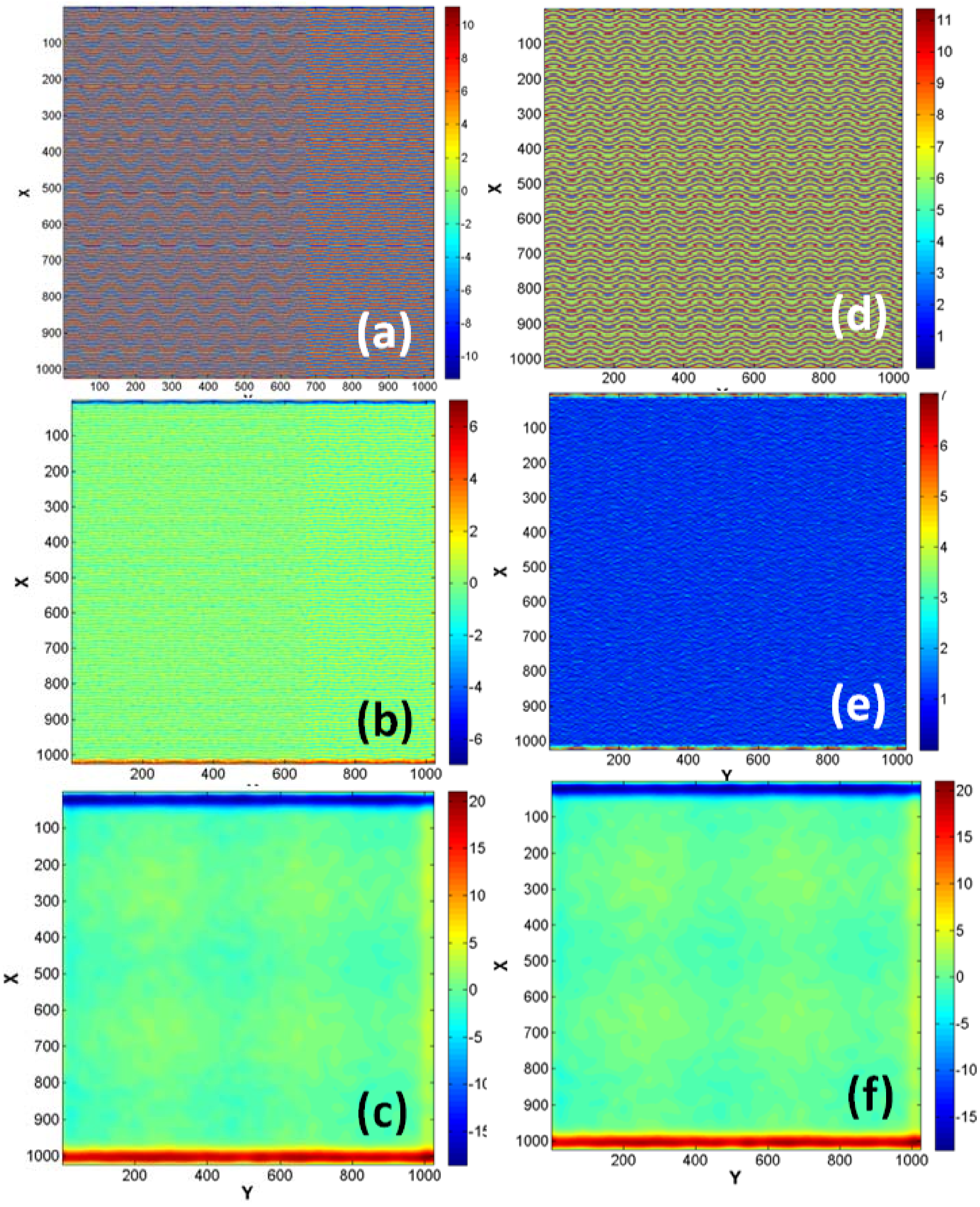

Figure 5.4: 2D Mexican Hat wavelet coefficients for Type 1 - Synthetic Signal at: (a) scale $a = 2$ and directional angle $\theta = 0$, (b) $a = 5$ and $\theta = 0$, (c) $a = 20$ and $\theta = 0$, (d) $a = 2$ and $\theta = \pi/2$, (e) $a = 5$ and $\theta = \pi/2$, and (f) $a = 20$ and $\theta = \pi/2$.

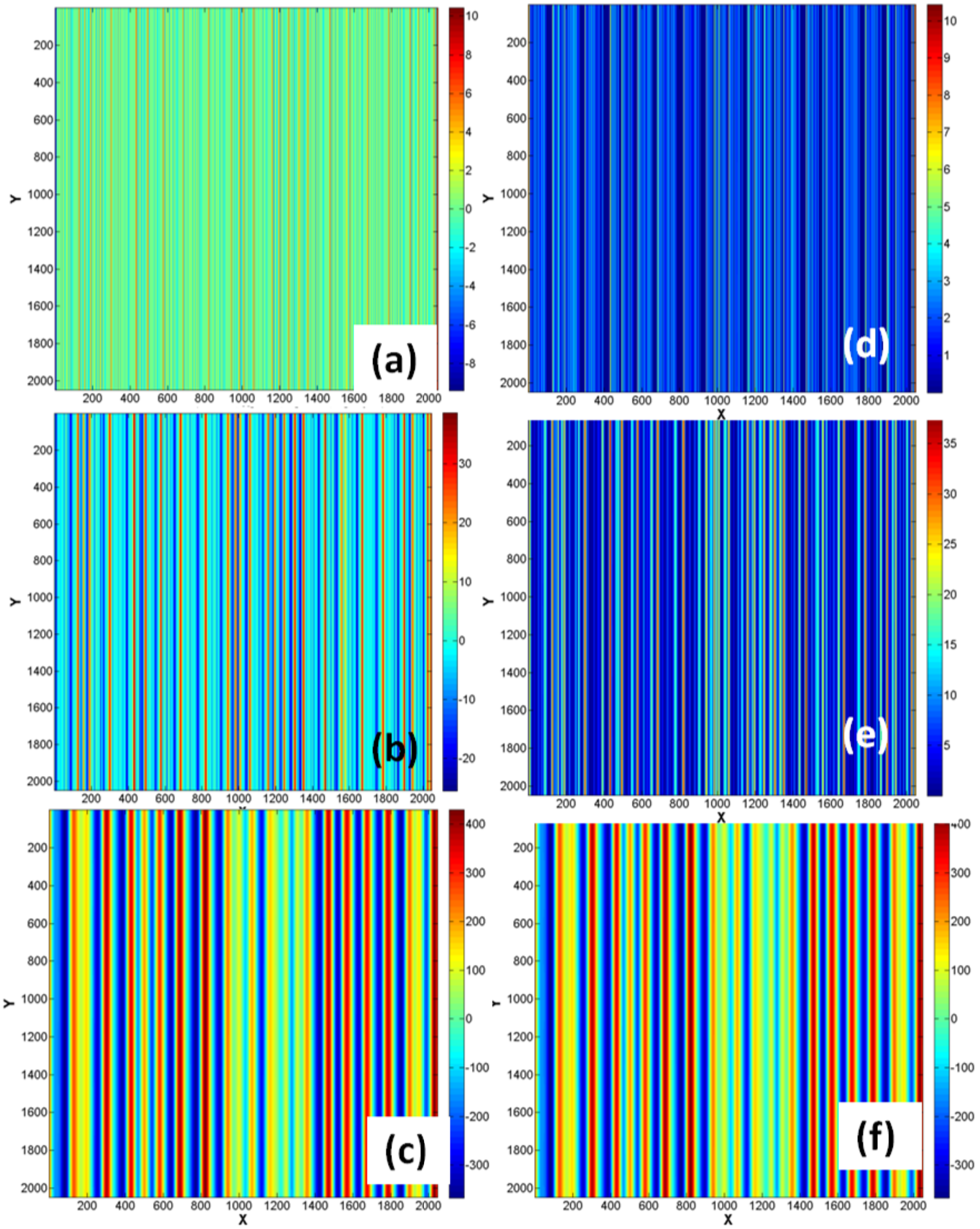

Figure 5.5: 2D Mexican Hat wavelet coefficients for Type 2 - Synthetic Signal at: (a) scale $a = 2$ and directional angle $\theta = 0$, (b) $a = 5$ and $\theta = 0$, (c) $a = 20$ and $\theta = 0$, (d) $a = 2$ and $\theta = \pi/2$, (e) $a = 5$ and $\theta = \pi/2$, and (f) $a = 20$ and $\theta = \pi/2$.

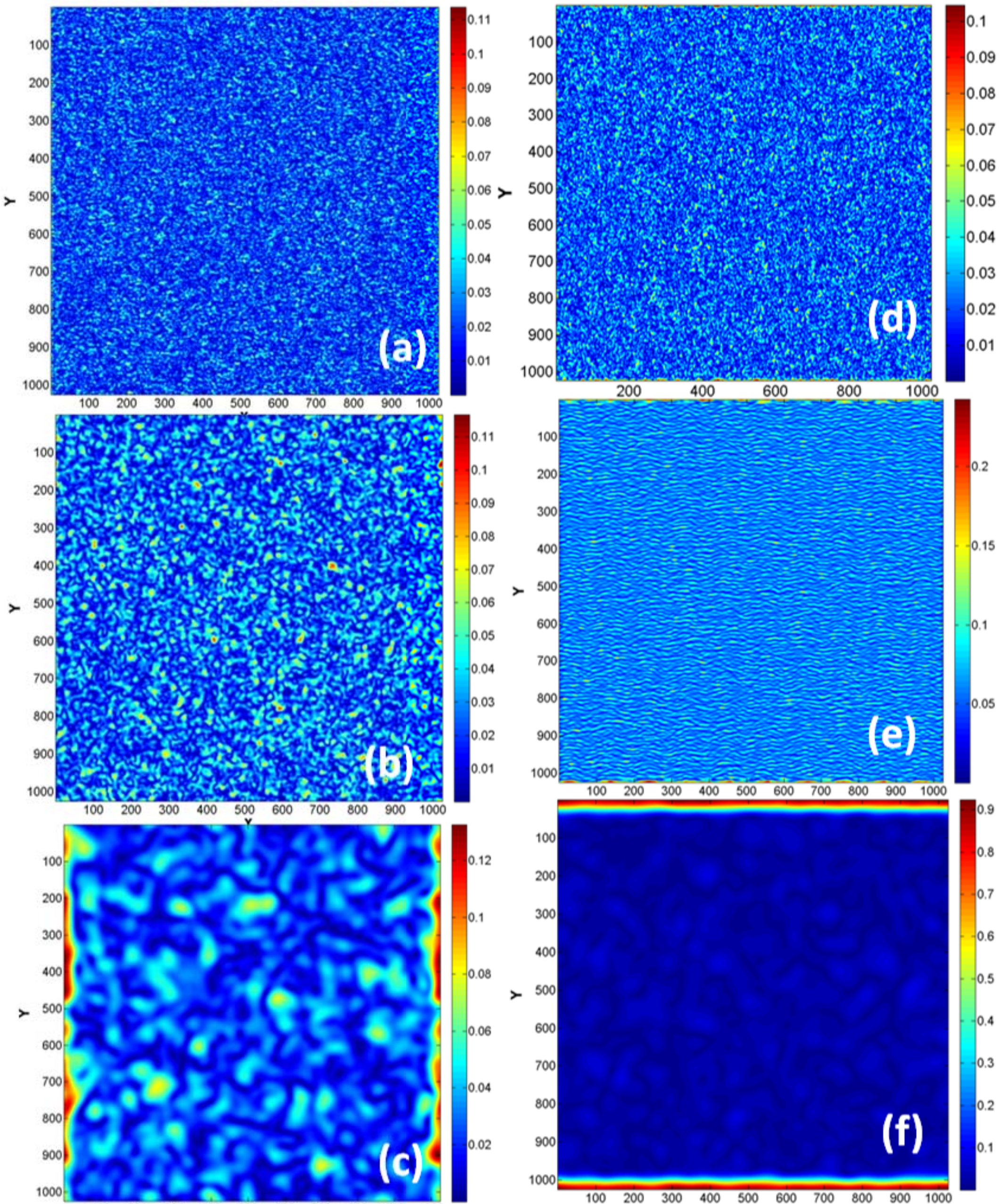

Figure 5.6: 2D Morlet wavelet coefficients for Type 1 - Synthetic Signal at: (a) scale $a = 2$ and directional angle $\theta = 0$, (b) $a = 5$ and $\theta = 0$, (c) $a = 20$ and $\theta = 0$, (d) $a = 2$ and $\theta = \pi/2$, (e) $a = 5$ and $\theta = \pi/2$, and (f) $a = 20$ and $\theta = \pi/2$.

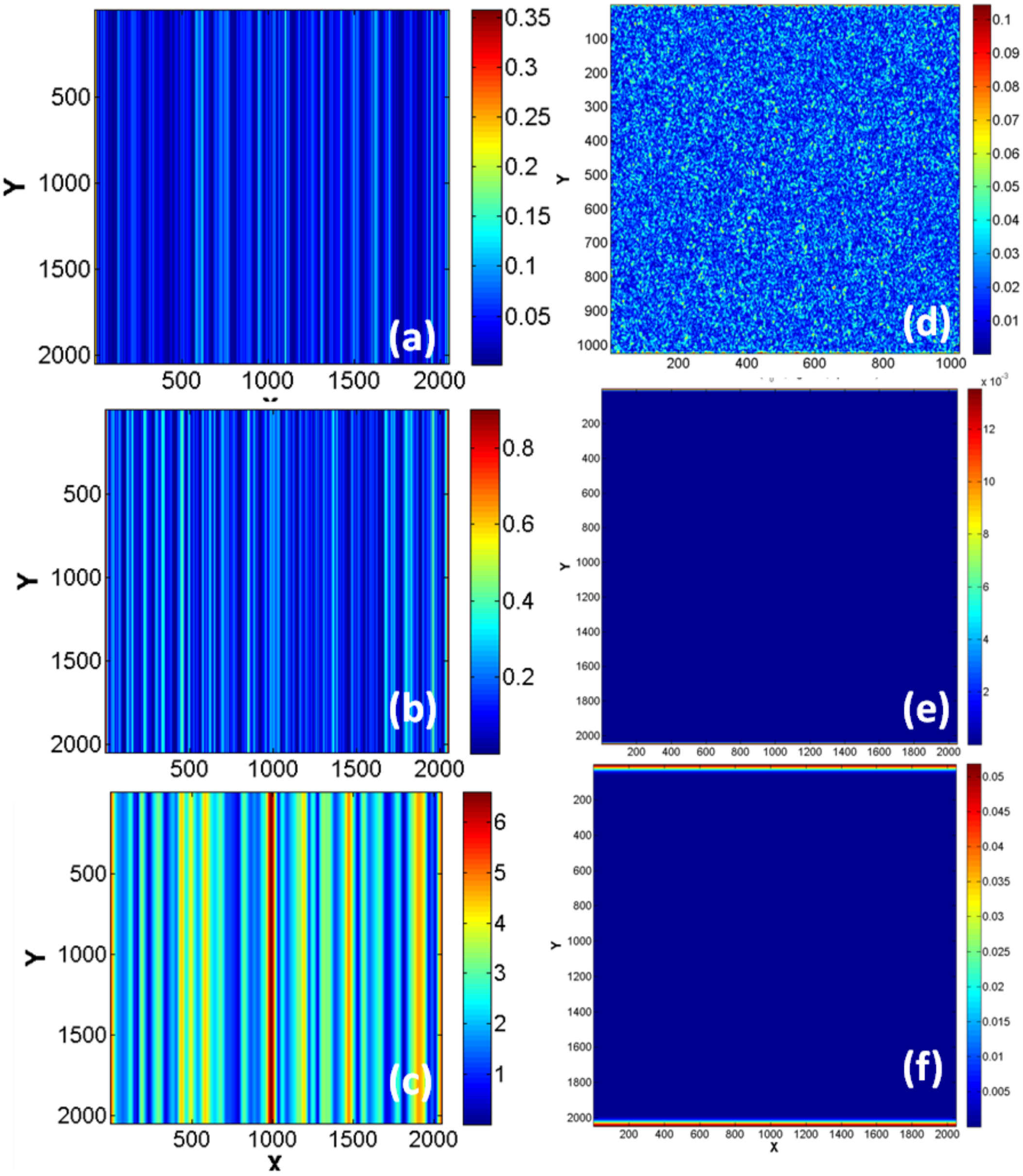

Figure 5.7: 2D Morlet wavelet coefficients for Type 2 - Synthetic Signal at: (a) scale $a = 2$ and directional angle $\theta = 0$, (b) $a = 5$ and $\theta = 0$, (c) $a = 20$ and $\theta = 0$, (d) $a = 2$ and $\theta = \pi/2$, (e) $a = 5$ and $\theta = \pi/2$, and (f) $a = 20$ and $\theta = \pi/2$.

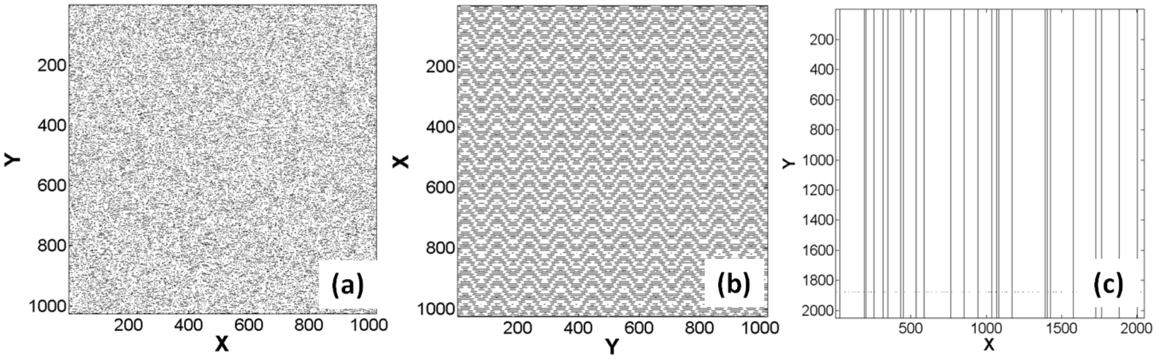

Figure 5.8: Crest lines retrieved from (a) Type 1-SS using 2D-Morlet wavelet, (b) Type 1-SS using 2D-Gauss wavelet, and (c) Type2-SS using 2D-Mexican hat wavelet.

6.0 FUTURE WORK

6.1 RIVER MORPHOMETRICS

Human activities and development continually have an impact on the environment, including waterways. Factors such as increased runoff in densely populated areas can lead to stream bank erosion and change the natural course and migration of a river. Additionally, the removal of aging dam structures necessitates reconstruction activity. Attempts to mitigate these negative impacts through restoration can be unsuccessful or have unpredictable results if not done properly. In order to properly restore a river to a more stable condition it is important to study the properties of the river, specifically the geometric properties of its planform so that an appropriate geometry can be selected [221]. The initial costs of stream restoration projects can be very high. Bulk estimates indicate that the cost of river restoration is over 129,000 us Dollars per river mile [26]. Currently there is not a tailored toolbox that could aid designers in performing statistical analysis of rivers (e.g. meandering rivers). Such tool is necessary to characterize different types of bends (Fig. 6.1), based on the orientation and number of loops and provide statistics of both bends population and individual bends (e.g. length of bend, sinuosity, and amplitude). As studied in this thesis, there is close relationship between the river centerline curvature and that of the mean center. However, there is not a clear understanding of the ranges of mean center curvature that triggers upstream-skewed bends, downstream-skewed bends, compound bends or multiple loops based on the classification of Frascati and Lanzoni, 2009 [90] shown in Fig. 6.1 for each type of meandering river based on the Brice classification scheme [47]. This would cast light in the probabilistic prediction of bend types at the vicinity of the mean center curvature singularities.

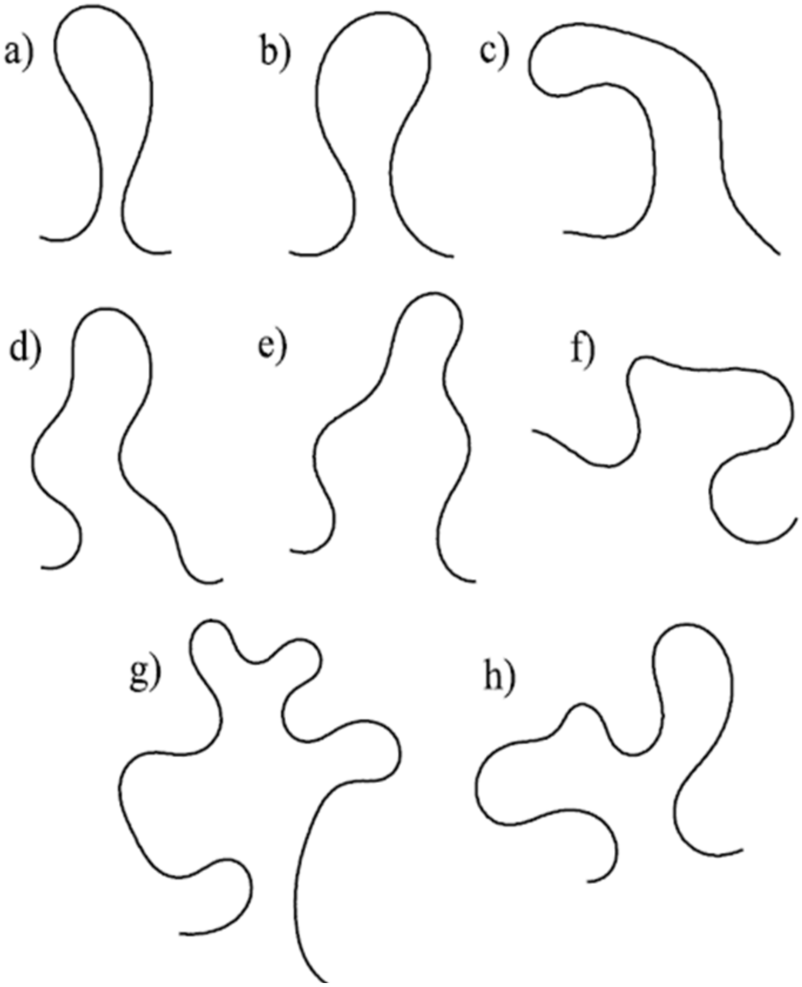

Figure 6.1: Examples of the shapes of meandering bends generated synthetically using the ZS linearized flow field (after [90]). (a) Upstream-skewed bend, (b) downstream-skewed bend, (c-f) compound bends, and (g and h) multiple loops. The flow is from left to right.

6.2 2D-WAVELET BASED ANALYSIS OF BED FORMS

6.2.1 3D Benchmark Synthetic Bed Form Signals

As highlighted in Section 5.3.1.2, the application of 2D wavelet based techniques require designing benchmark bed form synthetic signals. Some work have been performed in this matter. For instance, Rubin and Carter, 2006 [225] proposed several functions to replicate bed form geometry (Fig. 6.2); however, they do not include all the spectrum of scales (e.g. ripples, dunes, and bars) that would allow to effectively calibrate the parameters of the 2D wavelet based functions.

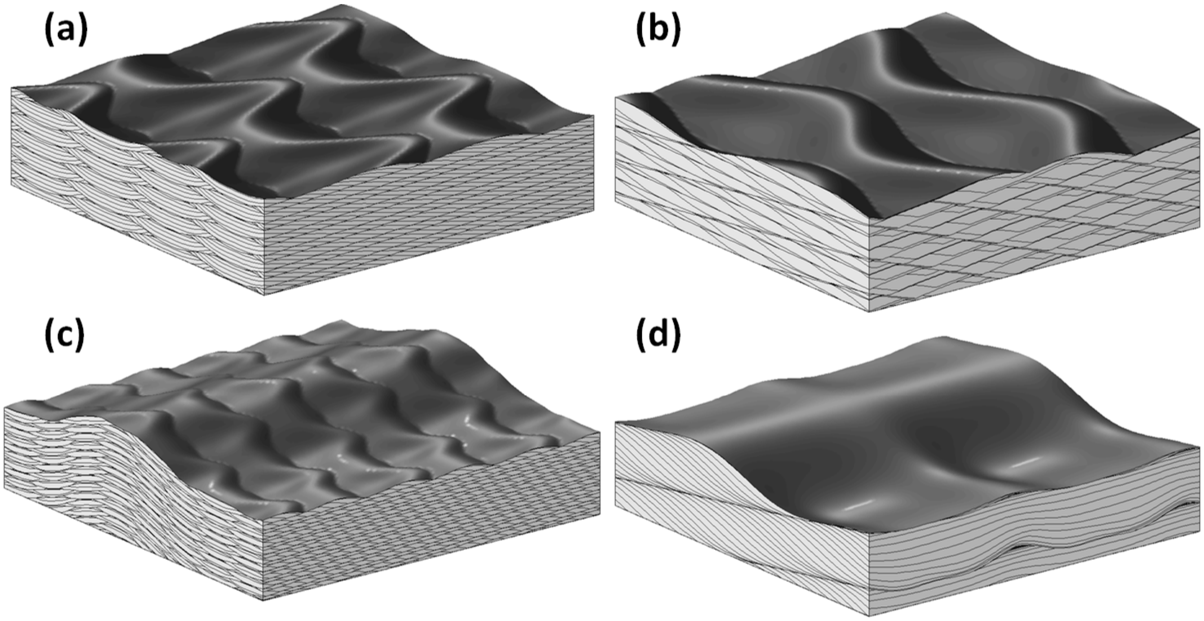

Figure 6.2: Bed form representation (after [225]) for: (a) structures formed by transverse bed forms with curved, out-of-phase crestlines and lunate plan forms: (b) bed forms with along-crest- migrating, out-of-phase sinuosities; (c) structure formed by straight-crested longitudinal bed forms with superimposed, sinuous, out-of-phase transverse bed forms ; and (d) structure formed by migrating bed forms with spurs that reverse asymmetry and migration direction but have no net along- crest displacement.

6.2.2 2D Wavelet Based Tool

A tailored 2D wavelet based tool should be designed. To this end, the following tasks should be considered:

6.2.2.1 Program Coding The programming language to code the 2D-wavelet program will be MATLAB. Many widely used 1D-wavelet programs are coded in this language. One of the most popular one, the Torrence and Compo 1D-wavelet program [243] as well as wavelet programs and studies developed by Stanford University (WAVELAB 850), Harvard University (wavdetect) used the MATLAB environment. MATLAB is a prototyping environment, meaning that it focuses on ease of development with language flexibility and interacting debugging which is limited in performance oriented languages like C++ and FORTRAN. The coding should cover the following general aspects:

1. Graphical user interface design to improve the usability of the program.
2. Functions to improve the stability under invalid or unexpected inputs.
3. Incorporate the latest methodologies (i.e. complex ridgelets, dual-tree complex wavelet transforms) in the analysis river bedforms. For comparison purposes continuous and discrete 2D-Wavelet transform functions such as Morlet wavelet and B-spline wavelets studied by Chui, 1992 ([64]) would be included.
4. Riverbed morphology retrieval functions to estimate predominant wavelength, amplitude and slope of ripples and dunes and describe the orientation of dominant bifurcations.
5. Statistical framework functions to estimate 2D-wavelet means and variances in the physical and Fourier space and bicoherence analysis.
6. Output data functions.

6.2.2.2 Program Testing A functional test to verify specific actions or functions of the code would be carried out at certain benchmarks through the program development in order to minimize the fixing cost. Likewise, the compatibility and stability of the program should also be checked. The program would be validated by using synthetic and collected data (e.g. bed form data from the Parana River and the Amazon River). The benchmark synthetic data would be used to test the program under different conditions of sampling frequency, stationarity, signal-to-noise ratios and topographical singularities (e.g. stepped relief changes). Likewise, riverbed and laboratory collected data would also be used to test the program.

6.2.3 Field Data from the Amazon River

Latrubesse et al., 2005 ([150]) have underlined the relatively limited knowledge available on tropical rivers. It is particularly true in the upper Amazonian floodplains (area that occupies Bolivia and Peru), where very little is known concerning fluvial dynamics, except on the middle and lower Amazon river (area that occupies Brazil). Bathymetric data of the Amazon River was collected in May 2012 by using a Multibeam Echosounder at 12 study plots located in the main and secondary channels of the Amazon River (Figure 6.3).

The data analysis for the Amazon river would be carried out by using the aforementioned 2D wavelet based toolbox. The statistics of the bedform at different scales will be compared for the main and secondary channels for confluence and diffluence cases. This characterization of 3D bedforms for the case of anabranching channels will be the first scientific outcome correlating anabraching structures with development of bedforms.

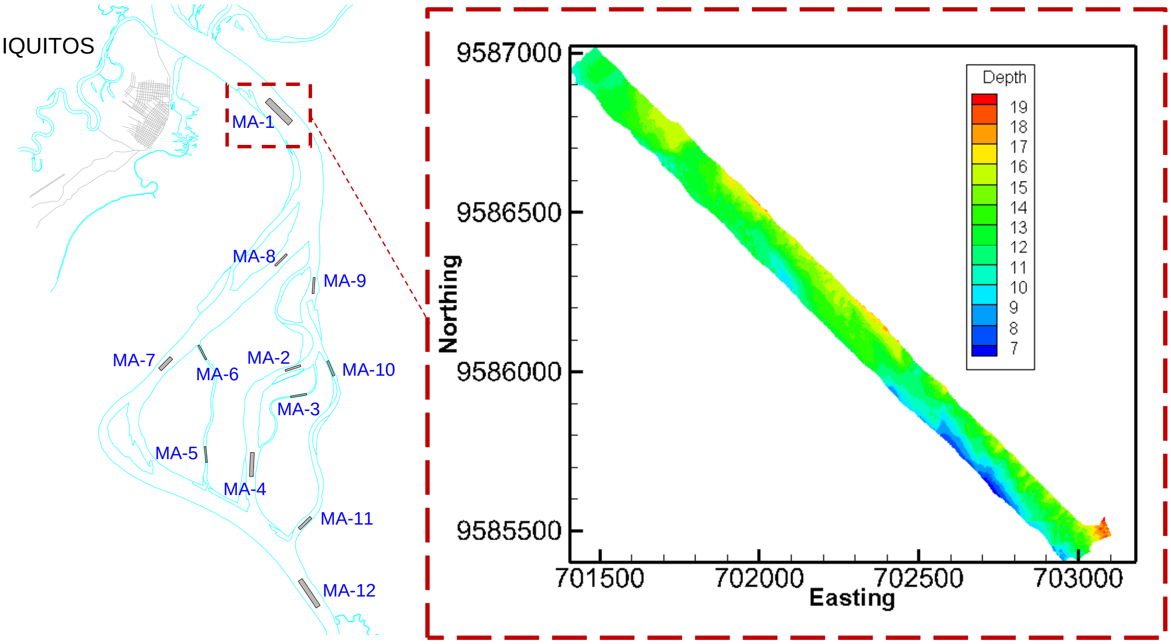

Figure 6.3: Study plots located in the main and secondary channels of the Amazon River [4, 3]. These plots are tipically 1-2 km length and 100-200 m width. The survey was carried out in July 2012 using mutibeam echosound, in coordination with the Peruvian Navy.

6.3 CORRELATION BETWEEN MORPHODYNAMIC AND HYDRODYNAMIC SIGNALS

There is a hydraulic transitional region (response lag of the flow structure to local curvature) that occurs just upstream of the bend apex (near the inflexion point upstream of a bend apex) for an upstream and downstream oriented bend [10]. Likewise, experimental work performed under flat smooth bed condition in a periodic, asymmetric, Kinoshita meandering channel [11] showed that: [1] for the case of bends oriented upstream valley, the bed forms are produced just upstream of the bend apex, whereas for the case of bends oriented downstream valley they are observed around the upstream inflection point, and [2] the downstream-skewed condition produces the deepest scour region, which is located downstream of the bend apex. To date; however, neither the spatial correlation between bed form, planform and bank form signals nor the correlation between the morphodynamic and hydrodynamic signals have been studied.

2D wavelet based tools have the potential to quantify river hydrodynamic and morphodynamic structures, and their interrelationship, without making a two-dimensional simplification of the phenomena.

7.0 CONCLUSIONS

The following conclusion are drawn:

- As part of the study of morophodynamic signals, a methodology that combines the capabilities of signal processing techniques (e.g. one dimensional continuous wavelet transforms and a robust spline filter) was developed to discriminate waves with different periodicities in bed form profiles.
- The application of one dimensional continuous and discrete wavelets, principal component analysis and the Frechét distance has allowed to define the mean center of meandering rivers. The mean center represents a robust reference to analyze river meandering parameters for middle-term horizons (e.g. 10-∼30 years). These techniques have also proved to be effective in the development of a universal river classification system that could complement the prevailing observational Brice classification scheme.
- To the best of my knowledge this thesis has addressed for the first time the study of meandering rivers confluences in the Upper Amazon catchment. The wavelet analysis has allowed to identify and quantify based on planimetric configurations of the main, tributary and downstream main channel the following confluence features: [1] modulation of the morphodynamics of the upstream main and tributary channels and [2] modulation of the morphodynamics of the downstream main channel imposing arc-wavelength and amplitude increments and resembling a constructive effect in the superposition of curvature waves.
- The capabilities of the 2D wavelet based tools have not been fully used in the analysis of three dimensional bed form data. The use of two dimensional wavelets requires finding the most efficient angular, scale and sampling grid parameters. To this end, it is neces-

sary designing benchmark signals that fully represent the configurations that commonly observed in natural environments (e.g. crestal platforms, crestal joints and bifurcations, etc.)

APPENDIX

RONALD R. GUTIERREZ BIO

A.1 ACADEMIC TRAINING

1. B.S., National University of Engineering, Lima, PERU, December 1997, Department of Civil Engineering.
2. Diplomate Designation in Project Management, Peruvian University of Applied Sciences, Lima, Peru, April, 2009, School of Postgraduate Studies.
3. M.S., University of Pittsburgh, Pittsburgh, Pennsylvania, June 2012, Department of Civil and Environmental Engineering.

A.2 PROFESSIONAL SOCIETY MEMBERSHIPS

1. American Society of Civil Engineers.
2. American Geophysical Union.
3. American Statistical Association.
4. Geological Society of America.
5. International Association for Hydro-Environment Engineering and Research (President of the student chapter of the University of Pittsburgh).

A.3 AWARDS AND HONORS

1. Graduate honoree student (University of Pittsburgh, 2013) invited to the 2013 Honors convocation of the University of Pittsburgh.
2. Freeman fellowship (American Society of Civil Engineers, 2012) to carry out bathymetry (using a multibeam echo sounder) and velocity measurements (using ADCP) in the Amazon River.
3. Student travel grant (American Geophysical Union, 2011) to give an oral presentation in the AGU Fall Meeting 2011. San Francisco, USA.
4. International Student Fund Scholarship (Center for International Studies of the University of Pittsburgh, 2010) to carry out a one-month preliminary field work in the Amazon River, Peru.
5. Student scholarship (International Erosion Control Association, 2001) to attend the 33rd Annual IECA Conference and Trade Exposition in Orlando, Florida.
6. B.S. Thesis (National University of Engineering, 2000) approved with the highest level of merit based on the Peruvian grading system.

A.4 JOURNAL PUBLICATIONS

1. Gutierrez, R. R., Abad J. D., Parsons, D. R., Best J. L. (2013). Discrimination of bed form scales using robust spline filter and wavelets transforms: methods and application to synthetic signals and the Parana River, Argentina, Journal of Geophysical Research-Earth Surface (accepted with minor text revision).
2. Gutierrez, R. R. and Abad J. D. (2013). Planform Characterization of Meandering Rivers by Using Wavelet Transforms, Principal Component Analysis and Frecht Distance, Water Resources Research, AGU (in final revision).
3. Gutierrez, R. R., Choi, M., and Abad J. D. (2013). Characterization of confluences of free meander trains at the Upper Amazon Basin, in revision for Sedimentary Geology.

4. Gutierrez, R. R., Abad J. D., Parsons, D. R., Best J. L. (2013). Discrimination of bed form scales using robust spline filter and wavelets transforms, in preparation for Computers and Geosciences.
5. Gutierrez, R. R. and Abad J. D. (2013). Discrimination and analysis of bed form scales using 3D synthetic signals and two-dimensional wavelets, in preparation, Journal of Hydraulic Research.

A.5 CONFERENCE PROCEEDINGS AND ABSTRACTS

1. Gutierrez, R. R., Choi, M., and Abad, J. D. (2013). Dynamics of meander train confluences, 8th Symposium on River, Coastal and Estuarine Morphodynamics, RCEM 2013. Cantabria, Spain, June.
2. Gutierrez, R. R. and Abad, J. D. (2013). Conservation of meander dynamics, from cutoff to migration processes, 8th Symposium on River, Coastal and Estuarine Morphodynamics, RCEM 2013. Cantabria, Spain, June.
3. Gutierrez, R. R., Abad, J. D. , Parsons and J. Best (2013). Characterization of bedforms, application to the Parana River, 8th Symposium on River, Coastal and Estuarine Morphodynamics, RCEM 2013. Cantabria, Spain, June.
4. Gutierrez, R. R. and Abad, J. D. (2012). Statistical analysis of meandering rivers using wavelet transforms and principal component analysis, American Geophysical Union (AGU), Fall Meeting 2012, San Francisco, USA, November. Poster presentation.
5. Gutierrez, R. R. and Abad J. D. (2012). Statistical analysis of meandering rivers using wavelet transforms and principal component analysis, Tropical Rivers Conference, Iquitos, Peru, August.
6. Abad, J. D., Peralta, B., Paredes, J., Frias, C., Gutierrez, R., Montoro, H. (2012). The meandering Ucayali River, a cyclic adaptation of cutoff and planform migration. River Flow 2012. September 5-7, San Jose, Costa Rica.
7. Gutierrez, R. R. Abad, J. D., Parsons, D., Best, J. (2011). Discrimination of bed form scales using robust spline filter and wavelet transforms: methods and application to syn-

thetic signals and the Parana River, Argentina. AGU Fall Meeting 2011, San Francisco, USA, November. Oral presentation.

8. Gutierrez, R. R. Abad, J. D., Parsons, D., Best, J., Orfeo (2011). 1D-wavelets to the study of bed morphology in large river systems. ASCE EWRI conference, Palm Springs, California, USA.
9. Gutierrez, R. R., Abad, J. D., Parsons, D., Best, J., Orfeo (2011). Wavelets application to study the bed forms of the Parana River, XXXIV International Association of Hydraulics Engineering and Research Congress, Brisbane, Australia.
10. Abad, J. D., Gutierrez, R. R., Guneralp, I. (2010). Analysis of bend migration patterns of meandering channels using Wavelets. 2010 Annual Meeting, Association of American Geographers, Washington, DC, USA. April 14-18.
11. Gutierrez R. R., Abad, J. D., Parsons D., Best, J., Orfeo, O. (2010). Aplicacion de wavelets en el estudio de formas de fondo del Rio Parana, XXIV Latin American Congress in Hydraulics, Punta del Este, Uruguay, November.
12. Gutierrez, R. R., Abad, J. D. (2010). Aplicacin de Wavelets en el estudio de ros meandrcos. 2do Congreso Nacional del Agua, National University of Engineering, Lima, PERU, April 7-9. In Spanish.
13. Gutierrez R. R. and Mansen A. (2005). Bioingenieria para el control de la erosion (Bioengineering application in erosion control), XV Peruvian Civil Engineering Congress, Ayacucho, Peru, November.

A.6 TECHNICAL REPORTS

1. Gutierrez R. R., Allende T., Zedano J., Carranza J. and Ayala M. (2009). Study of Hazard Assessment of Barranca, Pativilca and Paramonga. Report to the United Nations Development Program - Peruvian Agency of Civil Defense.
2. Gutierrez R. R. and Abad J. D. (2012). Statistical Analysis of Meanders of the Red River and Its Tributaries. Report to Barr Engineering Co. for the US Army Corps of Engineers.

BIBLIOGRAPHY

[1] J. D. Abad and M. H. Garcia. RVR meander: A toolbox for re-meandering of channelized streams. *Computers and Geosciences*, 32:92–101, 2006.

[2] J. D. Abad and M. H. Garcia. Experiments in a high-amplitude kinoshita meandering channel. 2: Implications of bend orientation on bed morphodynamics. *Water Resources Research*, 2009.

[3] J. D. Abad and H. Montoro. Anabranching structures in the upper amazon river, quasi-freely and non-developed meanders. *In submission*, 2013.

[4] J. D. Abad, J. Paredes, and H. Montoro. Similarities and differences between a large meandering river and an anabranching river: the ucayali and amazon river cases. *AGU Fall Meeting, San Francisco, USA*, 2010.

[5] J. D. Abad, B. Peralta, J. Paredes, C. Frias, R. Gutierrez, and H. Montoro. The meandering ucayali river, a cyclic adaptation of cutoff and planform migration. *River Flow 2012. September 5-7, San Jose, Costa Rica*, 2012.

[6] Jorge D. Abad. *Hydrodynamics and morphodynamics in Kinoshita Meandering Channels*. PhD thesis, Department of Civil and Environmental Engineering, University of Illinois at Urbana-Champaign, Illinois, USA, 2008.

[7] Jorge D. Abad. Planform dynamics of meandering channelss based on wavelet analysis. In *AGU Fall Meeting, San Francisco, USA*, 2009.

[8] Jorge D. Abad. Planform dynamics of meandering channelss based on wavelet analysis. In *AGU Fall Meeting, San Francisco, USA*, 2009.

[9] Jorge D. Abad and M. H. Garcia. RVR Meander: A toolbox for re-meandering of channelized streams. *Computers and Geosciences*, 32:92–101, 2006. doi: 10.1016/j.cageo.2005.05.006.

[10] Jorge D. Abad and Marcelo H. Garcia. Experiments in a high-amplitude Kinoshita meandering channel: 1. Implications of bend orientation on mean and turbulent flow structure. *Water Resour. Res.*, 45, 2009. doi: 10.1029/2008WR007017.

[11] Jorge D. Abad and Marcelo H. Garcia. Experiments in a high-amplitude Kinoshita meandering channel: 2. Implications of bend orientation on bed morphodynamics. *Water Resour. Res.*, 45:1–14, 2009. doi: 10.1029/2008WR007017.

[12] Jorge D. Abad, Octavio E. Sequeiros, Benoit Spinewine, Carlos Pirmez, Marcelo H. Garcia, and Gary Parker. Secondary current of saline underflow in a highly meandering channel: Experiments and theory. *Journal of Sedimentary Research*, 81:787–813, 2011.

[13] J Aberle, V. Nikora, M. Henning, B. Ettmer, and B Hentschel. Statistical characterization of bed roughness due to bed forms: a field study in the Elbe River at Aken, Germany. *Water Resour. Res.*, 46, 2010. doi: 10.1029/2008WR007406.

[14] Paul Addisson. *The illustrated wavelet transform handbook.* Institute of Physics Publishing Bristol and Philadelphia, United Kingdom, 2004.

[15] John R. L. Allen. *Sedimentary structures: their character and physical basis. Volume I.* Elsevier Scientific Publishing Company, The Netherlands, 1982.

[16] Dulan Amarasinghea, Upul Sonnadara, Marcus Bergb, and Vernon Cooray. Channel tortuosity of long laboratory sparks. *Journal of Electrostatics*, 65(8):521–526, 2007.

[17] Mina Aminghafari, Nathalie Cheze, and Jean-Michel Poggi. Least meadian of squares regression. *Computational Statistics and Data Analysis*, 50:2381–2398, 2006.

[18] Mario L. Amsler and Marcelo H. Garcia. Discussion: Sand-dune geometry of large rivers during floods. *Journal of Hydraulic Engineering*, 123:582–585, June 1997.

[19] V. S. Shastri Annambhotla, William W. Sayre, and Robert H. Livesey. Statistical properties of Missouri River bed forms. *Journal of the Waterways, Harbors and Coastal Engineering Division*, 98(4):489–510, November 1972.

[20] J. Antonie, R. Murenzi, P. Vandergheynst, and S. Twareque. *Two-dimensional wavelets and their relatives.* Cambridge University Press, United Kingdom, 2004.

[21] Gail M. Ashley. Classification of large-scale subaqueous bedforms: a new look at an old problem. *J. Sediment. Petrol.*, 60(1):160–172, January 1990.

[22] Peter Ashmore and Gary Parker. Confluence scour in coarse braided streams. *Water Resources Research*, 19(2):392–402, 1983.

[23] Serap Aydn, Hamdi Melih Saraoglu, and Sadk Kara. Log energy entropy-based eeg classification with multilayer neural networks in seizure. *Annals of Biomedical Engineering*, 37(12):2626–2630, 2009. DOI: 10.1007/s10439-009-9795-x.

[24] A. C. W. Baas. Wavelet power spectra of aeolian sand transport by boundary layer turbulence. *Geophysical Research Letters*, 33, 2006. doi:10.1029/2005GL025547.

[25] Jaco A. Baas. An empirical model for the development and equilibrium morphology of current ripples in fine sand. *Sedimentology*, 46:123–138, 1999.

[26] Brian Bair. Streambank stabilization, streambank fencing, nuisance species control, riparian zone management. In *Salmon Habitat Restoration Cost Workshop*, Gladstone, OR, USA, 2004. NOA Pacific States Marine Fisheries Commission.

[27] Bhavik R. Bakshi. Multiscale pca with application to multivariate statistical process monitoring. *AIChE Journal*, 44(7):1596–1610, 1998.

[28] N. J. Balmforth and C. Piccolo. The onset of meandering in a barotropic jet. *Jornal of Fluid Mechanics*, 449:85–114, 2001.

[29] S. Baulinas. Time scales and trends in the central england temperature data (1659 1990): A wavelet analysis. *Geophys. Res. Lett.*, 24:1351–1354, 1997. doi:10.1029/97GL01184.

[30] Lee Benda, Leroy Poff, Daniel Miller, Thomas Dunne, Gordon Reeves, George Pess, and Michael Pollock. The network dynamics hypothesis: how channel networks structure riverine habitats. *Bioscience*, 5(5):413–427, 2004.

[31] S. J. Bennett and J. L. Best. Mean flow and turbulence structure over fixed ripples and the ripple-dune transition. In *Coherent Flow Structures in Open Channels, edited by P. J. Ashworth et al.*, number 281-304. John Wiley, 1996.

[32] J. L. Best. The morphology of river channel confluences. *Progress in Physical Geography*, 10:157–174, 1986.

[33] J. L. Best. The fluid dynamics of small-scale alluvial bedforms. In *Advances in Fluvial Dynamics and Stratigraphy, edited by P. A. Carling and M. R. Dawson*, number 67-125. John Wiley and Sons, 1996.

[34] James L. Best. Sediment transport and bed morphology at river channel confluences. *Sedimentology*, 35:481–498, 1988.

[35] Jim Best. The fluid dynamics of river dunes: A review and some future research directions. *J. Geophys. Res.*, 110, 2005. doi:10.1029/2004JF000218.

[36] Jim Best. Kinematics, topology and significance of dune-related macroturbulence: some observations from the laboratory and field. In *Fluvial Sedimentology VII*, number 35, pages 41–60, Oxford, UK, 2005. Blackwell Publishing Ltd.

[37] Jim Best and A. Robert. Discussion of "Transition from Ripples to Dunes" by A.J. Raudkivi. *Journal of Hydraulic Engineering*, 132(12):1316–1320, 2006.

[38] Pascale M. Biron, James L. Best, and Andre G. Roy. Effects of bed discordance on flow dynamics at open channel confluences. *Journal of Hydraulic Engineering*, 122(12):676–682, 1996.

[39] Pascale M. Biron, Antonie Richer, Alistair Kirkbride, Andre G. Roy, and Sangsoo Han. Spatial patterns of water surface topography at a river confluence. *Earth Processes and Landforms*, 27:913–928, 2002.

[40] Astrid Blom and Maarten G. Kleinhans. Estimating bed form height from sorting preserved in sedimentary records of river dunes, deltas and bars. In *5th IAHR Symposium on River, Coastal and Estuarine Morphodynamics*, pages 641–648, Enschede, NL, September 2007. International Association of Hydro-Environment Research.

[41] Astrid Blom and Gary Parker. Vertical sorting and the morphodynamics of bed form-dominated rivers: a modeling framework. *J. Geophys. Res.*, 109, 2004. doi:10.1029/2006JF000618.

[42] P. Blondeaux and G. Seminara. A unified bar-bend theory of river meanders. *Journal of Fluid Mechanics*, 157:449–470, 1985.

[43] Claudine Boyer, Andre G. Roy, and James L. Best. Dynamics of a river channel confluence with discordant beds: Flow turbulence, bed load sediment transport, and bed morphology. *Journal of Geophysical Research*, 111, 2006. doi:10.1029/2005JF000458.

[44] K. F. Bradbook, S. N. Lane, and K. S. Richards. Numerical simulation of three-dimensional, time-averaged flow structure at river channel confluences. *Water Resources Research*, 36(9):2731–2746, 2000.

[45] K. F. Bradbrook, S. N. Lane, K. S. Richards, P. M. Biron, and A. G. Roy. Large eddy simulation of periodic flow characteristics at river channel confluences. *Journal of Hydraulic Research*, 38(3):207–215, 2000.

[46] K. F. Bradbrook, S. N. Lane, K. S. Richards, P. M. Biron, and A. G. Roy. Role of bed discordance at symmetrical river confluences. *Journal of Hydraulic Engineering*, 127(5):351–368, 2001.

[47] J. C. Brice. Air photo interpretation of the form and behaviour of alluvial rivers. final report. Technical report, Final report to the US Army Research Office, 1975.

[48] W. B. M. Ten Brinke, A. W. E. Wilbers, and C. Wesseling. Dune growth, decay and migration rates during a large-magnitude flood at a sand and mixed sand-gravel bed in the Dutch Rhine river system. In *Fluvial Sedimentology VI*, number 28, pages 15–32, Oxford, UK, 1999. Blackwell Publishing Ltd.

[49] R. Bruinsma. The statistical mechanics of meandering. *Journal de Physique*, 51:829–845, 1990.

[50] Carlo Camporeale and Luca Ridolfi. Interplay among river meandering, discharge stochasticity and riparian vegetation. *Journal of Hydrology*, 382:138–144, 2010.

[51] M. Bayani Cardenas. Stream-aquifer interactions and hyporheic exchange in gaining and losing sinuous streams. *Water Resources Research*, 45:1–13, 2009.

[52] M. Bayani Cardenas. Stream-aquifer interactions and hyporheic exchange in gaining and losing sinuous streams. *Water Resources Research*, 45:1–13, 2009.

[53] M. Bayani Cardenas and J. L. Wilson. The influence of ambient groundwater discharge on exchange zones induced by currentbedform interactions. *Journal of Hydrology*, 331:103–109, 2006.

[54] M. Bayani Cardenas, J. L. Wilson, and V. A. Zlotnik. Impact of heterogeneity, bed forms, and stream curvature on subchannel hyporheic exchange. *Water Resour. Res.*, 40, 2004. doi: 10.1029/2004WR003008.

[55] M. Bayani Cardenas, J. L. Wilson, and V. A. Zlotnik. Hydrodynamics of coupled flow above and below a sediment-water interface with triangular bedforms. *Adv. Water Resour.*, 30:301–313, 2007.

[56] Chris J. Carey, Tony G. Brown, Keith C. Challis, J. Howard, and Lyden Cooper. Predictive modelling of multiperiod geoarchaeological resources at a river confluence: a case study from the Trent-Soar,UK. *Archaeological Prospection*, 13:241–250, 2006.

[57] Philippe Castigliola and J. Garcia Castellanos. Process capability indices dedicated to bivariate non normal distributions. *Journal of Quality in Maintenance Engineering*, 14:87–101, 2008.

[58] Y. Catano-Lopera, J. D. Abad, and M. H. Garcia. Characterization of bedform morphology generated under combined flows and currents using wavelet analysis. *Ocean Eng.*, 36:617–632, July 2009.

[59] Turgay Celik and Tardi Tjahjadi. Multiscale texture classification using dual-tree complex wavelet transform. *Pattern Recognition Letters*, 30:331–339, 2009.

[60] T. P. Chang and G. H. Toebes. A statistical comparison of meander planforms in the wabash basin. *Water Resources Research*, 6:557–578, 1970. doi:10.1029/WR006i002p00557.

[61] Tianhorng Chang and C.-C. Jay Kuo. Texture analysis and classification with tree-structured wavelet transform. *Transactions on Image Processing*, 2(4):429–441, 1993.

[62] F. Charru and E. J. Hinch. Ripple formation on a particle bed sheared by a viscous liquid. Part 1. Steady flow. *Journal of Hydraulic Research*, 550:111–121, 2006.

[63] S. V. Chitale. Theories and relationship of river channel patterns. *Journal of Hydrology*, 19(4):285–308, 1973. http://dx.doi.org/10.1016/0022-1694(73)90104-2.

[64] Charles Chui. *An introduction to wavelets.* Academic Press, San Diego, California, USA, 1992.

[65] S. E. Coleman and V. I. Nikora. Fluvial dunes: initiation, characterization, flow structure. *Earth Surf. Processes Landforms*, 36:39–57, 2011.

[66] Stephen E. Coleman and Burkhard Eling. Sand wavelets in laminar open-channel flows. *Journal of Hydraulic Research*, 38(5):331–338, 2000.

[67] M. Colombini and A. Stocchino. Ripple and dune formation in rivers. *J. Fluid Mech.*, 673:121–131, 2011.

[68] George Constantinescu, Shinjiro Miyawaki, Bruce Rhoads, Alexander Sukhodolov, and Gokhan Kirkil. Structure of turbulent flow at a river confluence with momentum and velocity ratios close to 1: Insight provided by an eddy-resolving numerical simulation. *Water Resources Research*, 47, 2011. doi: 10.1029/2010WR010018.

[69] O. T. Coomes, C. Abizaid, and M. Lapointe. Human modification of a large meandering amazonian river: genesis, ecological and economic consequences of the masisea cutoff of the central ucayali, peru. *Journal of the Human Environment*, 38(3):130–134, 2009.

[70] Ransome K. T. Corney, Jeffrey Peakall, Daniel R. Parsons, Lionel Elliott, Kathryn J. Amos, James L. Best, Gareth M. Keevil, and Derek B. Ingham. The orientation of helical flow in curved channels. *Sedimentology*, 53:249–257, 2006.

[71] Subhendu Das, Nirode Mohanty, and Avtar Singh. Is the nyquist rate enough? In *2008 3rd International Conference on Digital Telecommunications (ICDT)*, pages 27–32. Institute of Electrical and Electronics Engineers (IEEE), Institute of Electrical and Electronics Engineers (IEEE), 2008.

[72] T. R. Davies and C. C. Tinker. Fundamental characteristics of stream meanders. *Geological Society of America Bulletin*, 95(5):1173–1192, 1984.

[73] Olivier Devauchelle, Alexander P. Petroff, E. Lobkovsky, and Daniel H. Rothman. Longitudinal profile of channels cut by springs. *Journal of Fluid Mechanics*, 667:38–47, 2011. doi:10.1017/S0022112010005264.

[74] Olivier Devauchelle, Alexander P. Petroff, Hansjorg F. Seybold, and Daniel H. Rothman. Ramification of stream networks. *Proceedings of the National Academy of Sciences*, 109(51):20832–20836, 2012. doi: 10.1073/pnas.1215218109.

[75] Yadolah Dodge. *The concise encyclopedia of statistics.* Springer, New York, USA, 2008.

[76] Jeff Dozier. An examination of the variance minimization tendencies of a supraglacial stream. *Journal of Hydrology*, 31:359–380, 1976.

[77] Anne Driemel, Sariel Har-Peled, and Carola Wenk. Approximating the Frechet distance for realistic curves in near linear time. *Discrete Computational Geometry*, 48:94–127, 2012.

[78] William W. Duncan, Geoffrey C. Poole, and Judith L. Meyer. Large channel confluences influence geomorphic heterogeneity of a southeastern United States river. *Water Resources Research*, 45, 2009. doi: 10.1029/2008WR007454.

[79] U. Ehret and E. Zehe. Series distance an intuitive metric to quantify hydrograph similarity in terms of occurrence, amplitude and timing of hydrological events. *Hydrology and Earth System Sciences*, 15(3):877–896, 2011.

[80] M. Elhakeem and J. Imran. A bedload model for uniform sediment derived from the movement of bedforms. In *River, Coastal and Estuarine Morphodynamics: RCEM 2005*, pages 853–860. Taylor and Francis Group, London, 2006.

[81] M. A. K. Elsayed. Wave parameters and functions in wavelet analysis. *Ocean Engineering Journal*, 31:111–125, 2004.

[82] Mohamed A. K. Elsayed. Wavelet bicoherence analysis of windwave interaction. *Ocean Eng.*, 33:458–470, 2006.

[83] Frank Engelund and Jorgen Fredsøe. Sediment ripples and dunes. *Annu. Rev. Fluid Mechanics*, 14:13–37, 1982.

[84] F. Exner. Uber die wechselwirkung zwischen wasser und geschiebe in flüssen. *Sitzenberichte der Academie der Wissenschaf*, 134:165–180, 1925. (in German).

[85] M. Farge. Wavelet transforms and their application to turbulence. *Annu. Rev. Fluid Mech.*, 24:395–457, 1992.

[86] M. Feilner, M. Jacob, and M. Unser. Orthogonal quincunx wavelets with fractional orders. In *Proceedings of the 2001 IEEE International Conference on Image Processing*, volume I. Institute of Electrical and Electronics Engineers, IEEE, October 2001.

[87] M. Felix, S. Sturton, and J. Peakall. Combined measurements of velocity and concentration in experimental turbidity currents. *Sediment. Geol.*, 179:31–47, 2005.

[88] R. I. Ferguson. Meander irregularity and wavelength estimation. *Journal of Hydrology*, 26:315–333, 1975.

[89] Efi Foufoula-Georgiou and Praveen Kumar. *Wavelets in Geophysics*. Academic Press, Inc., USA, 1994.

[90] A. Frascati and S. Lanzoni. Morphodynamic regime and long-term evolution of meandering rivers. *Journal of Geophysical Research*, 114, 2009. doi:10.1029/2008JF001101.

[91] Roy M. Frings and Maarten G. Kleinhans. Complex variations in sediment transport at three large river bifurcations during discharge waves in the river Rhine. *Sedimentology*, 55:1145–1171, 2008.

[92] Sharon Gabel. Geometry and kinematics of dunes during steady and unsteady flows in the Calamus River, Nebraska, USA. *Sedimentology*, 40:237–269, 1993.

[93] Damien Garcia. Robust smoothing of gridded data in one and higher dimensions with missing values. *Computational Statistics and Data Analysis*, 54(4):1167–1178, 2010.

[94] Jean-Francois Ghiene, Flavia Girard, Julien Moreau, and Jean-Loup Rubino. Late Ordovician climbing-dune cross-stratification: a signature of outburst floods in proglacial outwash environments? *Sedimentology*, 57:1175–1198, 2010.

[95] A. Grinsted, J. C. Moore, and S. Jevrejeva. Application of the cross wavelet transform and wavelet coherence to geophysical time series. *Nonlinear Processes in Geophysics*, 11:561–566, 2004. SRef-ID: 1607-7946/npg/2004-11-561.

[96] Avijit Gupta. *Large rivers: geomorphology and management.* John Wiley, 2007.

[97] Ronald R. Gutierrez and Jorge D. Abad. Wavelet analysis of meandering rivers. In submission to the Geophysical Research Letters.

[98] Ronald R. Gutierrez, Jorge D. Abad, Daniel Parsons, and Jim Best. Discrimination of bedform scales using robust spline filters and wavelet transforms: methods and application to synthetic signals and the rio parana, argentina. In review, Journal of Geophysical Research.

[99] Muhammad I. Haque and Khalid Mahmood. Geometry of ripples and dunes. *Journal of Hydraulic Engineering*, 111(1):48–63, January 1985.

[100] Muhammad I. Haque and Khalid Mahmood. Analytical study on steepness of ripples and dunes. *Journal of Hydraulic Engineering*, 112(3):220–236, March 1986.

[101] Muhammad I. Haque and Khalid Mahmood. Sediment convection-diffusion and bedform length. *Journal of Hydraulic Engineering*, 113(11):1381–1401, November 1987.

[102] R. D. Hill. Analyisis of irregular of lightning channels. *Journal of Geophysical Research*, 73(6):1897–1906, 1968.

[103] Mikio Hino. Equilibrium-range spectra of sand waves formed by flowing water. *J. Fluid Mech.*, 30(3):565–573, 1968.

[104] Piet Hoekstra, Paul Bell, Pim van Santen, Niels Roode, Franck Levoy, and Richard Whitehouse. Bedform migration and bedload transport on an intertidal shoal. *Continental Shelf Research*, 24:1249–1269, 2004.

[105] Robert R. Jr. Holmes and Marcelo H. Garcia. Flow over bedforms in a large sand-bed river: a field investigation. *Journal of Hydraulic Research*, 46(3):322–333, 2008.

[106] J. M. Hooke. Changes in river meanders : a review of techniques and results of analyses. *Progress in Physical Research*, 8:473–508, 1984.

[107] Alan D. Howard. Theoretical model of optimal drainage networks. *Water Resources Research*, 26(9):2107–2117, 1990. doi:10.1029/2003WR002583.

[108] Alan D. Howard and Allen T. Hemberger. Multivariate characterization of meandering. *Geomorphology*, 4:161–186, 1991.

[109] Hsi-Ching Hsin and Ching-Chung Li. An experiment on texture segmentation using modulated wavelets. *Transactions on Systems Man, and Cibernetics*, 28(5):720–725, 1998.

[110] Hsi-Ching Hsin and Ching-Chung Li. The adaptive modulated wavelet transform image representation. *Pattern Recognition Letters*, 23:1817–1823, 2002.

[111] Andrew Hunt and Richard Favero. Using principal component analysis with wavelets in speech recognition. pages 296–301, 1994.

[112] Jasim Imran, Gary Parker, and Carlos Pirmez. A nonlinear model of flow in meandering submarine and subaerial channels. *Journal of Fluid Mechanics*, 400:295–331, 1999.

[113] Roscoe G. Jackson. Largescale ripples of the lower Wabash River. *Sedimentology*, 23:593–623, 1976.

[114] Rober B. Jacobson and David L. Galat. Flow and form in rehabilitation of large-river ecosystems: an example from the Lower Missouri River. *Geomorphology*, 77:249–269, 2006.

[115] C. S. Jain and J. F. Kennedy. The growth of sand waves. In *International Symposium on Stochastic Hydraulics*. University of Pittsburgh School of Engineering Publication Series, 1971.

[116] Subhash C. Jain and John F. Kennedy. The spectral evolution of sedimentary bed forms. *J. Fluid Mech.*, 63(2):301–314, 1974.

[117] D. J. Jerolmack, D. Mohrig, and B. McElroy. A unified description of ripples and dunes in rivers. In *River, Coastal and Estuarine Morphodynamics: RCEM 2005*, pages 843–851. Taylor and Francis Group London, 2006.

[118] Douglas Jerolmack and David Mohrig. Interactions between bed forms: Topography, turbulence, and transport. *J. Geophys. Res.*, 110, June 2005. doi: 10.1029/2004JF000126.

[119] I. T. Jollliffe. *Principal Component Analysis*. Springer, New York, USA, 2002.

[120] P. Y. Julien, G. J. Klaassen, W. B. M. Ten Brinke, and A. W. E. Wilbers. Case study: bed resistance of Rhine River during 1998 flood. *Journal of Hydraulic Engineering*, 128:1042–1050, December 2002.

[121] Perre Y. Julien and Gerit J. Klaasen. Sand-dune geometry of large rivers during floods. *Journal of Hydraulic Engineering*, 121(9):657–663, September 1995.

[122] Naoki Kabeya, Tayoko Kubota, Akira Shimizu, Tatsuhiko Nobuhiro, Yoshio Tsuboyama, Sophal Chann, and Nara Tith. Isotopic investigation of river water mixing around the confluence of the tonle sap and mekong rivers. *Hydrological Processes*, 23:1351–1358, 2008.

[123] Masoud Karbasi, Mohammad H. Omid, and Javad Farhoudi. Experimental investigation of cluster bed-form formation over uniform sediment. *Am. J. Appl. Sci.*, 7(8):1093–1099, 2010.

[124] Jeffrey S. Kargel and Randolph L. Kirk. Carbonate-Sulfate volcanism on Venus? *Icarus*, 112:219–259, 1994.

[125] L. Karimova, Y. Kuandykov, N. Makarenko, M. M. Novak, and S. Helama. Fractal and topological dynamics for the analysis of paleoclimatic records. *Physica A*, 373:737–746, 2006. doi:10.1016/j.physa.2006.04.061.

[126] Philip R. Kaufmann, Jhon M. Faustini, David P. Larsen, and Mostafa A. Shirazi. A roughness-corrected index of relative bed stability for regional stream surveys. *Journal of Geomorphology*, 99:150–170, 2008.

[127] Jason W. Kean and J. Dungan Smith. Form drag in rivers due to small-scale natural topographic features: 1. Irregular sequences. *Journal of Geophysical Research*, 111, 2006. doi: 10.1029/2006JF000490.

[128] Jason W. Kean and J. Dungan Smith. Form drag in rivers due to small-scale natural topographic features: 1. Regular sequences. *Journal of Geophysical Research*, 111, 2006. doi: 10.1029/2006JF000467.

[129] Barbara A. Kennedy. On Playfairs law of accordant juntions. *Earth Surface Processes and Landforms*, 9(2):153–173, 1984.

[130] J. F. Kennedy. The mechanics of dunes and antidunes in erodible-bed channels. *J. Fluid Mech.*, 16:521–544, 1963.

[131] C. J. Keylock, D. R. Parsons R. D. Hardy, R. I. Ferguson, S. N. Lane, and K. S. Richards. The theoretical foundations and potential for large-eddy simulation (LES) in fluvial geomorphic and sedimentological research. *Earth-Sci. Rev.*, 71:271–304, 2005.

[132] K. Kheiashy, J. McCorquodale, I. Georgiou, and E. Meselhe. Geometric and statistical characteristics of bed forms in the lower Mississippi River. In *Sixth International Symposium on Coastal Engineering and Science of Coastal Sediment Process*, New Orleans, Louisiana, USA, May 2007. American Society of Civil Engineers.

[133] M.G. Kleinhans. Sorting in grain flows at the lee side of dunes. *Earth-Sci. Rev.*, 65:75–102, 2004.

[134] M.G. Kleinhans. Grain-size sorting in grainflows at the lee side of deltas. *Sedimentology*, 52(2):291–311, 2005.

[135] Katherine Klink and Cort J. Willmott. Principal components of the surface wind field in the united states: A comparison of analyses based upon wind velocity, direction, and speed. *International Journal of Climatology*, 9(3):293–308, 1989. DOI: 10.1002/joc.3370090306.

[136] M. A. F. Knaapen. Local variation in the shape of superimposed bedforms as a function of local bathymetry. In *Proceedings of Marine Sandwave and River Dune Dynamics III*. School of Earth and Environment, University of Leeds, April 2008.

[137] Natalia Komarova and Alan Newell. Nonlinear dynamics of sand banks and sand waves. *J. Fluid Mech.*, 415:285–321, 2000.

[138] R. A. Kostaschuk and M. A. Church. Macroturbulence generated by dunes: Fraser River, Canada. *Sediment. Geol.*, 1-4:25–37, 1993.

[139] Ray Kostaschuk. Sediment transport mechanics and subaqueous dune morphology. In *River, Coastal and Estuarine Morphodynamics: RCEM 2005*, pages 795–801. Taylor and Francis Group, London, 2006.

[140] Dirk P. Kroesse, Thomas Taimre, and Zdravko I. Botev. *Handbook of Monte Carlo methods*. Wiley and Sons Inc., USA, 2011.

[141] R. A. Kuhnle, J. K. Horton, S. J. Bennett, and J. L. Best. Bedforms in bimodal sand-gravel sediments: laboratory and field analysis. *Sedimentology*, 40:631–654, 2006.

[142] Praveen Kumar and Foufoula-Georgiou. A multicomponent decomposition of spatial rainfall fields. Segregation of large and small scale features using wavelet transforms. *Water Resour. Res.*, 29:2515–2532, 1993. doi: 10.1029/93WR00549.

[143] David Labat. Recent advances in wavelet analyses: Part 1. A review of concepts. *Journal of Hydrology*, 314:275–288, 2005.

[144] Peter F. Lagasse, W. J. Spitz, L. W. Zevenbergen, and D. W. Zachman. *Handbook for Predicting Stream Meander migration*. National Cooperative Highway Research Program, National Research Council (U.S.). Transportation Research Board, Washington, D.C., USA, 2004.

[145] Luc Lambs. Interactions between groundwater and surface water at river banks and the confluence of rivers. *Journal of Hydrology*, 288:312–326, 2004.

[146] W. B. Langbein and L. B. Leopold. River meanders - theory of minimum variance. *United States Geological Survey, Professional Paper 422H*, 1966.

[147] Eddy Langendoen and Andrew Simon. Modeling the evolution of incised streams. II: Streambank erosion. *Journal of Hydraulic Engineering*, 134(7):909–915, 2008.

[148] Stefano Lanzoni and Giovanni Seminara. On the nature of meander instability. *Journal of Geophysical Research*, 111(F04006), 2006. DOI: 10.1029/2005JF000416.

[149] Alain Laraque, Jean Loup Guyot, and Naziano Filizola. Mixing processes in the amazon river at the confluences of the Negro and Solimoes Rivers, Encontro das Aguas, Manaus, Brazil. *Hydrological Processes*, 23:3131–3140, 2009.

[150] E. M. Latrubesse, J. C. Stevaux, and R. Sinha. Tropical rivers. *Geomorphology*, 70:187–206, 2005.

[151] J. Wesley Lauer, Gary Parker, and William E. Dietrich. Response of the Strickland and Fly River confluence to postglacial sea level rise. *Journal of Geophysical Research*, 113, 2006. doi: 10.1029/2006JF000626.

[152] Suzanne Leclair. Preservation of cross-strata due to the migration of subaqueous dunes: an experimental investigation. *Sedimentology*, 49:1157–1180, 2002.

[153] Suzanne F. Leclair, John S. Bridge, and F. Wang. Preservation of cross-strata due to migration of subaqueous dunes over aggrading and non-aggrading beds: Comparison of experimental data with theory. *Geoscience Canada*, 24:55–66, 1997.

[154] Carl J. Legleiter and Phaedon C. Kyriakidis. Forward and inverse transformations between cartesian and channel-fitted coordinate systems for meandering rivers. *Mathematical Geology*, 38:927–958, 2006.

[155] Luna B. Leopold, M. G. Wolman, and J. P. Miller. *Fluvial Processes in Geomorphology.* Dover, USA, 1995.

[156] Raymond A. Levey, Böjrn Kjerfve, and Rufus T. Getzen. Comparison of bed form variance spectra within a meander bed during flood and average discharge. *J. Sediment. Petrol.*, 50(1):149–155, March 1980.

[157] J. Lewin and B. J. Brindle. Confined meanders. In K. J. Gregory, editor, *River channel changes*, pages 221–233. Wiley, Chischester, UK, 1977.

[158] Sarah Little. Wavelet analysis of seafloor bathymetry: an example. *Wavelets in Geophysics*, 4:167–182, 1994.

[159] Hsin-Kuan Liu. Mechanics of sediment-ripple formation. *Journal of the Hydraulics Division*, 83(2):1–23, 1957.

[160] P. C. Liu. Wavelet spectrum analysis and ocean wind waves. In *Wavelets in Geophysics edited by E. Foufoula-Georgiou and P. Kumar.* Academic Press, San Diego, California, 1994.

[161] W. Long and R. R. Hood. A new model skill assessment metric based on discrete Fréchet distance. *Journal of Geophysical Research*, 2012. Submitted.

[162] Sergio G. Longhitano and W. Nemec. Statistical analysis of bed-thickness variation in a tortonian succession of biocalcarenitic tidal dunes, Amantea Basin, Calabria, southern Italy. *Sediment. Geol.*, 179:195–224, 2005.

[163] R. Luchi, G. Zolezzi, and M. Tubino. Bend theory of river meanders with spatial width variations. *Journal of Fluid Mechanics*, 681:311–339, 2011.

[164] J. R. E. Lutjeharms and R. C. van Ballegooyen. The retroflection of the Agulhas current. *Journal of Physical Oceanography*, 18(11):1570–1583, 1988.

[165] Jianwei Ma. Towards artifact-free characterization of surface topography using complex wavelets and total variation minimization. *Applied Mathematics and Computation*, 170(2):1014–1030, 2005. doi: 10.1016/j.amc.2004.12.053.

[166] Jianwei Ma, Xiangqian Jiang, and Paul Scott. Complex ridgelets for shift invariant characterization of surface topography with line singularities. *Physics Letters A*, 344(6):423–431, 2005. doi: 10.1016/j.physleta.2005.06.091.

[167] T. E. MacDonald, G. Parker, and D. Leuthe. Inventory and analysis of stream meander problems in Minnesota. Technical report, 1992. Department of Civil Engineering, University of Minnesota, Minneapolis, Minnesota, USA.

[168] T. B. Maddux, S. R. McLean, and J. M. Nelson. Turbulent flow over three-dimensional dunes: 2. Fluid and bed stresses. *J. Geophys. Res.*, 108:1–171, 2003.

[169] Stephane Mallat. *A wavelet tour of signal processing. The sparse way.* Elsevier, Massachusetts, USA, 2009.

[170] Marco Marani, Stefani Lanzoni, Diego Zandolin, Giovanni Seminara, and Andrea Rinaldo. Tidal meanders. *Water Resources Research*, 38(11):1–14, 2002.

[171] S. R. Massel. Wavelet analysis for processing of ocean surface wave records. *Ocean Engineering Journal*, 28:957–987, 2001.

[172] E. Mayorga, M.G. Logsdon, M.V.R. Ballester, and J.E. Richey. LBA-ECO CD-06 Amazon River Basin land and stream drainage direction maps. Available on-line [http://daac.ornl.gov] from Oak Ridge National Laboratory Distributed Active Archive Center, Oak Ridge, Tennessee, U.S.A., 2012.

[173] MDA-Federal. Landsat GeoCover 1990/TM and ETM+ 2000 edition mosaics. ETM-EarthSat-MrSID, 1.0, USGS, Sioux Falls, South Dakota, 2004.

[174] Daniel E. Mecklenburg and Anand D. Jayakaran. Dimensioning the sine-generated curve meander geometry. *Journal of the American Water Resources Association*, 48(3):635–642, 2012. DOI: 10.1111 j.1752-1688.2012.00638.x.

[175] A. J. Mercer. Analytically determined bedform shape. *Journal of the Engineering Mechanics Division*, 97:175–180, 1971.

[176] J. R. Moll, T. Schilperoort, and A. J. De Leeuw. Stochastic analysis of bedform dimensions. *Journal of Hydraulic Research*, 25(4):465–479, 1987.

[177] Kevin K. Moorhead, David W. Bell, and Rachael N. Thorn. Floodplain hydrology after restoration of a Southern Appalachian mountain stream. *Wetlands*, 28(3):632–639, 2008.

[178] Sarah. A. Morley, Jeffrey J. Duda, Holly J. Coe, Kristopher K. Kloehn, and Michael L. McHenry. Benthic invertebrates and periphyton in the Elwha River Basin: current conditions and predicted response to dam removal. *Northwest Science*, 82:179–195, 2008.

[179] M. Paul Mosley. An experimental study of channel confluences. *Journal of Geology*, 84:535–562, 1976.

[180] Elise Mostacci, Caroline Truntzer, Harvé Cardot, and Patrick Ducoroy. Multivariate denoising methods combining wavelets and principal component analysis for mass spectrometry. *Proteomics*, 10:2564–2572, 2010.

[181] D. Motta, J. D. Abad, E. J. Langendoen, and M. H. Garcia. The effects of floodplain soil heterogeneity on meander planform shape. *Water Resources Research*, 48(W09518), 2012.

[182] Davide Motta, Jorge D. Abad, Eddy J. Langendoen, and Marcelo H. Garcia. A simplified 2D model for meander migration with physically-based bank evolution. *Geomorphology*, 2011. In press.

[183] G. C. Nanson and E. J. Hickin. A statistical analysis of bank erosion and channel migration in Western Canada. *Geological Society of America Bulletin*, 97:497–504, 1986.

[184] E. J. Nason and G. C. Nanson. The character of channel migration on the Beatton River, northeast British Columbia, Canada. *Geological Society of America Bulletin*, 86:487–494, 1991.

[185] Tami J. Nicoll and Edward J. Hickin. Planform geometry and channel migration of confined meandering rivers on the Canadian prairies. *Geomorphology*, 116:37–47, 2010. doi:10.1016/j.geomorph.2009.10.005.

[186] Jeffrey D. Niemann, Nicole M. Gasparini, Gregory E. Tucker, and Rafael L. Bras. A quantitative evaluation of Playfairs law and its use in testing long-term stream erosion models. *Earth Surface Processes and Landforms*, 26:1317–1332, 2001.

[187] Vladimir I. Nikora, Alexander N. Sukhodolov, and Pawel M. Rowinski. Statistical sand wave dynamics in one-directional water flows. *J. Fluid Mech.*, 351:17–39, 1997.

[188] NIST/SEMATECH. *e-Handbook of Statistical Methods.* NIST, http://www.itl.nist.gov/div898/handbook/, 2010.

[189] C. F. Nordin and J. H. Algert. Spectral analysis of sand waves. *Proc. Am. Soc. Civil Engineers*, 92:95–114, 1966.

[190] Carl F. Jr. Nordin. A stationary Gaussian model of sand waves. In *International Symposium on Stochastic Hydraulics*. University of Pittsburgh School of Engineering Publication Series, 1971.

[191] Annie Nyander, Paul S. Addison, Ian McEwan, and Gareth Pender. Analysis of river bed surface roughnesses using 2D wavelet transform-based methods. *The Arabian Journal for Science and Engineering*, 28(1C):107–121, 2003.

[192] O. Orfeo and J. Stevaux. Hydraulic and morphological characteristics of middle and upper reaches of the Paraná River (Argentina and Brazil). *Geomorphology*, 44:309–322, 2002.

[193] Takeshi Osawa, Hiromune Mitsuhashi, Hideyuki Niwa, and Atushi Ushimaru. Enhanced diversity at network nodes: River confluences increase vegetation-patch diversity. *The Open Ecology Journal*, 3:426–437, 2010.

[194] W. R. Osterkamp and E. R. Hedman. Tperennial-streamflow characteristics related to channel geometry and sediment in missouri river basin. *USGS Professional Paper*, (1242):2107–2117, 1982.

[195] Aaron I. Packman, Mashfiqus Selehin, and Mattia Zaramella. Hyporheic exchange with gravel bed: basic hydrodynamic interactions and bedform-induced advective flows. *Journal of Hydraulic Engineering*, 130(7):647–656, 2004.

[196] Chris Paola and Leon Borgman. Reconstructing random topography from preserved stratification. *Sedimentology*, 38:553–565, 1991.

[197] Gary Parker, Panayiotis Diplas, and Juichiro Akiyama. Meanders bends of high amplitude. *Journal of Hydraulic Engineering*, 109(10), 1983.

[198] D. R. Parsons, J. L. Best, O. Orfeo, R. J. Hardy, R. Kostaschuk, and S. N. Lane. Morphology and flow fields of three-dimensional dunes, Rio Parana, Argentina: Results from simultaneous multibeam echo sounding and acoustic Doppler current profiling. *J. Geophys. Res.*, 110, 2005. doi:10.1029/2004JF000231.

[199] Daniel R. Parsons, James L. Best, Stuart N. Lane, Oscar Orfeo, Richard J. Hardy, and Ray Kostaschuck. Form roughness and the absence of secondary flow in a large confluence-diffluence, Rio Parana, Argentina. *Earth Surf. Processes Landforms*, 32:155–162, 2007.

[200] Juliana M. Aguiar Peixoto, Bruce Walker Nelson, and Florian Wittmann. Spatial and temporal dynamics of river channel migration and vegetation in central Amazonian white-water floodplains by remote-sensing techniques. *Remote Sensing of Environment*, 113:2258–2256, 2009. doi: 10.1016/j.rse.2009.06.015.

[201] J. T. Perron, J. W. Kirchner, and W. E. Dietrich. Spectral signatures of characteristic spatial scales and non-fractal structure in landscapes. *J. Geophys. Res.*, 113:61–78, 2008.

[202] E. Perucca, C. Camporeale, and L. Ridolfi. Influence of river meandering dynamics on riparian vegetation pattern formation. *Journal of Geophysical Research*, 111:1–9, 2006.

[203] James E. Pizzuto. Channel adjustments to changing discharges, Powder River, Montana. *Geological Society of America Bulletin*, 106:1494–1501, 1994.

[204] John Playfair. *Illustrations of the Huttonian theory of the earth. Edinburgh, Printed for Cadell and Davies, London, and W. Creech, Edinburgh, 1802.* University of Illinois Press, Urbana, Illinois, USA, 1956.

[205] Ari Posner. River meandering modeling and confronting uncertanty. Technical report, Sandia National Laboratories, Alburquerque, New Mexico, USA, March 2011.

[206] A. R. Prave and W. L. Duke. Small-scale hummocky cross-stratification in turbidites: a form of antidune stratification? *Sedimentology*, 37:531–539, 1990.

[207] Mariette T. H. Prent and Edward J. Hickin. Annual regime of bedforms, roughness and flow resistance, Lillooet River, British Columbia, BC. *Geomorphology*, 41:369–390, 2002.

[208] Andreas Prokoph and Jan Veizer. Trends, cycles and nonstationarities in isotope signals of phanerozoic seawater. *Chem. Geol.*, 161:225–240, 1999.

[209] Yang Qing-Yuan, Wang Xian-Ye, Lu Wei-Zhen, and Wang Xie-Kang. Experimental study on characteristics of separation zone in confluence zones in rivers. *Journal of Hydrologic Engineering*, 14(2):166–171, 2009.

[210] Jamie G. Quin. Is most hummocky cross-stratification formed by large-scale ripples? *Sedimentology*, 58:1414–1433, 2011.

[211] J. Raja, B. Muralikrishnan, and Shengyu Fu. Recent advances in separation of roughness, waviness and form. *Precision Engineering*, 26:222–235, 2002.

[212] R. E. Rathbun and C. E. Rostad. Lateral mixing in the Mississippi River below the confluence with the Ohio River. *Water Resources Research*, 40, 2004. doi: 10.1029/2003WR002381.

[213] Arved J. Raudkivi. Ripples on stream bed. *Journal of Hydraulic Research*, 123(1):58–64, 1997.

[214] Arnold J. H. Reesink and John S. Bridge. Evidence of bedform superimposition and flow unsteadiness in unit-bar deposits, South Saskatchewan River, Canada. *J. Sediment. Res.*, 81:814–840, 2011. doi: 10.2110/jsr.2011.69.

[215] Wei-Xin Ren and Zeng-Shou Sun. Structural damage identification by using wavelet entropy. *Engineering Structures*, (30):2840–2849, 2008. doi:10.1016/j.engstruct.2008.03.013.

[216] Bruce L. Rhoads, James D. Riley, and Daniel R. Mayer. Response of bed morphology and bed material texture to hydrological conditions at an asymmetrical stream confluence. *Geomorphology*, 109:161–173, 2009. doi: 10.1016/j.geomorph.2009.02.029.

[217] M. Leite Ribeiro, K. Blanckaert, A. G. Roy, and A. J. Schleiss. Flow and sediment dynamics in channel confluences. *Journal of Geophysical Research*, 117, 2012. doi: 10.1029/2011JF002171.

[218] Kelvin J. Richards. The formation of ripples and dunes on an erodible bed. *Journal of Hydraulic Research*, 99:597–618, 1980.

[219] André Robert and William Uhlman. An experimental study on the ripple-dune transition. *Earth Surf. Processes Landforms*, 26:615–629, 2001.

[220] M. Roca, J.P. Martin-Vide, and P.J.M. Moreta. Modelling a torrential event in a river confluence. *Journal of Hydrology*, 364:207–215, 2009.

[221] Philip Roni and Timothy J. Beechie. A review of stream restoration techniques and a hierarchical strategy for prioritizing restoration in Pacific Northwest watersheds. *North American Journal of Fisheries Management*, 22(1), 2002.

[222] David L. Rosgen. A classification of natural rivers. *Catena*, 22:169–199, 1994.

[223] A. Rossi, N. Massei, B. Laignel, D. Sebag, and Y. Copard. The response of the Mississippi River to climate fluctuations and reservoir construction as indicated by wavelet analysis of streamflow and suspended-sediment load, 1950-1975. *Journal of Hydrology*, 377(3-4):237–244, 2009.

[224] Peter J. Rousseeuw. Least meadian of squares regression. *Journal of the American Statistical Association*, 79(388):871–880, 1984.

[225] D. M. Rubin and C. L. Carter. Cross-bedding, bedforms, and paleocurrents. In *SEPM Concepts in Sedimentology and Paleontology*, volume 1. 2006. 2nd Editiion.

[226] B. G. Ruessink, G. Coco, R. Ranasinghe, and I. L. Turner. Coupled and noncoupled behavior of three-dimensional morphological patterns in a double sandbar system. *Journal of Geophysical Research*, 112, 2007. doi:10.1029/2006JC003799.

[227] Jori E. Ruppert-Felsot, Olivier Praud, Eran Sharon, and Harry L. Swinney. Extraction of coherent structures in a rotating turbulent flow experiment. *Physical Review E*, 72(1), 2005. DOI: 10.1103/PhysRevE.72.016311.

[228] Stanley A. Schaumm. *The fluvial system.* John Wiley and Sons, New York, USA, 1977.

[229] G. Seminara, G. Zolezzi, M. Tubino, and D. Zardi. Downstream and upstream influence of river meandering. Part 2. Planimetric development. *Journal of Fluid Mechanics*, 438:213–230, 2001.

[230] F. D. Shields, Andrew Simon, and Lyle J. Steffen. Reservoir effects on downstream river channel migration. *Environmental Conservation*, 27:54–66, 2000.

[231] Dan H. Shugar, Ray Kostaschuk, James L. Best, Daniel R. Parsons, Stuart N. Lane, Oscar Orfeo, and Richard J. Hardy. On the relationship between flow and suspended sediment transport over the crest of a sand dune, Río Paraná, Argentina. *Sedimentology*, 57:252–272, 2010.

[232] Arvind Singh, Kurt Fienberg, Douglas J. Jerolmack, Jeffrey Marr, and Efi Foufoula-Georgiou. Experimental evidence for statistical scaling and intermittent in sediment transport rates. *J. Geophys. Res.*, 114, 2009. doi:10.1029/2007JF000963.

[233] Arvind Singh, Stefano Lanzoni, Peter R. Wilcock, and Efi Foufoula-Georgiou. Multiscale statistical characterization of migrating bed forms in gravel and sand bed rivers. *Water Resour. Res.*, 47, 2011. doi: 10.1029/2010WR010122.

[234] Philip J. Soar and Colin R. Thorne. Channel restoration design for meandering rivers. Technical Report ERDC.CHL CR-01-1, Coastal and Hydraulics Laboratory, U.S. Army Engineer Research and Development Center, Vicksburg, Mississippi,, 2001.

[235] J. G. Speight. Meander spectra of the Angabunga River, Papua. *Journal of Hydrology*, 3:1–15, 1965.

[236] T. Stoesser, C. Braun, M. García-Villalba, and W. Rodi. Turbulence structures in flow over two-dimensional dunes. *Journal of Hydraulic Engineering*, 134:42–55, 2008.

[237] Hans-Henrik Stolum. River meandering as a self-organization process. *Science*, 271:1710–1713, 1996.

[238] Hans-Henrik Stolum. Planform geometry and dynamics of meandering rivers. *Bulletin of the Geological Society of America*, 110(11):1835–1491, 1998.

[239] Joep E. A. Storms, Remke L. van Dam, and Suzanne F. Leclair. Preservation of cross-sets due to migration of current ripples over aggrading and non-aggrading beds: comparison of experimental data with theory. *Sedimentology*, 46:189–200, 1999.

[240] Alice M. Takeda, Jose Stevaux, and Daniele S. Fujita. Effect of hydraulics, bedload grain size and water factors on habitat and abundance of narapa bonettoi righi and varela, 1983 of the upper parana river, brazil. *Hydrobiologia*, 463:241–248, 2001.

[241] Kunio Takezawa. *Introduction to Nonparametric Regression*. John Wiley and Sons, New Jersey, USA, 2006.

[242] Robert E. Thomas, Daniel R. Parsons, Steven D. Sandbach, Gareth M. Keevil, Wouter A. Marra, Richard J. Hardy, James L. Best, Stuart N. Lane, and Jessica A. Ross. An experimental study of discharge partitioning and flow structure at symmetrical bifurcations. *Earth Surface Processes and Landforms*, 36:2069–2082, 2011.

[243] C. Torrence and G. P. Compo. A practical guide to wavelet analysis. *Bulletin of the American Meteorological Society*, 79:61–78, 1998.

[244] George S. Triantafyllou. Vortex formation in ocean currents. *International Journal of Offshore and Polar Engineering*, 2(3):359–380, 1992.

[245] A. P. Tuijnder and J. S. Ribberink. Prediction of bedform dimensions, bed roughness and sediment transport under supply-limited conditions in rivers. Technical report, Faculty of Engineering Technology, University of Twente, The Netherlands, 2009.

[246] Maya G. Unde and Subash Dhakal. Sediment characteristics at river confluences: a case study of the Mula-Kas confluence, India. *Progress in Physical Geography*, 33:208–223, 2009. doi: 10.1177/0309133309338655.

[247] USACE. The streambank erosion control evaluation and demonstration act of 1974. Technical report, US Army Corps of Engineers, Vicksburgh, Mississipi, 1981. (Section 32, Public Law 93-. 251) amended by Public Law 94-587, Section 155 and 161.

[248] J. F. Valdes-Galicia and V. M. Velasco. Variations of mid-term periodicities in solar activity physical phenomena. *Advances in Space Research*, 5:2537–2116, 2007.

[249] C. F. van der Mark and A. Blom. A new and widely applicable bedform tracking tool. Technical report, University of Twente, Faculty of Engineering Technology, Department of Water Engineering and Management, March 2007.

[250] C. F. van der Mark, A. Blom, and J. M. H. Hulscher. Variability of bedform characteristics using flume and river data. In *River, Coastal and Estuarine Morphodynamics: RCEM 2007*, pages 923–930. Taylor and Francis Group, London, 2008.

[251] C. F. van der Mark, A. Blom, J. M. H. Hulscher, S. F. Leclair, and D. Mohrig. On the modeling the variability of bedform dimensions. In *River, Coastal and Estuarine Morphodynamics: RCEM 2005*, pages 831–841. Taylor and Francis Group, London, 2006.

[252] C. F. van der Mark, A. Blom, and J. S. M. Hulscher. Quantification of variability in bedform geometry. *J. Geophys. Res.*, 113, 2008. doi:10.1029/2007JF000940.

[253] Jeremy G. Venditti. Turbulent flow and drag over fixed two- and three-dimensional dunes. *J. Geophys. Res.*, 112:1–21, 2007. doi:10.1029/2006JF000650.

[254] Jeremy G. Venditti, Michael Church, and Sean J. Bennett. On the transition between 2D and 3D dunes. *Sedimentology*, 52:1343–1359, 2005.

[255] F. Visconti, C. Camporeale, and L. Ridolfi. Role of discharge variability on pseudomeandering channel morphodynamics: Results from laboratory experiments. *Journal of Geophysical Research*, 115, 2010. doi: 10.1029/2010JF001742.

[256] J. J. Walton and D. M. Hardy. Principal components analysis and its application to wind field pattern recognition. Technical Report UCRL-52488, Lawrence Rivermore Laboratory, 1978.

[257] Zhi-Qian Wang and Nian-Sheng Cheng. Time-mean structure of secondary flows in open channel with longitudinal bedforms. *Adv. Water Resour.*, 29:1634–1649, 2006.

[258] J. J. Warmink, M. J. Booij, S. J. M. H. Hulscher, and H. Van der Klis. Uncertainty in design water levels due to uncertain bed form roughness in the River Rhine. In *International Conference on Fluvial Hydraulics (River Flow 2010)*, pages 359–366, Braunschweig, Germany, September 2010. IAHR - Fluvial Hydraulics Committee, Technische Universität Braunschweig, EWE Aktiengesellschaft.

[259] A. W. E. Wilbers and W. B. M. Ten Brinke. The response of subaqueous dunes to floods in sand and gravel bed reaches of the Dune Rhine. *Sedimentology*, 50:1013–1034, 2003.

[260] Mark L. Wildhaber, Peter J. Lamberson, and David L. Galat. A comparison of measures of riverbed form for evaluating distributions of benthic fishes. *North American Journal of Fisheries Management*, 23:543–557, 2003.

[261] Yong Wu, Yuanjun He, and Hongming Cai. Optimal threshold selection algorithm in edge detection based on wavelet transform. *Image and Vision Computing*, 23:1159–1169, 2005.

[262] Wang Xuan, Lei Li, and Wang Mingzhe. Palmprint verification based on 2D-Gabor wavelet and pulse coupled neural network. *Knowledge-Based Systems*, 27:451–455, 2012.

[263] M. S. Yalin. Geometrical properties of sand waves. *Journal of the Hydraulic Division*, 90:105–119, 1964.

[264] M. S. Yalin. *River Mechanics.* Pergamon Press, USA, 1992.

[265] Salim Yalin and Grace Lai. On the form drag caused by sand waves. Technical Report 363/II-4, Japan Society of Civil Engineers, November 1985.

[266] Bofu Yu and M. Gordon Wolman. Some dynamic aspects of river geometry. *Water Resources Research*, 23(3):501–509, 1987.